価数揺動状態がある希土類の硫化物合成とその応用

メタデータ	言語: eng 出版者: 公開日: 2016-11-18 キーワード (Ja): キーワード (En): 作成者: 李, 良 メールアドレス: 所属:
URL	https://doi.org/10.15118/00009029

Synthesis of Rare-Earth Sulfides (RE=Yb, Eu, and Sm) with Valence-Fluctuated Characters and Their Applications

（価数揺動状態がある希土類の硫化物合成とその応用）

A Dissertation

Submitted to Muroran Institute of Technology

Division of Science for Composite Functions

In Partial Fulfillment of the Requirements

For the Degree of Doctor of Engineering

By

Liang Li

Muroran Institute of Technology

Muroran, Hokkaido, Japan

September 2016

Certificate of Approval

This dissertation entitled:

Synthesis of Rare-Earth Sulfides (RE=Yb, Eu, and Sm) with

Valence-Fluctuated Characters and Their Applications

（価数揺動状態がある希土類の硫化物合成とその応用）

Written by Liang Li
has been approved for the Division of Science for Composite Functions
Muroran Institute of Technology Hokkaido, Japan

Date: ____________________

____

Professor Dr. Shinji Hirai

Singed by the final examining committee:

____

_

Professor Dr. Akira Sakai

____

_

Professor Dr. Chihiro Sekine

The Final copy of this dissertation has been examined by the signatories, and we find that both the content and form meet acceptable presentation standers of scholarly work in the above mentioned discipline.

Acknowledgments

First and foremost I have to thank **God** for being my strength and guide in the writing of this thesis. Without Him, I would not have had the wisdom or the physical ability to do so.

I would like to express my deepest thanks and humble supplication to my supervisor Prof. Dr. Hirai Shinji for his untiring guidance and efforts during the entire course of the research and preparation of this dissertation. I would also like to thank Prof. Dr. Sakai, Prof. Dr. Sekine and Prof. Dr. Nakamura for their instructions and valuable comments.

I would like to express my sincere gratitude to Dr. Toshihiro Kuzuya and Dr. Kawamura for enormous help and guidance throughout. I would also like to thanks all my friends and my laboratory staffs for all kinds of helps during my study in Muroran institute of technology.

I also need to thank the Japanese Government (MONBUKAGAKUSHO: MEXT) Scholarship for financial support during these three years.

Last, I would like to thank my wife and my parents for their spiritual support during my study in Japan.

Abstract

In some rare earth compounds, valences of rare earth elements take non-integer values, because valence values of rare earth elements fluctuate spatially and temporally. The fluctuated valences depend strongly on the synthesis temperature. In this study, Yb, Eu, Sm based sulfides with valence-fluctuation characters were to study the synthesis and stability and expected to discover new applications.

Ytterbium sulfides were prepared from CS_2 sulfurization of Yb_2O_3 and then heat treatments. Ytterbium sulfides (Yb_3S_4 and YbS) are expected to be employed as high temperature n-type thermoelectric materials due to their large Seebeck coefficient.

The influences of particle size and specific surface area of Yb_2O_3 powders, sulfurization temperature and time and CS_2 gas flow rate on preparation of ytterbium sesquisulfide (Yb_2S_3) were researched. Small particle size (< 1 μm) and large specific surface area (> 2 m^2/g) of Yb_2O_3 are necessary for fabrication of pure Yb_2S_3. Single orthorhombic η-Yb_2S_3 and hexagonal ε-Yb_2S_3 were synthesized by the sulfurization of fine Yb_2O_3 powders at 700 ~ 800 °C and 1000~1050°C with CS_2 gas flow rate of 1.67 mL/s, respectively. Orthorhombic η-Yb_2S_3 transformed to hexagonal ε-Yb_2S_3 with increase of temperature. The heat treatments of Yb_2S_3 were investigated. Upon heat treatment at 1000 °C for 3 hr in Ar/CS_2 atmosphere, orthorhombic Yb_2S_3 phase underwent phase transition to hexagonal Yb_2S_3 phase. Moreover, orthorhombic Yb_3S_4 was main phase after heat treatment at 1050°C for 8 hr under Ar atmosphere and Yb_2S_3 disappeared upon prolonged (12 hr) heat treatment. Single Yb_3S_4 phase could be obtained after treatment at 1000 °C for 3 hr, or at 1200 °C for 1 hr, under vacuum ($\sim 1.2\times10^{-3}$ Pa). Single-phase YbS with a homogeneity range of $YbS_{1.11-1.15}$ could be synthesized by treatment at 1500 °C for 3 hr.

Secondly, europium sulfides were synthesized by CS_2 sulfurization of Eu_2O_3. EuS is a ferromagnetic semiconductor with NaCl type crystal structure. As this temperature is in the proximity of the boiling point of hydrogen, EuS is a potential magnetic refrigeration material.

The effects of Eu_2O_3 character and sulfurization conditions on the preparation of europium sulfides were researched. Single-phase Eu_3S_4 and EuS can be obtained by CS_2 gas sulfurization of spherical Eu_2O_3 with larger specific surface area and small grain size at 500 °C for longer than 0.5 hr and 800 °C for 8 hr, respectively. Moreover,

EuS can be fabricated from self-prepared needle Eu_2O_3 at 750 °C for 8 hr. The higher sulfurization temperature and shorter sulfurization time accelerated the formation of high purity EuS. Specific surface area of synthetics lessened with the rising of sulfurization temperature and time. Synthetic pure Eu_3S_4 were treated under rich-sulfur atmosphere, inert atmosphere and vacuum, respectively. Single EuS phase was obtained at 973 K under rich-sulfur atmosphere or at 1073 K under inert atmosphere. The stability of Eu_3S_4 during annealing is weaker than all above mentioned conditions and the transformation finished at 873 K under vacuum of 1.2 $*10^{-5}$ Pa. The transformation of Eu_3S_4 to EuS was attributed to stability of Eu^{2+} at high temperature. The synthetic EuS powders were sintered under a uniaxial pressure of 50 MPa in vacuum. The large reversible magnetocaloric effect of polycrystalline EuS was observed, which underwent second-order ferromagnetic to paramagnetic transition at 16.8 K. The maximum of magnetic entropy change is as large as 6.32 J/mol/K and the adiabatic temperature change is 9.1 K under a vary magnetic field change of 5 T. The entropy value for polycrystalline EuS was revised by the combination of the magnetization and heat capacity data. The relative cooling power for polycrystalline EuS reached 69.26 and 125.39 J/mol for ΔH = 3 T and 5 T, respectively.

Finally, non-stoichiometric samarium monosulfide (SmS_x, $0.55<x<1.2$) was synthesized from Sm_2S_3 and SmH_3 at 1273 K for 3 hr under vacuum. Until now, polycrystalline SmS prepared from the direct reaction between samarium and sulfur, has a thermoelectric figure of merit ZT ~0.9 with the optimal composition $SmS_{0.96}$. The influence of reaction ratio of Sm_2S_3 to SmH_3 on the fabrication of SmS was investigated.

The fabrication of SmS required the mole ratio of Sm_2S_3 to SmH_3 above 1. Lattice parameter of synthetic SmS increases firstly and then decreases to saturate following with the addition of SmH_3 content. SmS compact was sintered at 1373 K by spark plasma sintering. Density of synthetic SmS is about 99% of theory density. Seebeck coefficient of n-type semiconductor SmS_x decreases as temperature rises. The absolute value is distributed between 170-280 $\mu V\cdot K^{-1}$. The electrical conductivity of SmS_x ($0.86<x<1.07$) decreases with temperature increasing and shows similar temperature dependence. The surplus Sm which randomly distributed in the SmS_x ($0.55<x<0.75$) matrix, leads to a remarked reduces of electrical resistivity. The optimized power factor for $SmS_{0.6}$ and $SmS_{0.75}$ can reach 1500 μW·K^{-2}·m^{-1} at 600 K.

概要

価数揺動状態とは、価数が時間的に揺らぐことによって整数値から離れた中途半端な値をとる場合のことである。価数揺動の特徴の一つに、価数が強く温度依存することがある。本研究では、価数揺動状態がある Sm, Eu, Yb について、その用途に見合う単相の硫化物を合成することを目的とする。

最初に、Yb_2O_3 の CS_2 ガス硫化と熱処理によるイッテルビウム硫化物を合成した。斜方晶 Yb_3S_4 は p 型熱電材料、立方晶 YbS も 773 K 付近においてゼーベック係数が 1000μV/K に達した後、1023～1173 K 付近から高温では n 型になる熱電材料として期待されている。

硫化実験の結果、粒径が細かく、比表面積が大きな Yb_2O_3 の場合、973～1073 K の低温の硫化では η-Yb_2S_3、1273～1373 K の高温の硫化では ε-Yb_2S_3 単相が生成した。これに対してさらに大きな比表面積の Yb_2O_3 の場合、873K の硫化でも η-Yb_2S_3 単相の生成が確認された。また、η-Yb_2S_3 を真空中で熱処理すると Yb_3S_4 が生成し、とくに長時間または高温で熱処理すると YbS を得ることができた。

次に、Eu_2O_3 の CS_2 ガス硫化によりユーロピウム硫化物を合成した。EuS は NaCl 型結晶構造を有する強磁性半導体であり、磁気相転移温度が水素液化温度（20 K）の近くにあるため、水素液化磁気冷凍の液化段に利用できる磁気冷凍材料の候補材料である。

Eu_2O_3 には細粒と粗粒を用意し、細粒の場合、硫化時間にかかわらず 773 K の硫化では Eu_3S_4 単相、1073K の硫化では EuS 単相が生成した。EuS の生成は、Eu_2O_3 から EuS_2 を経て Eu_3S_4 を生成し、次いで一部 Eu_2O_2S を生成しながら EuS を生成するものと推定した。一方、細粒の場合、硫化条件にかかわらず Eu_3S_4 は生成せず、硫化時間が 1.8 ks と 28.8 ks の場合、低温で生成した Eu_2O_2S はそれぞれ 1273 K と 1073 K より高温で消滅し、EuS 単相となった。すなわち、Eu_2O_3 から Eu_2O_2S を経て EuS を生成することが確認された。

また、EuS 焼結体の磁気ゼロ及び磁場中（5T）の比熱を測定したところ、磁気ゼロの場合は 16.5 K に磁気転移に伴う大きなピーク、一方、磁場中は、ピークが磁場により広がりながら高温にシフトするという強磁性－常磁性状態を二次相転移する常磁性体の典型的な変化を示した。また、MPMS を用いた磁化測定から求めた単位体積当たりの磁気エントロピー変化の温度依存性から、16.8 K 付近に山型のピークが確認され、単結晶で見られた磁気エントロピー変化の値と一致した。すなわち、EuS 焼結体が単結晶と同等の磁気熱量効果を有することが明らかになった。

最後に、Sm_2S_3 粉末と SmH_3 粉末の反応焼結法により非化学量論組成の SmS_x,（$0.55<x<1.2$）焼結体を作製した。これまで、Sm 金属と硫黄の直接反応により $SmS_{0.96}$ が合成され、1000 K において性能指数（Z）が 0.9×10^{-3} K^{-1} に達することが報告されている。最初に、BN 坩堝中で所定の配合比の Sm_2S_3 と SmH_3 の混合粉末を焼成後、パルス通電焼結法により焼結体を作製した。

焼結体の電気抵抗（ρ）と S ゼーベック係数を測定したところ、ρ は、仕込み組成が化学量論組成付近の焼結体では高温ほど減少する半導体的挙動を示した。一方、仕込み組成（SmH_3 / Sm_2S_3）が 2 ~ 2.5 以上となり SmH_3 が過剰に

仕込まれると電気抵抗率は金属的な挙動を示した。また、仕込み組成が化学量論組成付近では温度と共にゼーベック係数が増加する傾向が見られたが、それよりも SmH_3 を過剰に加えた場合の焼結体ではゼーベック係数の明確な温度依存性が見られなくなった。出力因子は、Sm 過剰の焼結体で 1000～1500$\mu WK^{-2}m^{-1}$ と化学量論比付近のものに比べると大きくなった。

Contents

Dedication **I**
Acknowledgments **III**
Abstract **IV**
Chapter 1 Introduction **1**
1. 1 Background rare-earth sulfide **1**
1.1.1 Structure and characters of rare earth sulfide 1
1.1.2 Synthesis of Rare-earth sulfides 2
1.1.3 Application， 5
1.2 Valence-Fluctuation rare-earth sulfides **8**
1.3 Research purpose and motivation **12**
Chapter 2 Synthesis, sintering and heat capacity of ytterbium sulfides **15**
2.1 Introduction **15**
2.2 Experimental details **16**
2.2.1 Characters of Yb_2O_3 powders 16
2.2.2 Sulfurization, heat treatment and sintering of ytterbium sulfides 18
2.2.3. Analysis and characterization of as-synthesized materials 19
2.3 Sulfurization of ytterbium sesquisulfides **20**
2.3.1 XRD results of Yb_2S_3 20
2.3.2 Dependence of temperature, time and GFR on the formation of Yb_2S_3 24
2.3.3 Morphology, particle size distribution and specific surface area of Yb_2S_3 28
2.3.4 Kinetic analysis of reaction rate 33
2.3.5 Comparison of synthesis process of rare-earth sesquisulfides 34
2.4 Heat treatment and sintering of ytterbium sulfides **35**
2.4.1 Heat treatment of Yb_2S_3 under Ar or Ar/CS_2 gas 35
2.4.2 Heat treatment of Yb_2S_3 under vacuum 37
2.5 Sintering and Heat capacity of Yb_3S_4 and YbS **39**
2.6 Conclusions **41**
Chapter 3 Preparation, sintering and large magnetocaloric effect of europium sulfides **43**
3.1 Introduction **43**
3.2 Experimental procedure **45**
3.3 Influence of Eu_2O_3 character and sulfurization conditions on the preparation of EuS **47**
3.3.1 Preparation of Eu_3S_4 and EuS by CS_2-gas sulfurization of Eu_2O_3 47
3.3.2 Influence of sulfurization conditions on the formation of EuS 53
3.3.3 Morphology and specific surface area of EuS particles 55
3.3.4 Thermodynamic analysis of sulfurization process 62
3.4 Heat treatment of synthesized Eu_3S_4 **65**
3.5 Sintering and large magnetocaloric effect of synthesized EuS **71**
3.5.1 Sintering of synthetic EuS powder 71
3.5.2 Magnetization of polycrystalline EuS compacts 73
3.5.3 Specific heat of polycrystalline EuS compacts 77

3.5.4 Comparison specific heat of polycrystalline and singe crystal EuS 81
3.6 Conclusions 81
Chapter 4 Synthesis and sintering of samarium rich SmS_x and its electrical property 83
4.1 Introduction 83
4.2 Experimental procedure 84
4.2.1 Synthesis of SmS_x powders 84
4.2.2 Sintering of SmS_x compacts 84
4.2.3 Electrical properties of SmS_x compacts 85
4.3 Experimental results 85
4.3.1 Synthesis of SmS_x powders 85
4.3.2 Sintering of SmS_x compacts 90
4.3.3 Electrical transport properties of SmS_x compacts 92
4.4 Conclusions 95
Chapter 5 Conclusions 96
References 98

Chapter 1 Introduction

1. 1 Background rare-earth sulfides

Sulfides are promising candidates for environment-friendly and cost-effective materials. The rare-earth elements, Ln, are the elements which atomic numbers are 21, 39 and 57 through 71 in the periodic table. The characteristics of rare-earth elements are unfilled and filled 4f shell and lanthanide contraction.

Rare-earth, Ln, can combine with sulfur to procedure rare-earth sulfides with different formulas, such as rare-earth sesquisulfide (Ln_2S_3), monosulfide (LnS), Ln_3S_4, and LnS_2.

1.1.1 Structure and characters of rare earth sulfide

Lanthanide monosulfides, LnS, adopt the cubic NaCl-type structure. Magnetic measurements show that most rare-earth monosulfides contain trivalent metals implying an unbonded electron, $Ln^{3+}(e^-)S^{2-}$. The extra electron is delocalized in the 5d conduction band giving rise to metallic type conduction. However, the monosulfide of ytterbium, europium and samarium contain divalent metals, $Ln^{2+}S^{2-}$, and behave as semiconductors [1]. The variation of the lanthanide oxidation state is a result of the change of lanthanide electronic configuration. Although the valence configuration of most gas phase Ln^{2+} ions is $4f^{n+1}$, it appears that in some divalent lanthanide compounds, the $4f^n5d^1$ configuration is more stable resulting in an electron occupying the broad 5d band [2, 3]. This is also reflected in their cell parameters, with the genuine $Ln^{2+}S^{2-}$ compounds having larger cell dimensions than $Ln^{3+}(e^-)S^{2-}$[4]. The lanthanides that usually remain divalent in their compounds are those that have relatively accessible divalent state (i.e. Eu, Yb, and Sm). Generally, the stability of their divalent state increases with decreasing anion electronegativity. These divalent lanthanide compounds varied the lanthanide oxidation state leading to the change in the lanthanide electronic configuration.

Lanthanide sesquisulfides, Ln_2S_3, exist in a variety of polymorphic forms and larger lanthanides favoring higher coordination[5]. For a limited range of lanthanide elements, Light Ln_2S_3 (light Ln: La, Pr, and Nd) exhibit three polymorphic forms (α, β and γ) structure types where the lanthanides are 7- to 8-coordinate [6]. The orthorhombic α-Ln_2S_3 is stable at low temperature with exactly stoichiometric and irreversibly transformed to β phase. The tetragonal β-Ln_2S_3 is an oxysulfide with a limiting composition of $Ln_{10}S_{14}O$. Moreover, the β phase is transformed to γ phase with Th_3P_4 structure at higher temperature. This cubic γ phase has a wide composition range varying from Re_2S_3 to Re_3S_4. In addition, the γ phase exists in all sesquisulfides from La to Lu [7-9]. The composition of γ phase is expressed by $R_{2.67}V_{0.33}S_4$ (V: vacancy, where $V_{0.33}$ represents the maximum number of metal vacancies); the vacancy can be occupied by an R composition up to R_3S_4 ($R_{2.25}S_3$)[6]. The sesquisulfides of Dy to Tm (Lu) exist in the monoclinic δ-phase with 6- and 7-coordinate lanthanide ions [10, 11]. The heavier lanthanides (Tm to Lu) typically give sesquisulfides of the ε-form, having the rhombohedral corundum-type structure, with the lanthanides being 6-coordinate[12]. Low temperature varieties of these sesquisulfides exist in the cubic Tl_2O_3-type τ-phase[13].

1.1.2 Synthesis of Rare-earth sulfides

Both the monosulfide and sesquisulfides can be obtained from direct combination of elements in stoichiometric properties held at temperature range from 600 to 1050 °C for 2 to 3 days [14]. The monosulfides can be synthesized from their corresponding sesquisulfides through a variety of ways: (1) reduction in the pressure of aluminum (~1500 °C)[15], (2) reaction with lanthanide metal (1350 °C) [16], and (3) thermal dissociation under vacuum (1650 °C)[17].

Cerium, the most fascinating member of the periodic and abundant resources among rare earth elements, is an antiferromagnetic or a superconductor under various conditions of temperature and pressure[18]. My supervisor Professor Hirai had synthesized cerium monosulfide (CeS) powders by the reduction of Ce_2S_3 powder with an excess amount of metallic Ce at 1273 K for 10.8 ks[15]. Ce_2S_3 was obtained from with CS_2-gas sulfurization of ceria (CeO_2) powder[19]. The synthetic CeS powders contained a small amount of Ce, Ce_2O_2S, and β-Ce_2S_3 as impurities[15]. The oxygen content of CeS compact gradually decreases as the sintering temperature increases due to the evaporation of the volatile CeO[15].

Single-phase CeS compact was formed by sintering at 2173 K[15]. To evaluate the activation energy for densification of CeS, a CeS powder was prepared by milling an initial sintered compact and was used as an ingredient for hot-press experiments[15]. Densification data during hot-press sintering were analyzed using a kinetic equation, showing that boundary diffusion is a rate-limiting process[15]. The results suggest that this boundary diffusion model can explain well the densification data, with apparent activation energy of 479 kJ·mol^{-1}[15].

Rare-earth sesquisulfides can be synthesized by the direct reaction of rare-earth and sulfur in a sealed tube [20] or reductive gas sulfurization of rare-earth oxide[6] or slat (carbonate, sulfate, nitrate and oxalate)[21]. However, there are some problems for the direct reaction method. It is difficult to control the partial pressure of rare earths and sulfur to obtain rare earth sulfides with desired compositions. And then the residual oxysulfide leaves in the products from the oxidation of the rare earth surfaces.

The frequently-used reducing agent is H_2S gas or CS_2 gas[19, 22]. Figure 1.1 shows temperature dependences of ΔG° values for the sulfurization reactions of La_2O_3 powders using CS_2 and H_2S gases. The temperature dependences of the ΔG° values for the sulfurization reaction of several rare earth oxide powders using CS_2 and H_2S gases were calculated from the thermodynamic data. The ΔG° values of almost all the sulfurization reactions with CS_2 progress at a lower temperature because the ΔG° values are negative and significantly lower than those of the reactions using H_2S.

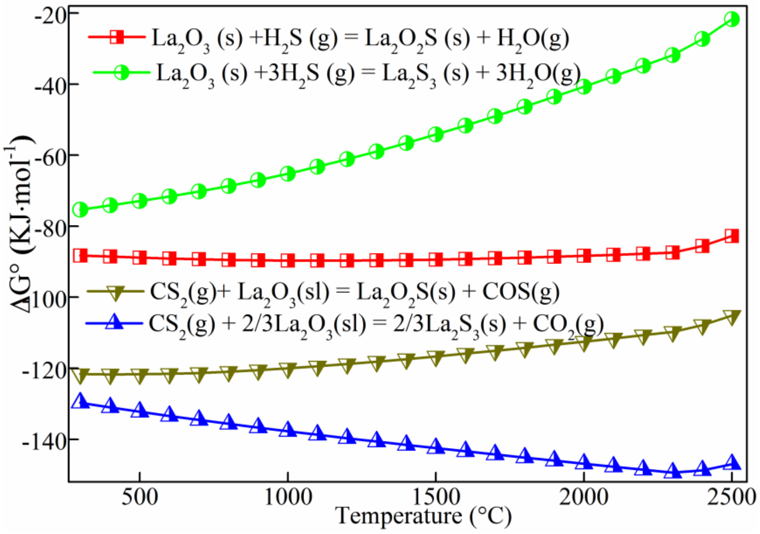

Fig. 1.1 temperature dependences of ΔG° values for sulfurization reactions of La_2O_3

To improve this method, our lab has synthesized some lanthanide sesquisulfides with CS_2-gas sulfurization of their oxides [6, 19, 23]. In the synthesis of light Ln_2S_3 via the CS_2-gas sulfurization of Ln_2O_3 powder, single-phase β-La_2S_3 were finally synthesized at above 1023 K for 8 h [6]. The α-Pr_2S_3 having a trace of β-Pr_2S_3 was formed for a shorter period of time at above 1123 K[6]. And α-Nd_2S_3 having a trace of β-Nd_2S_3 and single phase α-Sm_2S_3 were formed for a shorter period of time at above

1073 and 1123 K, respectively[6]. Ln_2O_2S were also formed in the initial stage of reaction [6]. In all cases, the impurity oxygen content in synthetic powders decreased gradually with an increase in sulfurization temperature. Moreover, the carbon content in these powders increased gradually with an increase in the sulfurization temperature[6].

Single-phase orthorhombic α-Ln_2S_3 (Ln= Gd, Tb, and Dy) is prepared at 1023K, 1323 K, 1203 K for 8 h, respectively. Single-phase monoclinic δ-Ho_2S_3 is formed at 1323 K for 8 h [23]. Gadolinium and holmium sesquisulfides were also synthesized via the CS_2-gas sulfurization of their oxalate, acetate, carbonate, and nitrate[21]. Single phase cubic γ-Gd_2S_3 was formed by the sulfurization of octanoate at 1073 K and oxalate at 873 K[21]. It has also found that gadolinium salts are thermally decomposed at temperatures high than 500 K[21]. The thermal decomposition leads to the formation of gadolinium oxide via an oxycarbonate. In the case of holmium sesquisulfides, the sulfurization of holmium oxide and nitride provide the mixture of δ-Ho_2S_3 and Ho_2O_2S impurity, while pure γ-Ho_2S_3 is exclusively formed from oxalate, acetates, or carbonates[21]. These results reveal that the formation of oxycarbonate such as $Gd_2O_2CO_3$ and $Ho_2O_2CO_3$ play an important role in the formation of γ-Gd_2S_3 and γ-Ho_2S_3[21]. Moreover, γ-Ho_2S_3 phase transformed to δ-Ho_2S_3 phase at above 1073 K and δ-Ho_2S_3 phase was stable at 1773 K[21].

To reduce the residual carbon content in the synthetic rare earth sulfides prepared by CS_2-gas sulfurization, especially at higher temperatures, the thermal decomposition of NH_4SCN was employed as the sulfur source. According to the thermogravimetry-differential thermal analysis (TG-DTA) and mass spectrometry analysis, NH_4SCN decomposed to NH_3, CS_2, H_2S, and HNCS at 400-550 K with a large mass reduction and endothermic peak [24].

Figure 1.2 shows schematics of the sulfurization apparatus. Different CS_2-gas sulfurization, the mixture gases from the thermal decomposition of NH_4SCN were introduced with Ar gas into a silica-glass reaction tube. Single phase of β-La_2S_3 and β-Gd_2S_3 were synthesized using these mixture gases from La_2O_3 and Gd_2O_3 at 1173 -1373 K. the residual carbon content of the obtained sesquisulfides from NH_4SCN sulfurization was significantly lower than that of CS_2-gas sulfurization. So the advantage of NH_4SCN sulfurization is the decrease of residual carbon content. But the generated H_2S gas is too dangerous and the temperature of mantle heater is unstable during the sulfurization process. Therefore, the NH_4SCN sulfurization is not fit for the industrial production.

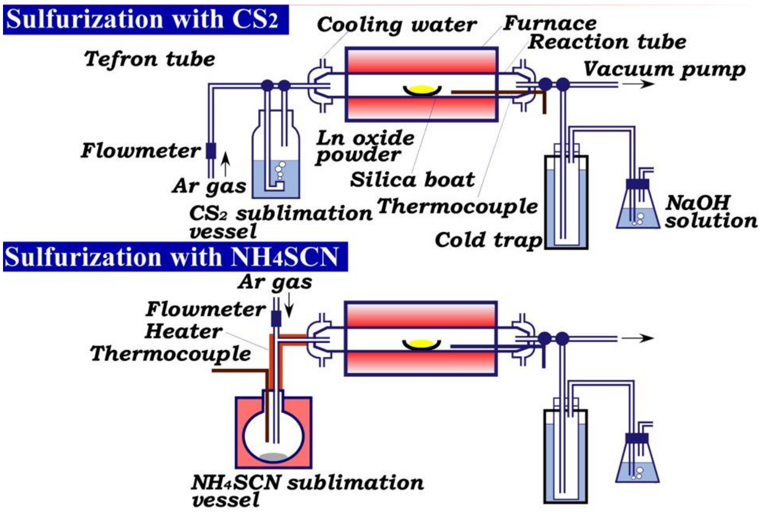

Fig. 1.2 Schematics of the sulfurization apparatus

1.1.3 Application，

Rare earth sulfides have been widely used for luminescent[25], magnetic and electronic materials[26]. In the last decade, these materials are essential in the energy storage, energy saving and renewable energy technology, which enable us to realize the sustainable society. Effective application of rare earth sulfides contains three aspects: pigment; crucible; thermoelectric materials.

1.1.3.1 Application of pigment

Rare earth sesquisulfides doping with at least one alkali/alkaline earth metal are well suited for the coloration of cosmetic, plastics, paints and rubbers[27]. Novel environmental friendly colorant/pigment can be prepared via precipitation technology and consisted of a core/shell structure [28]. The core is rare earth sesquisulfides doped with alkali/alkaline earth metal and the shell contains a coating layer of at least one transparent oxide deposited onto the external surface of the doped core particles[28]. The fluorination treatment of the core of doped rare earth sesquisulfide can improve the chromatic (both thermal and chemical stability) properties [29]. Moreover, the mean particle size of colorant products can be controlled with the value of 1.5 μm by the variation and optimization of the starting materials and sulfurization agent and condition[30, 31].

New ecological pigment Mg-Yb-S system [32] and Ca-Yb-S system [33]have been synthesized and characterized. MgS-Yb_2S_3 system[32] gives yellow color while CaS-Yb_2S_3 system [33] has variable color (blue-green) and controllable crystal structure (NaCl-type and Yb_3S_4-type) with different Yb concentration.

Recently, unfilled and sodium doped Ce_2S_3 with Th_3P_4 structure, as the most common red paint, has been widely investigated. SiO_2 coated Ce_2S_3 was prepared as red pigment to improve the thermal stability[34]. Compared with the heavy rare earth ion (Dy^{3+}, Ho^{3+}, Er^{3+}) doping of Ce_2S_3, the adjacent light rare earth element La was doped to Ce_2S_3 to improve the stability and check the possibility as red pigment[35]. Moreover, to quest the nontoxic alternatives based on rare-earth elements, the color of cerium fluorosulfide (CeSF, a typical example of the new class of rare-earth pigments) and mercury sulfide α-HgS (also known as cinnabar red or vermilion) were computed from first principles and the power of modern computational methods implicated the theoretical design of materials with specific optical properties[36].

1.1.3.2 Application of crucible

Another possible application for rare earth sulfide is crucible. Cerium monosulfide with high melting point is possible to consider as a refractory material[15]. Cerium sulfides, CeS, Ce_3S_4 and Ce_2S_3, have been considered as refractory sulfide crucibles[37, 38]. These refractory sulfide crucibles have prepared from the cold-press of the grinded sulfide powders and then sintered with different procedures and technologies[37]. Sulfides powders was prepared by H_2S gas sulfurization of CeO_2 for Ce_2S_3, vacuum heating Ce_2S_3 near its melting point for Ce_3S_4 and direct reaction of Ce_2S_3 and slight excess of Ce for CeS[38].

Test and evaluation of individual sulfide refractory as containers for various metals have been summarized[37]. The operating temperature of CeS crucible is less than 1800 °C and it cannot be used for platinum[37]. The Ce_3S_4 crucible is more susceptible to reduction of reactive metal for the formation of CeS protective layer and easily attacked by the alkaline earth-metal at its volatile temperature[37]. The properties of Ce_2S_3 crucible are intermediate between CeS and Ce_3S_4 so it cannot be used at temperature above 1500 °C[37]. Moreover, the properties of crucible are dependent on the consideration of optimal melting techniques, purification of gas atmospheres and porosity. For a certain metal and sulfide crucible, sometime different results are obtained. Here, we take titanium and CeS crucible as an example to discuss. When titanium was melted in CeS crucible at 1500 °C for 10 min, sound ingot coated with CeS can be obtained but stuck to crucible. However, Ti melted in CeS crucible with a heavy precipitate. This situation can be explained by three possible elements (porosity, gas atmospheres or melting condition).

1.1.3.3 Application of thermoelectric materials

Excellent thermoelectric materials have a large ZT, which means that the thermopower (S) is large, the electrical resistivity (ρ) and the thermal conductivity (κ) are small. The rough standard for practical use is ZT= 0.8-1. The cubic rare earth sesquisulfides with Th_3P_4 structure is an important high-temperature thermoelectric material [39].

The solid solution Ln_2S_3-Ln_3S_4 (Ln = La, Ce, Pr, Gd, Dy) with cubic structure have been extensively investigated for high temperature thermoelectric conversion materials. All γ-Ln_2S_3 compounds are insulator without any vacancy while Ln_3S_4 has one ninth conduction electron in per formula unit. The content of rare-earth vacancy is dependent on the ration of Ln/S from 1.33 to 1.5. As the quantity of vacancy increases, the n-type carrier concentration increases. Namely, the electron concentration and power factor can be increased by self-doping. Further, the lattice thermal conductivity can be kept low because of the complex crystal structure. Additionally, most rare earth sesquisulfides have melting points of greater than 2000 K. Theoretically speaking; it is possible to optimize the electrical conductivities, carrier concentrations and charge-carrier mobilities by adjusting the vacancy contents.

Actually, we need to consider which specific rare-earth element is the best choice for the highest potential thermoelectric performance before we optimize the vacancy concentrations. However, it is a very difficult problem to answer. Because rare earth elements are similar in properties and the differences of electrons numbers of 4f layer have no direct influence on thermoelectric properties, which is different with magnetic materials. Secondly, the most suitable sulfide is difference from the published data, e.g., Takeshita et al. [40] reported a ZT value of 0.75 for $LaS_{1.42}$ at 1273 K, while Gadzhiev et al. [41] reported $GdS_{1.48}$ has a ZT value of 0.74 at 1200 K. Furthermore, Taher and Gruber [42] estimated a ZT value of 0.41 for $NdS_{1.49}$ at 770 K and determined the highest ZT value of 1.5 for $DyS_{1.496}$ at 1000 K.

The reasons caused the difference included the following aspects: (1) the influence of impurity content on the thermoelectric property, e.g., if the measured sample contained oxygen contamination or the formed β-phase on the grain boundary of γ-phase, which may cause a concomitant deterioration of the electrical conductivity. (2) The effects of preparation methods. Preparation methods employed by different authors may also cause differences between different stoichiometry. (3) In the calculation process of the above mentioned ZT values, the thermal conductivity is not experimentally determined, but analogy. Because there is the assumption, these ZT values may include some errors. (4) Not only the preparation process may affect the thermoelectric properties, different testing gas atmospheres may also cause slightly changes in the chemical composition, because different gas atmosphere will affect the stability of sample dissociation energy. These variations are so small and little that there is little literature made a detailed characterization of microstructure structure or the composition for the tested sample. According to another expression of ZT, effective mass and mobility are proportional to ZT value. Gadzhiev et al. have compared effective masses and mobilities of La_3S_4, Dy_3S_4, Pr_3S_4, and Gd_3S_4 and found that La_3S_4 had large effective mass and mobility. However, Vickery R.C. et al. concluded that the shift point occurred at the Gd in the research of the influence of different chalcogenides and rare earth elements on the thermoelectric properties. So, Gd-based sulfides are also possible for the high performance thermoelectric materials. For the element of Pr or Dy, there is some problem for the hypothesis of calculation of thermal conductivity thermal conductivity (detail analysis process in reference [39]) so these two elements are low probability. After determining the matrix elements, the different doping elements are chosen to optimize the thermoelectric performance for different systems.

Based on the above analysis, our lab chose La_2S_3 and Gd_2S_3 as a matrix. For La_2S_3, stability was improved by doping different transition metal elements (Ti, Zf) and thermoelectric properties of La_2S_3 were optimized by a novel preparation method. For Gd_2S_3, ternary and non-stoichiometry method were employed to optimize the carrier concentration and the optimized ZT reached 0.51 at 950 K for $NdGd_{1.02}S_3$[43].

1.2 Valence-Fluctuation rare-earth sulfides

1.2.1 Mixed-valence rare-earth sulfide

Mixed-valence or mixed-configuration rare-earth compound and sometime as fluctuating-valence or fluctuating-configuration rare-earth compound are a number of compound with the character of atomic-like f levels and the wide s-d band coexist at the Fermi surface[44]. The nature of fluctuating-valence of rare-earth element is that both the $4f^n$ and $4f^{n-1}$ configurations contribute to the intermediate-valence wavefunction[45]. The mixed-valence state can be thought of as a mixture of $4f^n$ and $4f^{n-1}$ ions, the energies of which are nearly degenerate[45]. Three elements (pressure, temperature and element substitution) can cause these valence-fluctuation phenomena.

In rare earth systems, elements with valence fluctuation feature involving Ce, Sm, Eu, Tm and Yb, are energetically found to be near each other and can be inverted by externally applied or internally generated constraints. Such inversion involves a change in the valence state of the rare earth ion. In this study, we just studied Yb, Eu, and Sm related sulfides.

1.2.2 Property and structure characteristic of valence change rare-earth sulfide

The archetypal valence instability occurs in FCC samarium monosulfide (SmS) due to the pressure-induced phase transformation from semiconducting to metallic phase [46]. Both lattice parameters and resistances of SmS have an abrupt decrease under the effect of pressure without any change in the crystal structure [46]. The reduction of lattice constant is connected with the diameter of Sm ion because the diameter of bivalent and trivalent Sm ion is 1.14 and 0.96 Å, respectively. The reduction of cell constant is attributed to the partial transformation of Sm^{2+} to Sm^{3+} resulting from the hybridization of 4f electrons and the 5d conduction band with the decrease of energy gap. The energy band gap of SmS with NaCl structure reduced from 0.2 eV to 0.065 eV following the increase of pressure to around 6.5 kbr [47].

In order to determine the presence or absence of the mixed-valence and electronic structure, semiconductor and metallic SmS were analyzed by optical reflectivity[48] and angle-resolved photoemission spectroscopy[49]. X-ray absorption and resonance photoemission spectroscopy show mixed valency of Sm^{2+} and Sm^{3+} states in semiconducting SmS at low temperature (T=30 K) and high-resolution temperature-dependent valence-band photoemission spectroscopy show a pseudogap within 20 meV of the Fermi level at low temperatures [50]. In order to further understanding of phase transitions, many SmS-based ternary sulfides were researched.

Other rare earth elements (Y[51, 52], La[53] and Eu[54]) and transition metal elements (nickel [55] and manganese [56]) diffusion in samarium sulfide single crystal, polycrystalline and film were studied to improve the thermovoltaic effect in samarium sulfide based materials.

Europium monosulfide (EuS) is very similar with SmS in crystal structure and atom size. Similar with SmS, EuS also has phase transformation under hydrostatic pressure. The effect of pressure on magnetic transitions of EuS under hydrostatic pressure up to 10 kbars was reported and the magnetic exchange interactions vary in an important way with volume [57]. The behavior of EuS under pressure is an example of the competition between a structural NaCl-CsCl transition and f - d mixing[58].

EuS, as the ideal Heisenberg ferromagnet, had attracted sustained interest as the model crystals for investigations of magnetism in magnetic semiconductors[59]. In NaCl structure of EuS, only nearest-neighbor J_1 and next-nearest-neighbor J_2 exchange interactions are important[60]. the exchange-parameter J_1 and J_2 are in essential agreement with the inelastic-neutron-scattering but in marked disagreement with Swendsen's Green's-function theory and its application to the calculation of the ferromagnetic and paramagnetic Curie temperature[60].

Electron-beam-excited luminescence spectra for EuS show a series of low-energy broad corresponding to $4f^7$-$4f\ 6^5d$ transition and high-energy sharp peaks arising from intra-atomic transitions within the 4f configuration in the Eu ions [61]. A proposed energy level diagram for EuS has been derived previously from the optical data [62]. A slight indication of two crystal-field split 5d subbands can be deduced from the calculated density of states of EuS [62]. EuS microcrystal-embedded oxide thin films [63]and novel EuS nanocrystal containing paramagnetic Mn(II), Co(II), or Fe(II) ions [64] were prepared and their effective optical Faraday effects were investigated.

Specific heat measurements of EuS between 10 K and 35 K show a sharp peak at 16. 2 K and the dominant exchange interaction is between nearest neighbor Eu^{2+} ions [65]. The ferromagnetic Curie temperature of EuS increases linearly for hydrostatic pressures up to 4 kbar at a rate of 0.28 K/kbar because the interaction of the magnetic moments in EuS depends much stronger on the volume than the common superexchange mechanism [66]. The variation of specific heat is connected with the isothermal entropy change so it is meaningful to test the magnetic and thermal properties of EuS for the possible application of magnetic refrigerant materials, which is based on the isothermal entropy change induced by the variation of an applied magnetic field [67]. The high magnetocaloric effect of EuS, as compared to the usual $Gd_3Ga_5O_{12}$, made it as a first candidate for a low field refrigeration cycle (~ 1T)[67].

YbS differed from SmS and EuS by the presence of hole-type conduction and the energy band structure of YbS can be determined with the optical investigations[68]. Diffusive reflection spectra of YbS powders had a step due to electronic transitions with energies near 1.2 eV[68]. The optical-absorption band gap of YbS due to the lowest 4f- 5d transition has been studied as a function of pressure and the rate of closure of this gap with pressure lead to a metal-semiconductor transition in YbS [69]. The optical response and lattice-parameter measurements indicated the onset of a 4f-shell instability near 100 kba [70]. In these above mentioned researches, the influence of pressure on the stability and band structure of YbS had been researched.

In the metallic and semiconductor SmS, both bivalent and trivalent Sm ions had the crystallographic equivalence of the cation sites and a metallic like conductivity band is present near the Fermi energy. Moreover, a thermally activated hopping of the charge carriers occurred for Eu_3S_4 and Sm_3S_4 with the Th_3P_4 structure. However, cations with different valence in Yb_3S_4 occupy inequivalent lattice site so the valence distribution is static and no fluctuation is possible. The energy gaps of Sm3S4 are similar with these of SmS and its band conduction involved a thermal activation of charge carriers and a hopping conduction with temperature dependence frequency factor [71].

1.2.3 Research and application of valence change rare-earth sulfide

Similar with other heavy rare-earth sulfides, there is little research about preparation and characterization of ytterbium monosulfide. SmS based film can be employed as strain-sensing layer of resistant strain gauge. This application is based on the sensitivity of SmS under pressure. On the other hand, SmS based sulfides are expected to be employed as high temperature thermoelectric materials. Kazanin M. M. et al.[72] have optimized thermal electromotive force by slightly variation and control of composition or rare-earth/transition element doping. The mechanism of the formation of thermal electromotive force and influence elements were investigated. The study of EuS is focus on the preparation and characterization of nano-size material to improve the magnetic and optical properties.

1.3 Research purpose and motivation

The reasons for the study of rare earth sulfides were listed in below:

(1) Sulfides are promising candidates for environment-friendly and cost-effective functional materials [73]. The extensive research devoted to the physics and chemistry of rare-earth sulfides during the end of the last century has led to great advances the understanding of the properties of solids in general.

(2) Several years ago, the demand for rare earths is expected to increase because of their expansion into the fields of high-performance motors and automotive exhaust catalysts. However, serious overcapacity is a long-standing problem in China’s rare earths market. China's expanding economy is posing a risk to supply of REEs worldwide [74].

(3) The physical properties of rare-earth compounds are essentially influenced by the rare earth’s 4f electrons[75]. Among the rare-earth compounds there is a fascinating class of solids called intermediate (or homogeneously mixed) valence compounds [75]. To develop the novel application for sulfide related compound is meaningful and important.

(4) Mixed-valence rare earth sulfides had special electrical structures and then possessed many potential applications.

In this task, we dedicated to research on the following topics;

(1) Research of preparation and sulfurization technology of valence fluctuation rare-earth sulfides. In order to achieve industrial production of rare earth sulfides, it is necessary to study the influence of characteristics of starting material on the sulfurization process. Meanwhile, we need to further optimize the sulfurization process based on the former researches. Compared with light rare earth sulfides, crystal structures of heavy rare earth sulfides are more complex. Moreover, there are some difficulties on the preparation of heavy rare earth sulfides, especially for Yb and Lu in our lab. Therefore, this study chose ytterbium sulfide with characteristics of valence fluctuation state as the initial study content. We employed four kinds of Yb_2O_3 with different specific surface area, grain size and particle size distributions as starting materials, systematically researched the influences of sulfurization temperature, sulfurization time, gas-flowing rate, and different sulfurization programs on the

sulfurization products. We wish to understand the influence of characteristics of starting material on the sulfurization processes. Meanwhile, raw materials with different characteristics can be obtained optimal process parameters in order to provide a meaningful reference for future industrial production. The sulfurization process of Eu_2O_3 is different with other rare earth sulfide because there is no Eu_2S_3. Therefore, it is meaningful to systematically study the sulfurization process of Eu_2O_3.

(2) Research of phase transformation processes and sintering for mixed-valence rare earth sulfides. Stability of rare earth sulfides is defining factors of rare earth sulfides during industrialization application. Stability of rare earth sulfides is connected with dissociation energy on the surface layer of sulfide, so the vapor pressure of sulfur affected the stability of rare earth sulfide and phase transformation processes. In this study, synthetic ytterbium sulfides and europium sulfides were treated under different atmospheres to study their stability and phase transformation. We also researched the sintering process for valence fluctuation rare earth sulfides.

(3) Novel and possible application of valence fluctuation rare earth sulfide

For the application of rare earth sulfide, we should consider the different characteristics for different rare earth elements and compounds and then choose different application fields. How to choose the application of rare earth sulfides? What factors need to be considered?

We take EuS as an example. To store and transport hydrogen fuel, it is effective to liquefy hydrogen; therefore, a magnetic refrigerant material with a large specific heat near the liquid hydrogen temperature is required. Near the liquid helium temperature, medium and heavy rare-earth compounds exhibiting large specific heats due to magnetic phase transitions and possessing large total angular momentum quantum numbers are at the level practically required of magnetic refrigerant materials. However, Er_3Ni and $HoCo_2$ have minimum specific heat values near the liquid hydrogen temperature, and oxysulfides that contain heavy rare-earth elements and possess specific heat peaks have small specific heats near the liquid hydrogen temperature. Recently, we discovered that polycrystalline EuS, which also contains a bivalent cation (Eu^{2+}), has a large specific heat peak ($0.7\ J\cdot K^{-1}\cdot cm^{-3}$) near 16.5 K, which is the liquid hydrogen temperature. So, it is interesting and meaningful to research the possibility for EuS as novel magnetic refrigerant material for liquid hydrogen.

Different with YbS and EuS, SmS has small resistivity, so it is possible to be used as high temperature thermoelectric materials. It is expected to optimize the thermoelectric properties by controlling the composition.

Not every valence fluctuation rare earth sulfides (even rare earth sulfide) can find a suitable or possible new application. Such as ytterbium sulfide, it is not fitting for thermoelectric materials due to large resistivity and magnetic refrigerant material. It need further explore for its application.

Chapter 2 Synthesis, sintering and heat capacity of ytterbium sulfides

2.1 Introduction

Rare-earth sulfides have been considered as the candidate for pigments [36, 76, 77], high temperature thermoelectric materials [22, 43], refractory materials [15] and optical materials [78]. Ytterbium sulfides have received considerable attentions for their interesting thermoelectric properties [79] and optical properties. Especially, ytterbium monosulfide (YbS) has been researched as high temperature thermoelectric materials for its p-type electrical conductivity while most rare earth chalcogenides have n-type electrical conductivity [79]. Furthermore, YbS is also expected to be used as refractory materials for its high melting point (2130°C) [80].

In former studies, binary rare-earth sesquisulfide Ln_2S_3 (Ln = rare-earth element) had been formed via the sulfurization of their oxides or salts under CS_2 gas [19, 21, 81, 82]. Moreover, some remarkable breakthroughs have been made on thermoelectric properties of non-stoichiometric ternary and quaternary rare-earth sulfides ($LaGd_{1+x}S_3$ [22], $SmGd_{1+x}S_3$ [22], $SmEuGdS_4$ [83], $NdGd_{1+x}S_3$ [43]) by tuning their chemical compositions with rare-earth element self-doping [84]. These investigations imply the preparations of Ln_2S_3 with CS_2 gas become feasible at lower temperature in comparison with the sulfurization of H_2S gas [85]. The volatile liquid CS_2 is easier to handle for its less toxic compared with H_2S [86]. However, there is no report about the influences of particle size and specific surface area (denoted as SSA hereafter) of Ln_2O_3 on sulfurization process via CS_2 gas.

In literature [80], the sulfurization temperature of 1250 °C is too high for the synthesis of Yb_2S_3. Partial CS_2 molecular decomposed to carbon. Residual carbon affects the color of products, which limited its application as pigment materials. It is necessary to study the possibility of preparing Yb_2S_3 at lower temperature by controlling Yb_2O_3 characters or sulfurizing Yb_2O_3 in proper CS_2 gas flow rate (denoted as GFR hereafter) to lessen residual carbon content.

Different with light rare-earth sesquisulfides, heavy rare-earth sesquisulfide Yb_2S_3 has several polymorphic forms. Hexagonal ε-Yb_2S_3 [87] transforms into monoclinic δ-Yb_2S_3 at 897 °C [12]. Cubic ϕ-Yb_2S_3 with lattice parameter a=10.3 Å transforms into Th_3P_4-type γ-Yb_2S_3 at a higher temperature [12]. In spite of the extensive polymorphisms in Yb_2S_3, the above transformations are not presented in the Yb-S phase diagram [12] with the pressure of 4.5 atmospheres [88]. These phase transformations and sulfurization products are dependent on reaction condition, e. g., Yb_3S_4 phase has been synthesized by the sulfurization of Yb_2O_3 at 1300 °C via H_2S gas [89]. Is it achievable to obtain different polymorphic Yb_2S_3 by control sulfurization condition?

In Yb-S binary system, polymorphic Yb_2S_3, Yb_3S_4[89, 90] and YbS [91] had been checked by electron diffraction. Different with light rare-earth sesquisulfides, Yb_2S_3 has several polymorphic forms. Hexagonal ε-Yb_2S_3 [87] transforms into monoclinic δ-Yb_2S_3 at 897 °C [12]. Cubic ϕ-Yb_2S_3 with lattice parameter a=10.3 Å transforms into Th_3P_4-type γ-Yb_2S_3 at a higher temperature [12]. These phase transformations and sulfurization products are dependent on reaction condition, e. g., Yb_3S_4 phase has been synthesized by the sulfurization of Yb_2O_3 at 1300 °C via H_2S gas [89]. Is it achievable to obtain different polymorphic Yb_2S_3 by control sulfurization condition? Moreover, there is little report about the synthesis of ytterbium sulfides, whether Yb_3S_4 or YbS, by heat treatment of Yb_2S_3 under different atmospheres.

2.2 Experimental details

2.2.1 Characters of Yb_2O_3 powders

Herein, Yb_2O_3 powders provided by different companies (specific surface area 50 m^2/g, purity 99.8%, Shin-Etsu Chemical Co., Ltd., remarked as Yb_2O_3-A; specific surface area 10 ~ 25 m^2/g, purity 99.9%, mean particle size 0.5 ~ 2 μm, NIPPON Yttrium Co., Ltd., remarked as Yb_2O_3-B; particle size 0.37 μm, purity 99.8%, Shin-Etsu Chemical Co., Ltd., remarked as Yb_2O_3-C; specific surface area 2 m^2/g, particle distribution 3 ~5 μm, purity 99.99%, Shin-Etsu Chemical Co., Ltd., remarked as Yb_2O_3-D) were examined.

Figure 2.1 shows SEM microstructure of ytterbia powders with different SSA and particle size. Yb_2O_3-A particle has bigger SSA (Table 2.1) and irregular shape (Figure 2.1a). Compared with Yb_2O_3-A, Yb_2O_3-B has smaller particle size (Figure 2.1b) and SSA. Homogeneous spherical particle of Yb_2O_3-C has a uniform size of ~ 0.37um (Table 2.1 and Figure 2.1c). Polygonal tabular particle of Yb_2O_3-D is different with others Yb_2O_3 and has bigger particle (Figure 2.1d) and smaller SSA (Table 2.1).

Figure 2.2 shows particle size distribution of Yb_2O_3 powders. The average particle size of Yb_2O_3-A is 3.92 μm. The distribution of Yb_2O_3-B reflects a broad range of particle sizes with poor uniformity. Due to the large proportion of particles below 1 micron in size (Figure 2.1), Yb_2O_3-B would have a reunion. The first peak corresponds Yb_2O_3-B primary particles with particle size of ~ 1μm. The agglomerate of Yb_2O_3-B causes average particle size of second particle (7.89μm) is larger than that showed in Figure 2.1b. The particle size distribution of Yb_2O_3-C contains two parts. The left part is primary particle distribution and right part is aggregated particle distribution. For Yb_2O_3-D, the average particle size is large (8.68μm) as showed in Figure 2.1d.

Table 2.1 Information of Yb_2O_3 powders with different characteristic

Raw material	SSA(m^2/g)	Size(μm)	Purity (%)	Producer
Yb_2O_3-A	50	~1	99.8	Shin-Etsu Chemical Co., Ltd.,
Yb_2O_3-B	10~25	0.5 ~ 2	99.9	NIPPON Yttrium Co., Ltd.,
Yb_2O_3-C	13.31	0.37	99.8	Shin-Etsu Chemical Co., Ltd.,
Yb_2O_3-D	2	3 ~ 5	99.99	Shin-Etsu Chemical Co., Ltd.,

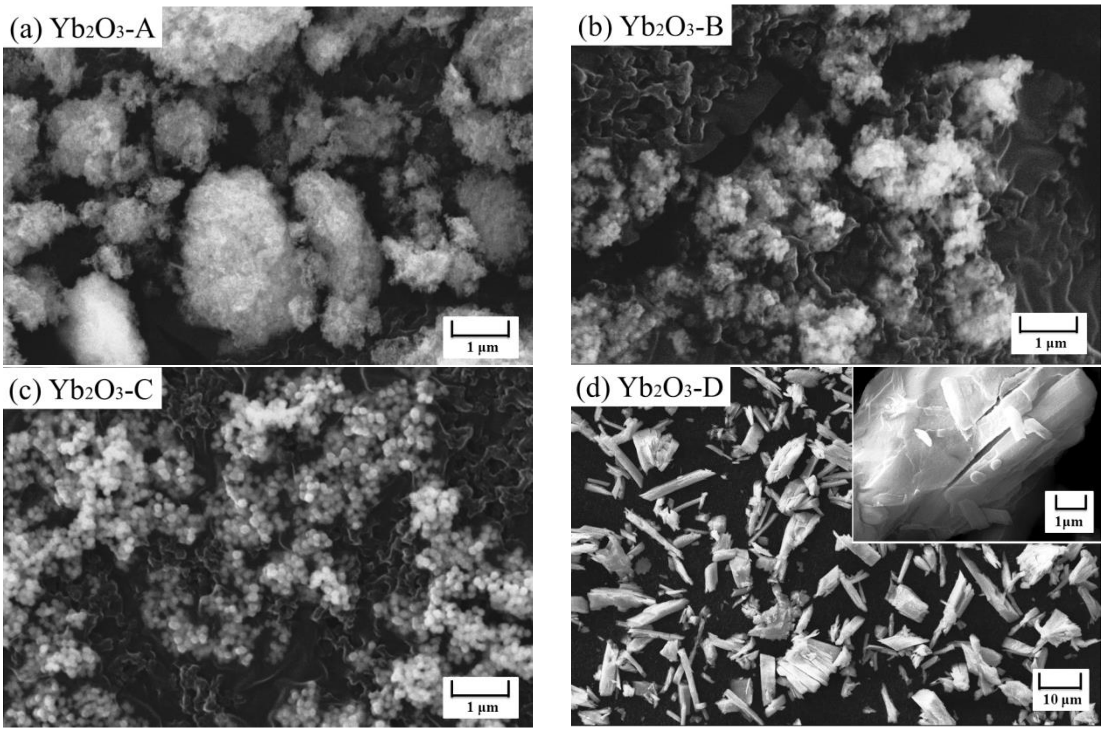

Figure 2.1 SEM images of Yb_2O_3-A (a), Yb_2O_3-B (b), Yb_2O_3-C (c), Yb_2O_3-D (d).

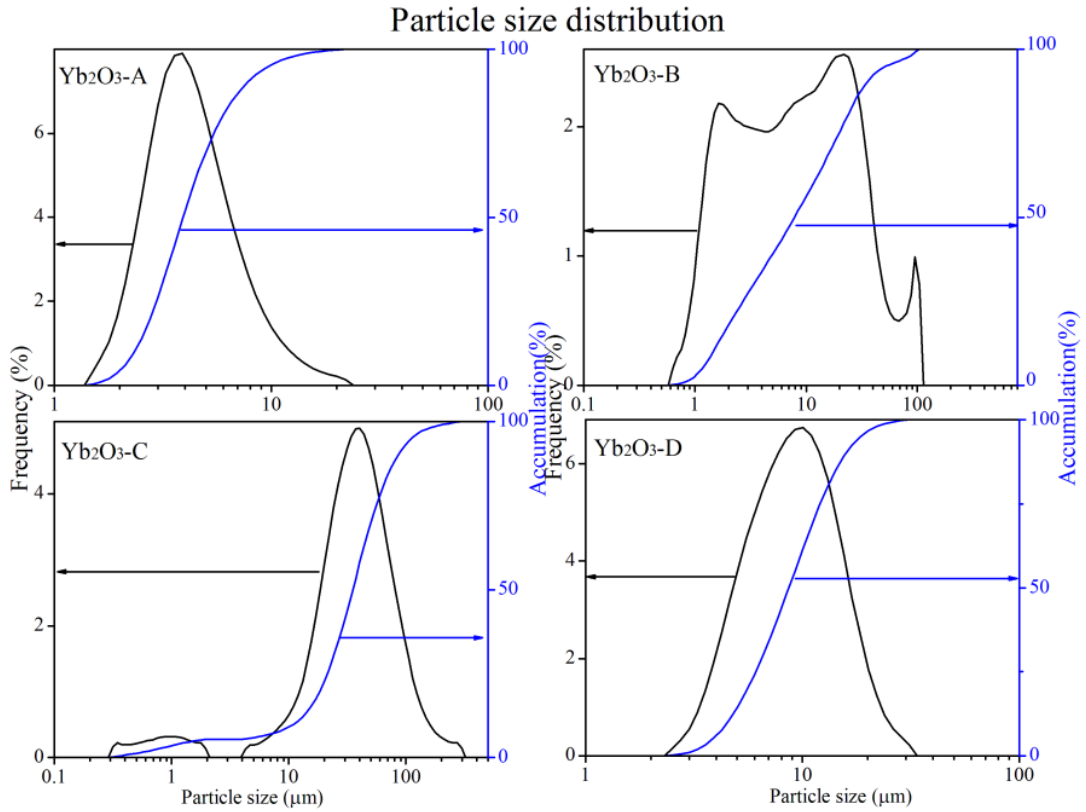

Figure 2.2 Particle size distributions of Yb_2O_3 powders

2.2.2 Sulfurization, heat treatment and sintering of ytterbium sulfides

The sulfurization experiment was conducted via the following procedure. A silica boat loaded with Yb_2O_3 was inserted into a silica-glass tube in the furnace (ARF3-500-60KC, Asahi Rika Mfg. Co., Ltd.) and then the pressure in the tube was pumped into less than 0.1 Pa. After the tube was filled with argon gas, the boat was heated to setting temperature (500 ~ 1050 °C). Reagent-grade liquid CS_2 (Kanto Chemical Co., Tokyo, Japan) was carried into the reactor by flowing carrier argon gas through a bubbler in a flow rate of 0.83 mL/s ~ 3.33 mL/s. The sulfurization experiments were continued up to 0.5 ~ 8 hr. The reactor system was cooled to room temperature in a stream of Ar gas.

The heat treatments of synthetic Yb_2S_3 contain three conditions; 1) 1000 ~1050 °C for 3 hr ~ 12 hr under Ar/CS_2 or Ar gas: three grams of synthetic Yb_2S_3 were treated with the same apparatus for sulfurization. 2) 1000 ~1500 °C for 1 hr ~ 5 hr under vacuum less than 1.2×10^{-3} Pa: above one grams of synthetic single orthorhombic η-Yb_2S_3 or hexagonal ε-Yb_2S_3 was placed on a BN boat (inner diameter of 15 mm) and inserted into an alumina tube. The reactor system was heated to 500-1550 °C with 10 °C/min. 3) Closed system: synthetic Yb_2S_3 was placed in a graphite die (inner diameter of 10.5 mm) and cold pressed under a uniaxial applied stress of 25 MPa. And then it was sintered at 1000 ~ 1400 °C with heating rates of 0.42 K·s^{-1} under 50 MPa by spark plasma sintering (Model SPS-511L, Sumitomo Coal Mining Co. Ltd, Tokyo, Japan). The sintering vacuum is lower than 7×10^{-3} Pa. And then synthetic Yb_3S_4 or YbS powders were sintered at 1000°C-1900 °C for 1- 5 hr under 50 MPa by spark plasma sintering.

2.2.3. Analysis and characterization of as-synthesized materials

X-ray diffraction (XRD, Model Rint-Ultima+, Rigaku Corp., Tokyo, Japan) with monochromatic Cu Kα radiation at 40 kV and 20 mA was applied to check phase compositions of sulfurization products and polymorphic forms of Yb_2S_3. Cell parameters of synthetic powders were measured with the scan step of 1.0×10^{-3} degree for 2s. The reaction degree was estimated from the normalized intensities of the diffraction lines of each reaction product. Morphology of synthetic Yb_2S_3 was characterized by scanning electron microscopy (SEM, JSM-5310LV, JEOL Ltd. Tokyo, Japan) to study the change of Yb_2O_3 powders before and after sulfurization. The effect of impurity content on particle size of Yb_2S_3 powders was also studied.

Chemical compositions of synthetic powders were measured by oxidizing them to stoichiometric Yb_2O_3. And 0.2~0.5 g of each powder was placed in a quartz crucible and inserted into an electric furnace. The powders were heated to 1000 °C for 3 hr with heating rate of 0.37 °C·s^{-1} and subsequently cooled to room temperature in air. The thermal analysis showed that Yb_2S_3 was completely oxidized to Yb_2O_3 at 800 °C. Ytterbium (Yb) content and sulfur (S) content were calculated from the weight of Yb_2O_3 and weight change caused by the complete oxidation of the sulfide to the oxide. The oxygen content and carbon content of synthetic powders were determined by an oxygen determinator (Model TC-436, LECO Corp., St. Joseph, MI) and a carbon determinator (Model CS-444LS, LECO Corp., St. Joseph, MI), respectively.

SSA of synthetic Yb_2S_3 was measured by a surface area and pore size analyzer (AUTOSORB-1, QUANTACHROME INSTRUMENTS, Florida, USA) using the Multi-point Brunauer, Emmett and Teller (BET) method with N_2 adsorption to indirectly reveal particle size of sulfurization product. Particle size distributions of Yb_2O_3 and Yb_2S_3 were measured by laser diffraction particle size distribution analyzer (Nikkiso Co, Ltd., Japan).

The thermal-relaxation technique was employed for specific heat measurement in the temperature range between 2 and 100 K by using a physical properties measurement system (PPMS, Quantum Design).

2.3 Sulfurization of ytterbium sesquisulfides

In this study, four kinds of Yb_2O_3 powders with different characters (remarked as Yb_2O_3-A~D, detail informations listed in Table 1) were sulfurized via CS_2 gas to investigate the influence of Yb_2O_3 characters on fabrication of single Yb_2S_3 phase. The chemical compositions of sulfurization products were measured. Dependences of temperature on the formation of Yb_2S_3 were systematically researched. Morphology and SSA of sulfurization products were characterized. Based on experimental results, the elements on sulfurization reaction rate were discussed and synthesis process of Yb_2S_3 was compared with that of light Ln_2S_3.

2.3.1 XRD results of Yb_2S_3

Figure 2.3 shows representative XRD patterns of synthetics with sulfurization at 600 ~1050 °C for 0.5 ~ 8 hr and GFR of 1.67 mL/s. In Figure 2.3a, a new polymorphic form of Yb_2S_3 (named η-Yb_2S_3) formed by the sulfurization of Yb_2O_3-A at 600°C for 8 hr. This η-Yb_2S_3 poses similar XRD pattern and lattice plane (Table 2.2) with those of η-Lu_2S_3 with orthorhombic structure [92], which has a space group of Fddd (Sc_2S_3 type)[93]. Single η-Yb_2S_3 can be gained at 600 ~ 900 °C for Yb_2O_3-A. Hexagonal Yb_2S_3 phase (named ε-Yb_2S_3) formed at 1000 °C for 1 hr. For higher sulfurization temperature of 1050 °C, the intensities of ε-Yb_2S_3 characteristic peaks strengthened while those of η-Yb_2S_3 weakened. Moreover, the mass content of ε-Yb_2S_3 is 20.9% at 1000 °C for 1 hr and 57.8% at 1050 °C for 0.5 hr, respectively.

For the sulfurization of Yb_2O_3-B, single η-Yb_2S_3 phase appeared at 700 °C for 4 hr. Different with the sulfurization of Yb_2O_3-A, ε-Yb_2S_3 phase formed at 800 °C for 3 hr with the mass content of 4.88%. The ε-Yb_2S_3 becomes main phase with the mass content of 75.7% and weak peaks of η-Yb_2S_3 have been perceived simultaneously at 900 °C for 2 hr. The products completely translated into ε-Yb_2S_3 phase at 1000 °C for 1 hr. Single ε-Yb_2S_3 phase can be obtained for a short sulfurization time of 0.5 hr at 1050 °C.

In the sulfurization of Yb_2O_3-C, the formation temperature of η-Yb_2S_3 or ε-Yb_2S_3 is similar with that of Yb_2O_3-B. Small amount of ε-Yb_2S_3 phase formed at 900 °C, which is lower than that of Yb_2O_3-A (1000°C). The content of ε-Yb_2S_3 phase increased following temperature increase. Single ε-Yb_2S_3 phase can be gained with the sulfurization of Yb_2O_3-C at 1000 °C for 1 hr and 1050 °C for 0.5 hr.

Different with the former sulfurization results, Yb_2O_2S appeared as a transitional product for the sulfurization of Yb_2O_3-D. Yb_2O_2S and ε-Yb_2S_3 phase coexisted at 950 ~ 1050 °C for 3 ~ 8 hr. Moreover, the intensities of characteristic peaks of ε-Yb_2S_3 obviously added while those of Yb_2O_2S decreased following temperature increase.

Table 2.2 X-ray diffraction patterns for η-Yb_2S_3 and η-Lu_2S_3

Miller indices			d-spacing (nm)		Intensity	
h	k	l	Yb_2S_3	Lu_2S_3	Yb_2S_3	Lu_2S_3
1	1	1	0.60856	0.60445	65	49
0	0	4	0.57703	0.57182	10	7
0	2	2	0.49111	0.48732	14	11
1	1	5	0.37254	0.3695	30	18
2	0	2	0.36747	0.3651	5	5
1	3	1	0.3246	0.32225	15	11
2	2	0	0.31544	0.31337	44	38
0	2	6	0.31384	0.31118	40	37
1	1	7	0.29222	0.28974	7	7
0	0	8	0.28851	0.28591	3	2
2	2	4	0.27678	0.27481	8	5
2	0	6	0.27306	0.27098	100	100
0	4	0	0.27135	0.26934	50	49
1	3	5	0.2673	0.26521	11	7
3	1	1	0.24993	0.24836	6	6
0	4	4	0.24555	0.24366	3	2
1	3	7	0.23249	0.23061	3	4

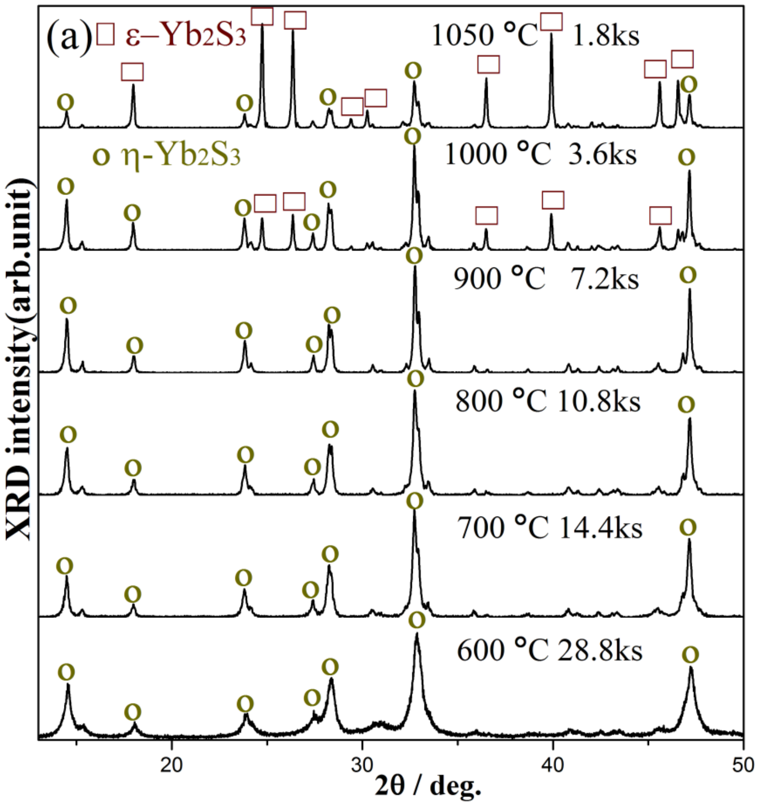
(a)
□ ε–Yb2S3
o η-Yb2S3
1050 °C 1.8ks
1000 °C 3.6ks
900 °C 7.2ks
800 °C 10.8ks
700 °C 14.4ks
600 °C 28.8ks
XRD intensity(arb.unit)
20
30
40
50
2θ / deg.

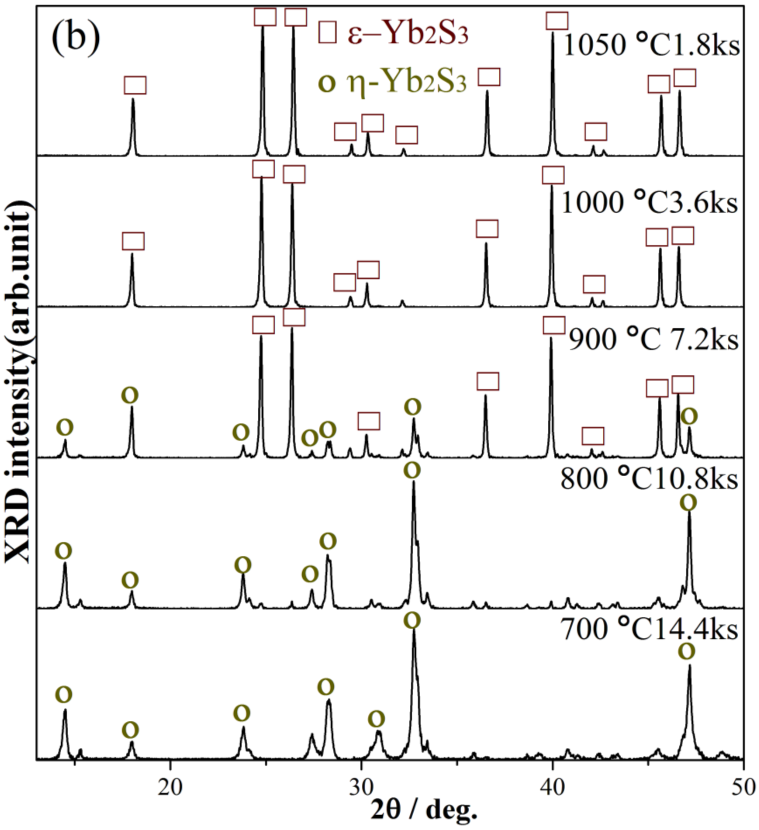
(b)
□ ε–Yb2S3
o η-Yb2S3
1050 °C1.8ks
1000 °C3.6ks
900 °C 7.2ks
800 °C10.8ks
700 °C14.4ks
XRD intensity(arb.unit)
20
30
40
50
2θ / deg.

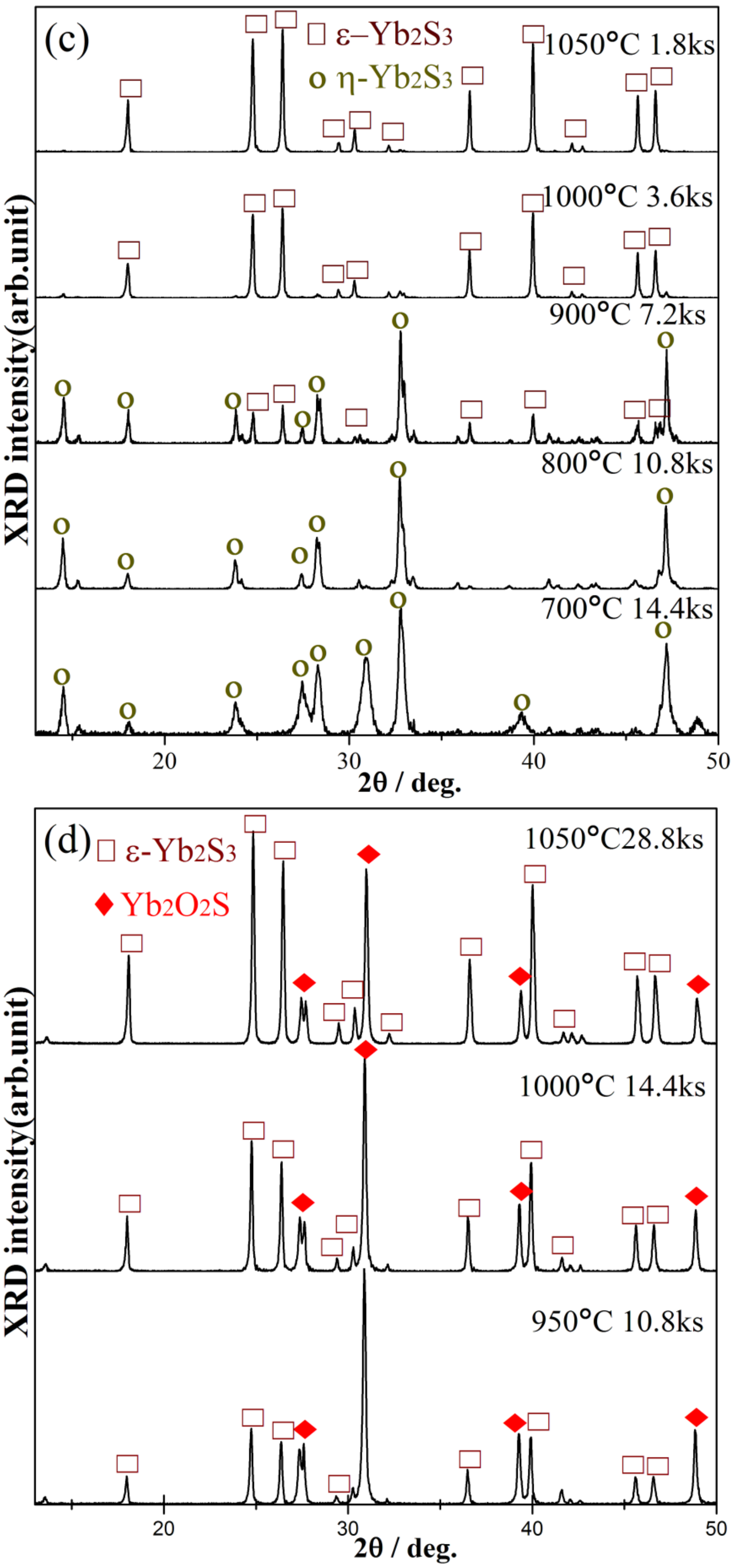

Figure 2.3 XRD patterns of samples produced by the sulfurization of Yb_2O_3-A (a), Yb_2O_3-B (b), Yb_2O_3-C (c) and Yb_2O_3-D (d) with gas flow rate of 1.67 mL/s.

Chemical compositions of sulfurization products with GFR of 1.67 mL/s are listed in Table 2.3. Yb content of η-Yb_2S_3 is close to 78.28%, which suggests this η-Yb_2S_3 is an isomer of Yb_2S_3. For Yb_2O_3-B, the minimum of impurity content of 0.02% grained at 1050 °C for 0.5 hr while the minimum of impurity content is 0.06% for Yb_2O_3-C sulfurized at 1000 °C for 1 hr.

Table 2.3 Chemical composition of Yb_2S_3 with gas flow rate of 1.67 mL/s

Starting materials	Sulfurization		Product	Composition (mass %)		
	°C	hr		Yb	S	Impurity
Yb_2O_3-A	1050	0.5	M-Yb_2S_3	77.88	21.61	0.52
Yb_2O_3-B	700	4	η-Yb_2S_3	78.69	20.79	0.52
Yb_2O_3-B	800	3	M-Yb_2S_3	78.53	21.15	0.32
Yb_2O_3-B	900	2	M-Yb_2S_3	78.23	21.70	0.07
Yb_2O_3-B	1000	1	ε-Yb_2S_3	77.87	21.61	0.53
Yb_2O_3-B	1050	0.5	ε-Yb_2S_3	78.30	21.69	0.02
Yb_2O_3-C	900	2	M-Yb_2S_3	78.53	21.16	0.31
Yb_2O_3-C	1000	1	ε-Yb_2S_3	78.32	21.62	0.06
Yb_2O_3-C	1050	0.5	ε-Yb_2S_3	78.57	21.05	0.37

Theory value W_{Yb}= 78.28%; Ws= 21.72%; M-Yb_2S_3: mixture of η-Yb_2S_3 and ε-Yb_2S_3.

2.3.2 Dependence of temperature, time and GFR on the formation of Yb_2S_3

Figure 2.4 shows temperature dependences of diffraction intensity of Yb_2O_3 (222), Yb_2O_2S (011), η-Yb_2S_3 (206) and ε-Yb_2S_3 (110) formed via the sulfurization of Yb_2O_3 at 700 °C ~ 1000 °C for 1 hr and 3 hr with GFR of 1.67 mL/s. The reaction sequence is Yb_2O_3→Yb_2O_2S→η-Yb_2S_3→ ε-Yb_2S_3 with increasing temperature. However, there is no intermediate product Yb_2O_2S occurred for the sulfurization of Yb_2O_3-A because larger specific surface area does not only increase the adsorption of CS_2, but also supply a large interface. This interface accelerates the solid-gas reaction rate. For Yb_2O_3-B and Yb_2O_3-C, Yb_2O_2S faded at 800 °C and the formation of Yb_2S_3 was similar.

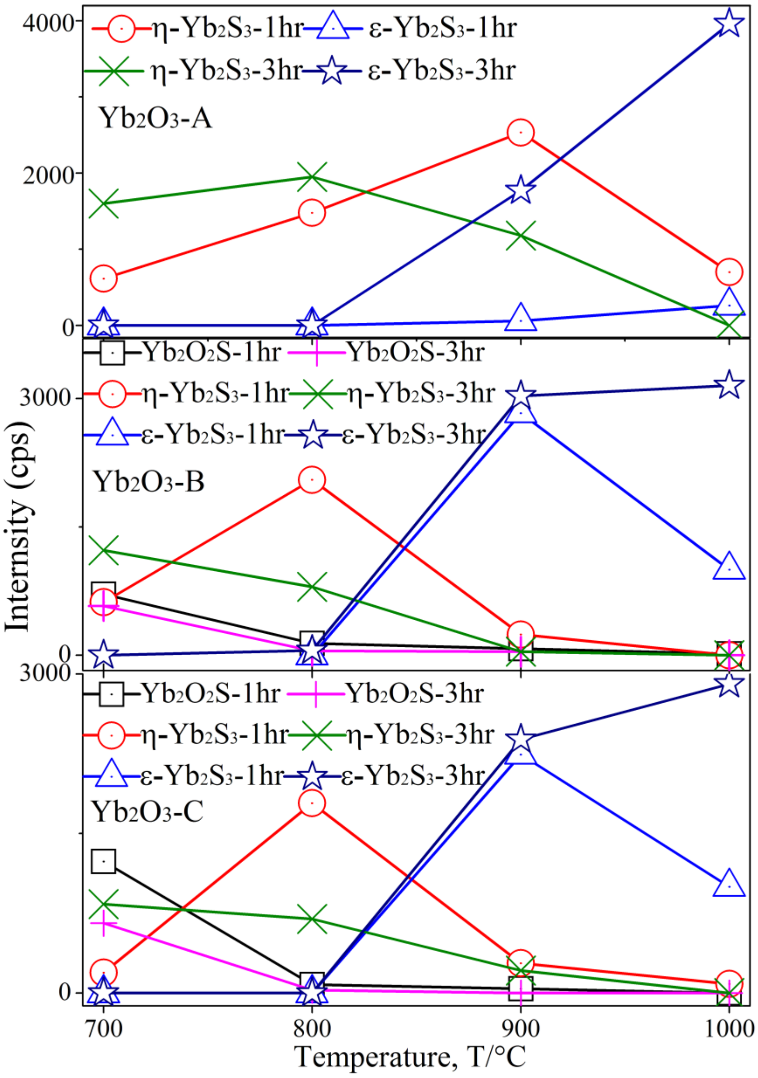

Figure 2.4 Temperature dependences of diffraction intensity of reaction product formed via the sulfurization of Yb_2O_3 for 1 hr or 3 hr with gas flow rate of 1.67 mL/s.

Figure 2.5 shows temperature dependences of diffraction intensity of Yb_2O_3 (222), Yb_2O_2S (011), η-Yb_2S_3 (206) and ε-Yb_2S_3 (110) formed via the sulfurization of Yb_2O_3 at 500 °C ~ 1050 °C for 8 hr with GFR of 0.83 mL/s. For the sulfurization of Yb_2O_3-A, single η-Yb_2S_3 phase appeared at 600 °C, reached its maximum intensity at 950 °C and disappeared at 1000°C. Orthorhombic η-Yb_2S_3 phase was observed at 700°C for Yb_2O_3-B and Yb_2O_3-C powders, and the maximum of diffraction intensity of η-Yb_2S_3 was detected at 850°C for Yb_2O_3-B and 800 °C for Yb_2O_3-C powders, respectively.

Different with the sulfurization process of Yb_2O_3-A, Yb_2O_2S phase emerged as intermediate product. Yb_2O_2S phase was observed at 700 °C for Yb_2O_3-B and Yb_2O_3-C. The corresponding maximum diffraction intensity of Yb_2O_2S was detected at 700°C, and disappeared at 800 °C for Yb_2O_3-B and 930°C for Yb_2O_3-C, respectively.

Hexagonal ε-Yb_2S_3 emerged at different temperature and enhanced gradually as the temperature increased. Single-phase ε-Yb_2S_3 was confirmed at above 1000°C except for the sulfurization of Yb_2O_3-D. For the sulfurization of Yb_2O_3-D, Yb_2O_2S phase existed until 1050 °C for 8 hr.

The compositions of synthetics sulfurized for 8 hr were listed in Table 2.4. For Yb_2O_3-A, sulfurization product is single η-Yb_2S_3 at 600~ 850 °C (Figure 2.5) and its composition becomes equal to theoretical value of Yb_2S_3. The impurity content of Yb_2S_3 formed by sulfurized Yb_2O_3-B at 930 °C for 8 hr increased to 0.78% but the impurity content reduced to 0.22% for the sulfurization of Yb_2O_3-C at same conditions.

The oxygen content and carbon content for ε-Yb_2S_3 produced by sulfurized Yb_2O_3-C at 1050°C for 8 hr with GFR of 3.33 mL/s were 0.62% and 0.86%, respectively. When GFR lessened to 0.83 mL/s, the oxygen content and carbon content were 0.48% and 0.23%, respectively. It showed the impurity contents of Yb_2S_3 powders are dependent on GFR. Therefore, purer samples can be made in proper GFR and sulfurization temperature to void the decomposition of excess CS_2 gas.

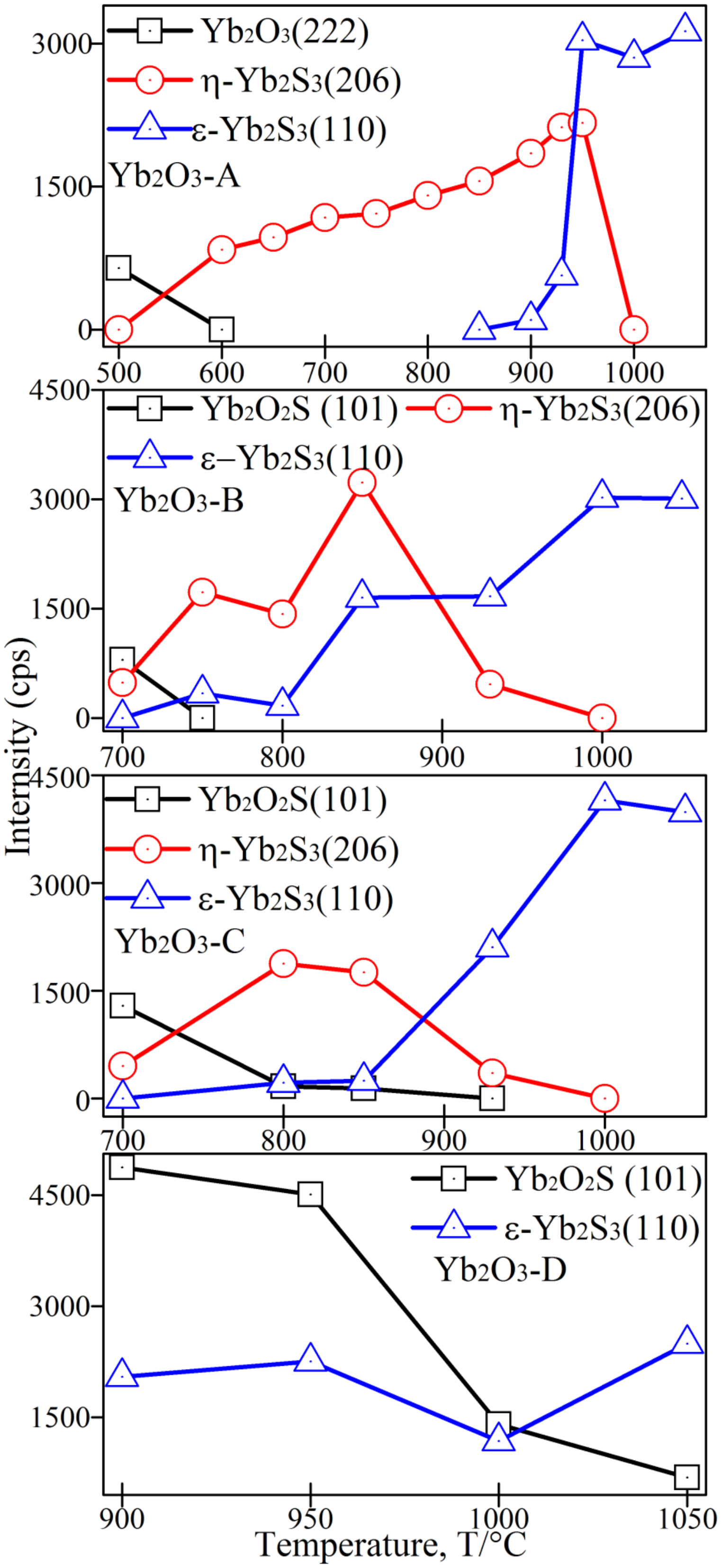

Figure 2.5 Temperature dependences of diffraction intensity of reaction products formed the sulfurization of Yb_2O_3 for 8 hr with gas flow rate of 0.83 mL/s.

Table 2.4 Chemical composition of Yb_2S_3 sulfurized for 8 hr

Starting materials	Condition		Product	Composition (mass %)		
	°C	mL/s		Yb	S	Impurity
Yb_2O_3-A	850	0.83	η-Yb_2S_3	78.07	21.66	0.27
Yb_2O_3-B	930	0.83	M-Yb_2S_3	78.88	20.34	0.78
Yb_2O_3-C	850	0.83	M-Yb_2S_3	78.58	21.03	0.39
Yb_2O_3-C	930	0.83	M-Yb_2S_3	78.11	21.67	0.22
Yb_2O_3-C	1050	0.83	ε-Yb_2S_3	78.0	21.7	0.71
Yb_2O_3-C	1050	3.33	ε-Yb_2S_3	77.5	21.4	1.48

Theory value W_{Yb}= 78.28%; Ws= 21.72%; M-Yb_2S_3: mixture of η-Yb_2S_3 and ε-Yb_2S_3.

2.3.3 Morphology, particle size distribution and specific surface area of Yb_2S_3

Figure 2.6 shows typical SEM micrographs of Yb_2S_3 formed by the sulfurization of Yb_2O_3-A powders. The shape of η-Yb_2S_3 produced at 700°C for 1 hr with GFR of 1.67 mL/s (Figure 2.6a) is similar with that of Yb_2O_3-A (Figure 2.1a). Following sulfurization temperature increased to 1000 °C, η-Yb_2S_3 phase transformed to ε-Yb_2S_3 phase (Figure 2.6b).

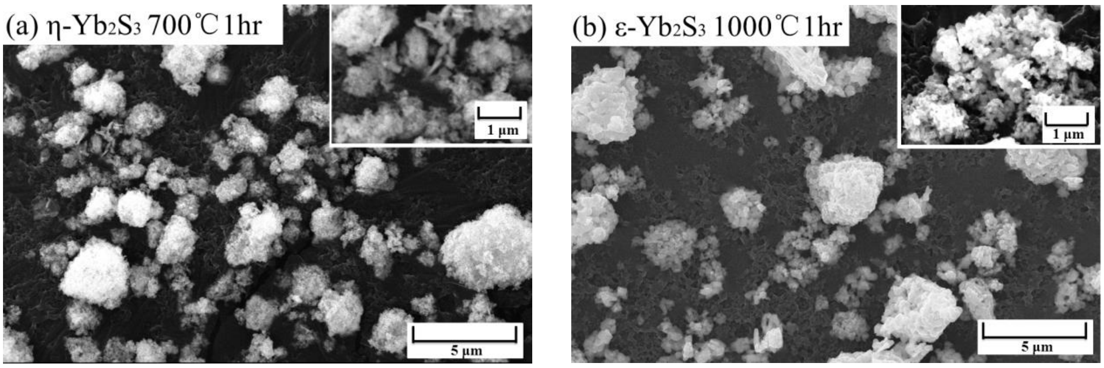

Figure 2.6 SEM micrographs of Yb_2S_3 by sulfurized Yb_2O_3-A at 700°C (a) and 1000°C (b) for 1hr with gas flow rate of 1.67 mL/s.

Figure 2.7 shows SEM micrographs of Yb_2S_3 prepared by the sulfurization of Yb_2O_3-B at 800 ~ 1050 °C for 1 hr with GFR of 1.67 mL/s. Figure 2.7a shows the partial agglutination of single η-Yb_2S_3 phase. In Figure 2.7b, the sulfurization product has larger particle size than that of η-Yb_2S_3 in Figure 2.7a, implying that η-Yb_2S_3 particle grows as the temperature increases to 900 °C. From 900 °C to 1000°C, residual η-Yb_2S_3 (mass fraction 24%) transformed to single ε-Yb_2S_3, which was accelerated by increase of impurity content (Table 2.3), just like the effecting of carbon on the sintered La_2S_3 powders[81]. The important point to note is particle size of single ε-Yb_2S_3 reduces after sulfurization at 1050°C.

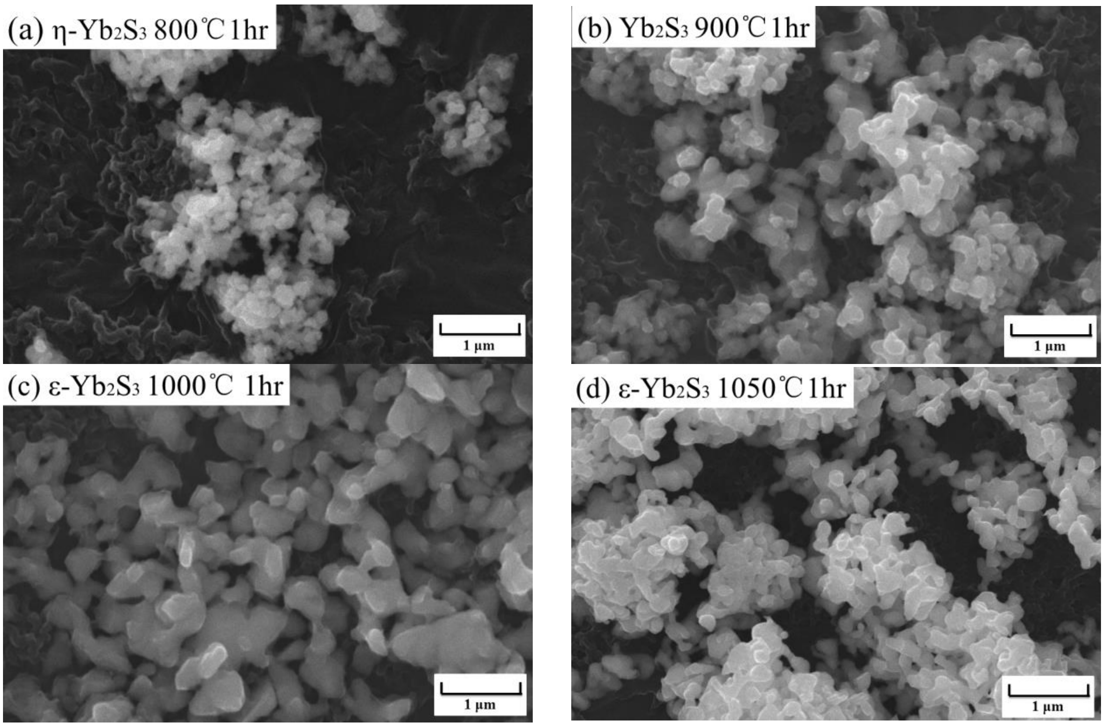

Figure 2.7 SEM micrographs of Yb_2S_3 formed by the sulfurization of Yb_2O_3-B at 800°C (a), 900°C (b), 1000 °C (c) and 1050 °C (d) for 1hr with gas flow rate of 1.67 mL/s.

Figure 2.8 shows SEM micrographs of Yb_2S_3 produced by the sulfurization of Yb_2O_3-C powders with GFR of 1.67 mL/s. In Figure 2.8a and 2.8b, particle size of η-Yb_2S_3 is bigger than that of primary Yb_2O_3-C particles (Figure 2.1c). It is mainly due to sulfur atom having a bigger diameter than oxygen atom. During the sulfurization process, oxygen atoms in sites of Yb_2O_3 lattice are replaced by sulfur atoms and the density lessens from 9.22 g/cm^{-3} of Yb_2O_3 to 6.02 g/cm^{-3} of Yb_2S_3. On the other hand, the agglomeration of Yb_2S_3 produces rounded balls with different size, which did not occurred during sulfurization processes of other Yb_2O_3. The formation of Yb_2S_3 rounded balls can be explained by three aspects: 1) homogeneous spherical Yb_2O_3-C particles were sulfurized with same reaction rate; 2) spherical Yb_2S_3 particle clustered together to lessen surface free energy; 3) volume shrinkage of phase transformation of Yb_2S_3 accelerated the formation of Yb_2S_3 ball. Figure 2.8c and Figure 2.8d show morphology of ε-Yb_2S_3 phase. The average particle size of ε-Yb_2S_3 balls (top right of Figure 2.8d) is lower than that of η-Yb_2S_3 balls (top right of Figure 2.8a).

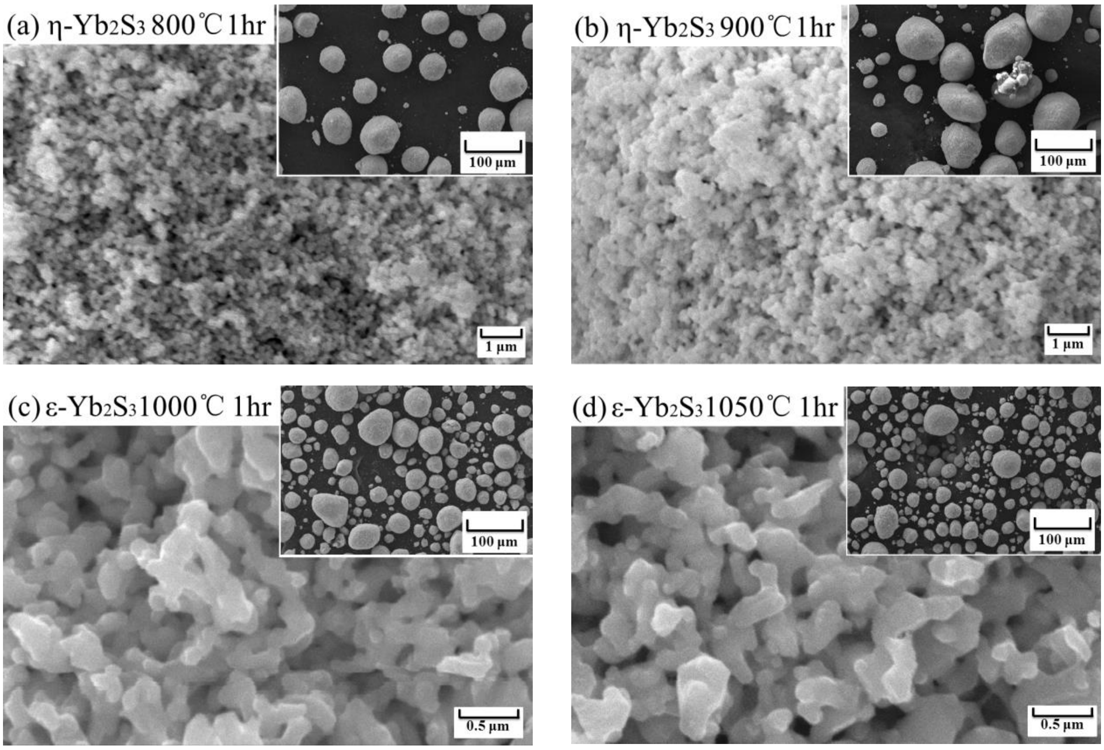

Figure 2.8 SEM micrographs of Yb_2S_3 formed by the sulfurization of Yb_2O_3-C at 800°C (a), 900°C (b), 1000 °C (c) and 1050 °C (d) for 1 hr with gas flow rate of 1.67 mL/s.

Figure 2.9 shows typical SEM micrographs of synthetic η-Yb_2S_3 powders by sulfurized Yb_2O_3-A at 650 °C (a), 750 °C (b) and at 850 °C (c) for 8 hr with flow rate of 0.83 mL/s. Figure 2.9a, the shape of synthetic η-Yb_2S_3 is similar with that of Yb_2O_3-A. The particle size of Yb_2S_3 is bigger than that of Yb_2O_3 due to sulfur having a bigger diameter than oxygen. During the sulfurization process, the sites of oxygen in Yb_2O_3 lattice are replaced by sulfur, the grain grows, and the density decrease from 9.22 g/cm^{-3} of oxide to 6.17 g/cm^{-3} of sesquisulfide.

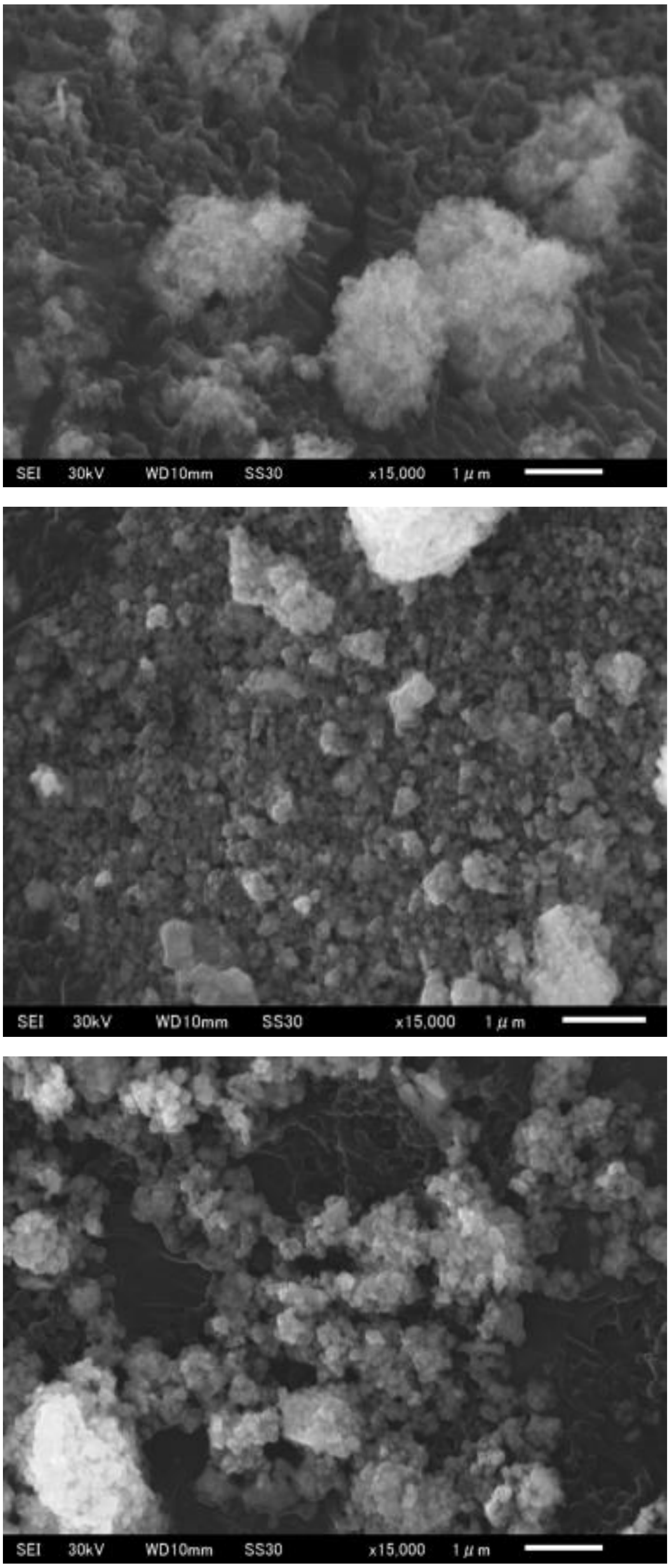

Figure 2.9 SEM images of η-Yb_2S_3 by sulfurized Yb_2O_3-A at 650 °C (a), 750 °C (b) and 850 °C (c) for 8 hr with flow rate of 0.83 mL/s.

Figure 2.10 shows particle size distribution of synthetic orthorhombic η-Yb_2S_3 sulfurized at 800 °C and hexagonal ε-Yb_2S_3 sulfurized at 1000 °C. In Figure 2.10a, the average particle size of orthorhombic η-Yb_2S_3 is 5.27μm for Yb_2O_3-A, 11.83 μm for Yb_2O_3-B and 41.24 μm for Yb_2O_3-C. However, average particle size of hexagonal ε-Yb_2S_3 (Figure 2.10b) is 3.71μm for Yb_2O_3-A, 10.00 μm for Yb_2O_3-B and 40.77 μm for Yb_2O_3-C, which is smaller than that of orthorhombic η-Yb_2S_3 because of the volume shrinkage of Yb_2S_3 during phase transformation. Both orthorhombic η-Yb_2S_3 and hexagonal ε-Yb_2S_3 have larger particles than that of their oxides for three kinds of Yb_2O_3.

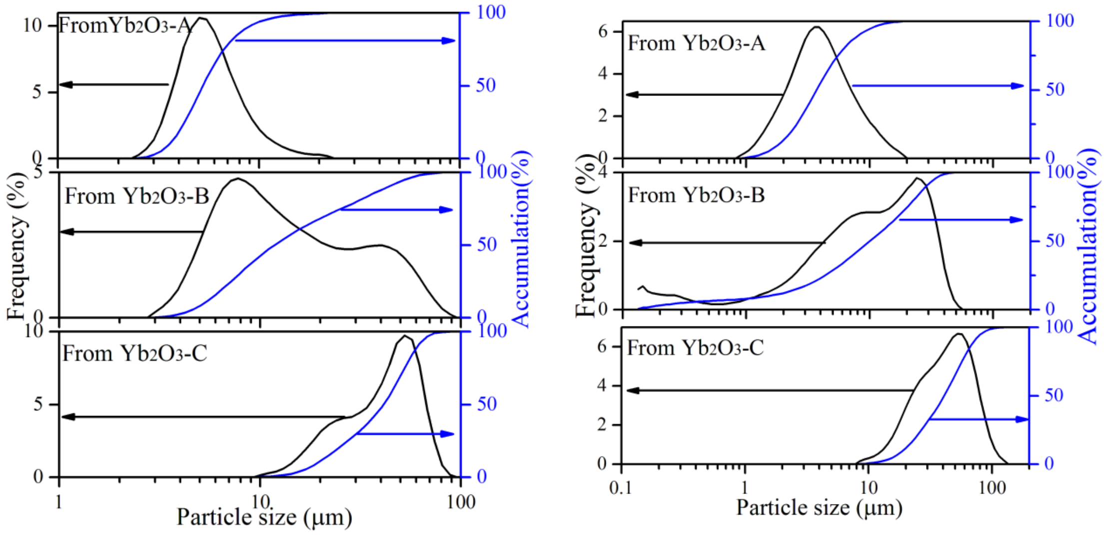

Figure 2.10 Particle size distributions of η-Yb_2S_3 (a) sulfurized at 800 °C and ε-Yb_2S_3 (b) sulfurized at 1000 °C

Figure 2.11 shows SSA results of Yb_2S_3 formed by sulfurized Yb_2O_3-A~C at 700 ~ 1050°C for 1 hr with CS_2 gas flow rate of 1.67 mL/s. For Yb_2O_3-A, SSA of single η-Yb_2S_3 lessened as temperature increased to 900 °C, which is attributed to the growth of η-Yb_2S_3 crystals. According to Figure 2.3a, the transformation of orthorhombic-to-hexagonal Yb_2S_3 phase was accelerated from 1000°C to 1050°C. The volume shrinkage of Yb_2S_3 during phase transformation leaded to the addition of SSA value.

SSA of Yb_2S_3 formed by sulfurized Yb_2O_3-B decreases to minimum and then rose with temperature. This variation implies particle size of Yb_2S_3 increases and then decreases from 800 °C to 1050 °C, which is consistent with SEM micrographs of Yb_2S_3 as shown in Figure 2.7. For Yb_2O_3-C, SSA of Yb_2S_3 reduces from 800 °C to 900 °C, which is similar with those of Yb_2O_3-A and Yb_2O_3-B. According to SEM results in Figure 2.8, the average particle size of ε-Yb_2S_3 is smaller than that of η-Yb_2S_3, so SSA of ε-Yb_2S_3 increases at 1000 °C.

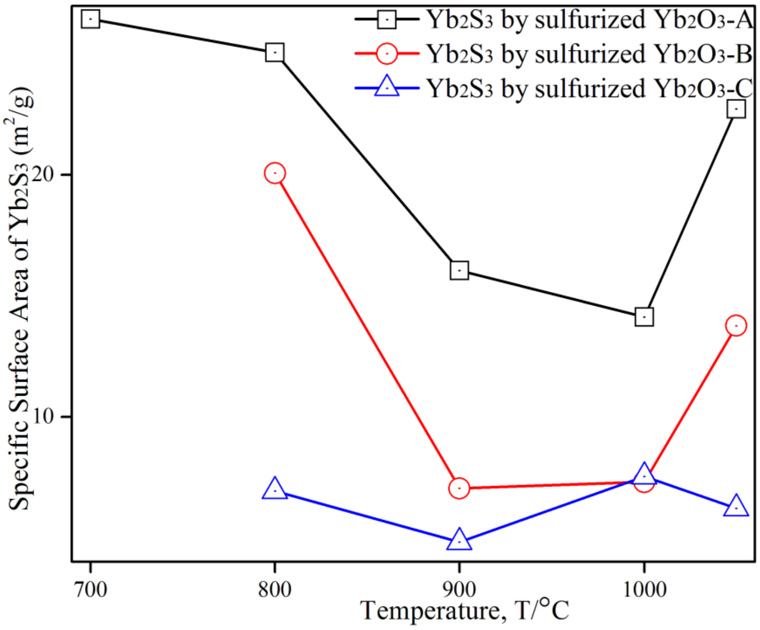

Figure 2.11 Specific surface area of Yb_2S_3 from Yb_2O_3-A ~C sulfurized at 700 ~ 1000 °C for 1 hr with gas flow rate of 1.67 mL/s.

2.3.4 Kinetic analysis of reaction rate

The sulfurization reaction mainly depends on three elements: 1) whether CS_2 gas adsorption is above the critical value for the diffusion through the boundary layer; 2) the formation and diffusion of an interface of Yb_2O_2S or Yb_2S_3; 3) discharge rate of generated CO_2 gas. The reaction proceeds as follows:

$$2Yb_2O_3\ (s) + CS_2\ (g) \rightarrow 2Yb_2O_2S\ (s) + CO_2\ (g) \qquad (1)$$

$$Yb_2O_2S\ (s) + CS_2\ (g) \rightarrow Yb_2S_3\ (s) + CO_2\ (g) \qquad (2)$$

The effect of GFR is dependent on SSA of Yb_2O_3. When GFR becomes 0.83 mL/s, larger SSA of Yb_2O_3-A supplies more chance for CS_2 molecules to adsorb on the surface of Yb_2O_3 particle (Figure 2.1), which can promote the gas-solid reaction occurrence. It is the reason single η-Yb_2S_3 can be prepared at relative low sulfurization temperature of 600 °C (Figure 2.3).

Following SSA of Yb_2O_3-B powders reduced to 10~25 m^2/g, the interplay of Yb_2O_3-B particle leads CS_2 adsorption capacity receded. Yb_2O_3-C powders have similar SSA and particle size with Yb_2O_3-B, so sulfurization products are similar in Figure 2.3c and Figure 2.4. Therefore, single η-Yb_2S_3 cannot be obtained from Yb_2O_3-B~D at 600°C ~ 800°C with GFR of 0.83 mL/s (Figure 2.4). If GFR is 1.67 mL/s, enough CS_2 molecules adsorb on the surface of every Yb_2O_3 particle and the sulfurization reaction can be completed. So there is no Yb_2O_2S in Figure 2.3b and

Figure 2.3c.

Particle size of Yb_2O_3 is the main affecting factor for the formation and diffusion of the interface of Yb_2O_2S or Yb_2S_3. According to SEM results in Figure 2.1, the diffusion of this interface can be quickly completed for Yb_2O_3-B and Yb_2O_3-C because particle size of Yb_2O_3-B or Yb_2O_3-C is smaller than that of Yb_2O_3-A, so single ε-Yb_2S_3 phase can be prepared by the shorter time of 1 hr at 1000 °C or 0.5 hr at 1050 °C (Figure 2.3). Moreover, sphere Yb_2O_3-C particles are easy to bond together and produce Yb_2S_3 balls (Figure 2.7).

For Yb_2O_3-D, the existence of Yb_2O_2S can be explained in three aspects: 1) SSA of Yb_2O_3-D is too small to absorb enough CS_2 molecules with GFR of 1.67 mL/s; 2) particle size of Yb_2O_3-D is too large to finish sulfurization process completely; 3) the diffusion of generated CO_2 from inner to outside was bated at a certain degree. Hence, the inner of Yb_2O_3 particle is difficult to be sulfurized to Yb_2S_3 but turned to Yb_2O_2S at above 1000°C (Figure 2.2d and Figure 2.4).

Compared with the sulfurization processes of four sets of recipes, small particle size and large SSA are necessary for preparation of single ε-Yb_2S_3 and appropriate GFR (1.67 mL/s) can accelerate the sulfurization reaction. Bigger specific surface area lessens the sulfurization temperature to 600 °C due to enhancement of CS_2 adsorbing capacity on the surface of every Yb_2O_3-A particle.

2.3.5 Comparison of synthesis process of rare-earth sesquisulfides

Table 2.5 shows the particle sizes of starting materials and minimum sulfurization temperature required for single Ln_2S_3 phase. In addition, the oxygen and carbon contents of Ln_2S_3 obtained under the abovementioned conditions and intermediate products are listed. Generally speaking, the sulfurization temperature is higher for heavy Ln_2S_3 than that of light Ln_2S_3. For light rare earths, whether particle size of Ln_2O_3 is small (1.8 μm of La_2O_3) or large (16 μm of Nd_2O_3), single Ln_2S_3 phase can be prepared. Nevertheless, the products from heavy Ln_2O_3 contain oxysulfide residues when particle size of heavy Ln_2O_3 is large (5 μm of Yb_2O_3 and 6.5 μm of Lu_2O_3). Therefore, heavy Ln_2O_3 are comparatively difficult to be sulfurized than light Ln_2O_3.

In this study, sulfurization temperature of heavy Yb_2O_3 was lessened to 600 °C for η-Yb_2S_3 and 1000 °C for ε-Yb_2S_3 by varying the characters of starting material Yb_2O_3. This discovery is not only for preparation of single Yb_2S_3 but also for fabrication of all Ln_2S_3 at lower temperature with small particle size and large specific surface area of Ln_2O_3 as starting material.

Table 2.5 Particle size of starting material and minimum sulfurization temperature required for single Ln_2S_3 phase (sulfurization time: 8 hr)

Starting material	Particle size/μm	Sulfurization					
		Temp. /°C	Final Products	Intermediate Products	Oxygen /mass%	Carbon /mass%	Reference
La_2O_3	1.8	750	β-La_2S_3	La_2O_2S,	0.91	0.02	Ref. 8
CeO_2	4.3	700	α-Ce_2S_3	Ce_2O_2S, CeS_2	1.30	0.10	Ref. 9
Pr_6O_{11}	7.5	850	β-Pr_2S_3	Pr_2O_2S, α-Pr_2S_3,	0.45	0.06	Ref. 10
Nd_2O_3	16	1000	β-Nd_2S_3	Nd_2O_2S, α-Nd_2S_3,	0.25	0.32	Ref. 10
Sm_2O_3	9.8	850	α-Sm_2S_3	Sm_2O_2S,	0.52	0.03	Ref. 8
Eu_2O_3	3.5	800	EuS	EuS_2, Eu_3S_4	0.52	0.05	–
Gd_2O_3	1.0	975	α-Gd_2S_3	Gd_2O_2S, GdS_2	0.25	0.43	Ref. 11
Tb_4O_7	3.0	1050	α-Tb_2S_3	Tb_2O_2S	0.41	0.14	Ref. 11
Dy_2O_3	1.0	975	α-Dy_2S_3	Dy_2O_2S	–	–	–
Ho_2O_3	1.6	1050	δ-Ho_2S_3	Ho_2O_2S	0.52	0.78	Ref. 12
Yb_2O_3	0.4	1000	ε-Yb_2S_3	Yb_2O_2S, η-Yb_2S_3	0.62 (1050°C)	0.86 (1050°C)	–
	1.0	700	η-Yb_2S_3	–	–	–	
		1000	ε-Yb_2S_3	η-Yb_2S_3	–	–	
	5	1050	ε-Yb_2S_3, Yb_2O_2S	Yb_2O_2S	–	–	
Lu_2O_3	6.5	1050	ε-Lu_2S_3, Lu_2O_2S	Lu_2O_2S	–	–	–

α: Orthorhombic (Gd_2S_3 type), β: Tetragonal ($Pr_{10}S_{14}O$ type), γ: Cubic (Th_3P_4 type)
δ: Monoclinic (Er_2S_3 type), η: Orthorhombic (Sc_2S_3 type), ε: Hexagonal

2.4 Heat treatment and sintering of ytterbium sulfides

In this section, the formation behavior of Yb_2S_3 synthesized via CS_2 gas sulfurization of Yb_2O_3 was investigated. Dependences of temperature on formation of Yb_2S_3 were systematically researched. Influences of specific surface area and particle size of Yb_2O_3 on the sulfurization process were discussed. Furthermore, it is meaningful to prepare Yb_3S_4 or YbS by heat treatment of Yb_2S_3 under different atmospheres.

2.4.1 Heat treatment of Yb_2S_3 under Ar or Ar/CS_2 gas

The synthetic Yb_2S_3 powders were heat treated under different conditions to synthesize Yb_3S_4 phase. XRD patterns of the synthetic from treated Yb_2S_3 powders are shown in Fig. 12. In Fig. 12, each of the Yb_2S_3 powders underwent orthorhombic-to-hexagonal phase transition upon heat treatment at 1000 °C for 3 hr in

Ar/CS_2 atmosphere. However, XRD results showed that orthorhombic Yb_3S_4 was main phase after heat treatment at 1050°C for 8 hr under Ar atmosphere and Yb_2S_3 nearly disappeared upon prolonged (12 hr) heat treatment.

Table 2.6 shows chemical compositions of synthetics by treated Yb_2S_3 powders under Ar gas for 5 ~ 12 hr. There is phase transformation of synthetic η-Yb_2S_3 powders with orthorhombic structure to hexagonal structure at 1000°C for 5 hr or 6 hr. Compared with starting material Yb_2O_3-A, the composition of synthetic ε-Yb_2S_3 by heat treatment is more approximate to theory value of Yb_2S_3 (Yb theory content 78.28%, S theory content 21.72%). And then, the impurity content is least for raw material Yb_2O_3-C. For longer heat-treatment time (6 hr), the product ε-Yb_2S_3 has no change but the content of sulfur is lower than that of sample treated 5 hr, which imply the mechanism of phase change is possibly sulfur lost during heat-treatment. If the treatment temperature is added to 1050 °C or time is lengthened to 8 hr or 12 hr, Yb_3S_4 is able to obtain. However, it is also connected with sulfurization procedure and impurity contents. In the other words, the residual carbon content will influence the stability of Yb_2S_3. Although the phase transformation from ε-Yb_2S_3 to Yb_3S_4 can be completed at 1050 °C for 12 hr, the composition of synthetic Yb_3S_4 has some differences with their theory values.

Table 2.6 Chemical composition of synthetics by treated Yb_2S_3 powders under Ar gas for 5 ~ 12 hr

Raw	Sulfurization		Heat-treat		Product	Composition (%)		
Yb_2O_3	°C	hr	°C	ks		Yb	S	Impurity
Yb_2O_3-A	800	3	1000	5	ε-Yb_2S_3	78.62	20.9	0.45
Yb_2O_3-B	800	3	1000	5	ε-Yb_2S_3	78.1	21.7	0.19
Yb_2O_3-C	800	3	1000	5	ε-Yb_2S_3	78.2	21.7	0.09
Yb_2O_3-B	800	4	1000	6	ε-Yb_2S_3	78.8	20.5	0.7
Yb_2O_3-B	930	4	1050	8	Yb_3S_4	79.1	19.5	1.3
Yb_2O_3-B	800	4	1050	12	Yb_3S_4	78.6	19.4	2.0
Yb_2O_3-C	800	4	1050	12	Yb_3S_4	78.0	19.2	2.7
Yb_2O_3-B	1050	8	1050	12	Yb_3S_4	79.1	19.5	1.44

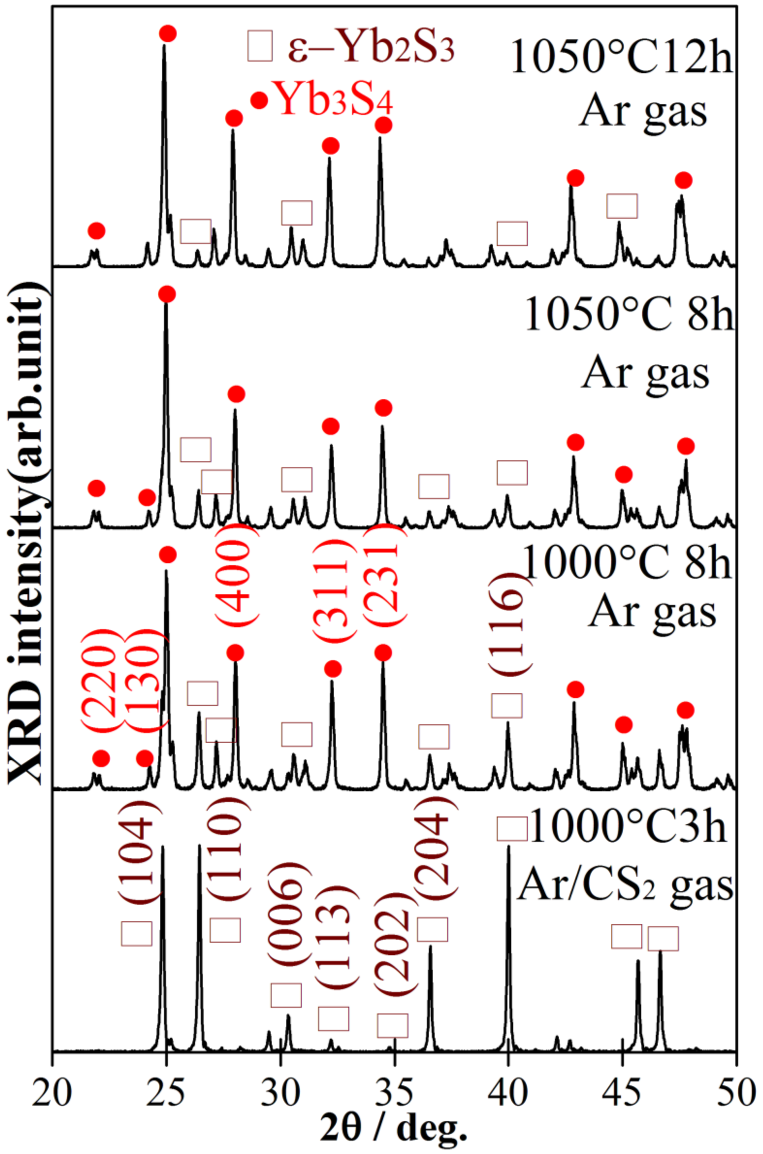

Fig. 2.12 XRD patterns of heat-treatment products under normal pressure

2.4.2 Heat treatment of Yb_2S_3 under vacuum

Figure 2.13 showed representative XRD patterns for the reaction products annealed synthetic Yb_2S_3 powders at 1000 °C ~ 1500 °C for 1 hr ~ 5 hr. Under the annealing temperature of 1000°C, hexagonal ε-Yb_2S_3 has no variation for 1 hr. Following time increased to 3 hr, hexagonal ε-Yb_2S_3 has completely transformed to Yb_3S_4. At 1200 °C, diffraction peaks of YbS were observed for 5 hr. The intensity of diffraction peaks of Yb_3S_4 reduced following annealing temperature increased to 1500 °C. Single YbS having a homogeneity range $YbS_{1.11\text{-}1.15}$ was formed at 1500 °C for 3 hr.

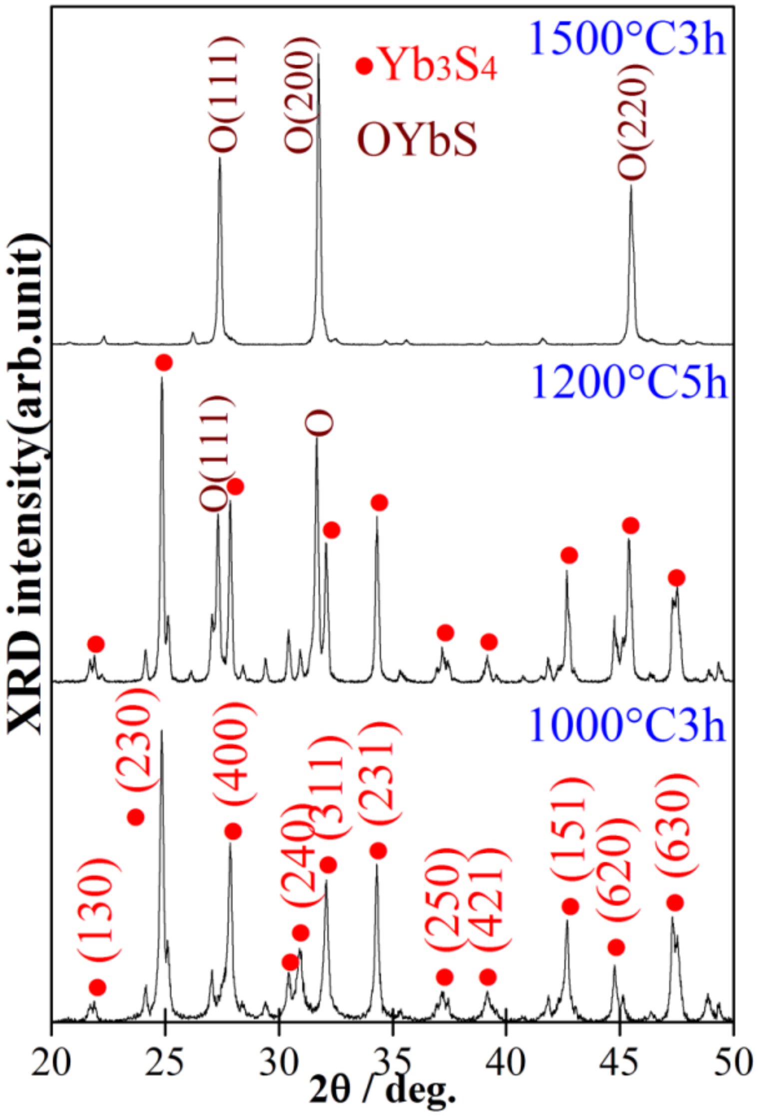

Fig. 2.13 XRD patterns of heat-treatment products under vacuum

XRD patterns for the reaction products sintered at 1000 ~ 1400 °C by SPS are shown in Fig. 2.14. At 1000 °C and 1100 °C, the diffraction peaks of hexagonal ε-Yb_2S_3 had no change. As the sintering temperature enlarged to about 1300 °C, the slight diffraction peaks of orthorhombic Yb_3S_4 were observed. It displays that hexagonal ε-Yb_2S_3 transform to Yb_3S_4 on the surface of compact at high sintering temperature. However, this transformation of Yb_2S_3 to Yb_3S_4 was inhabited under closed carbon mold.

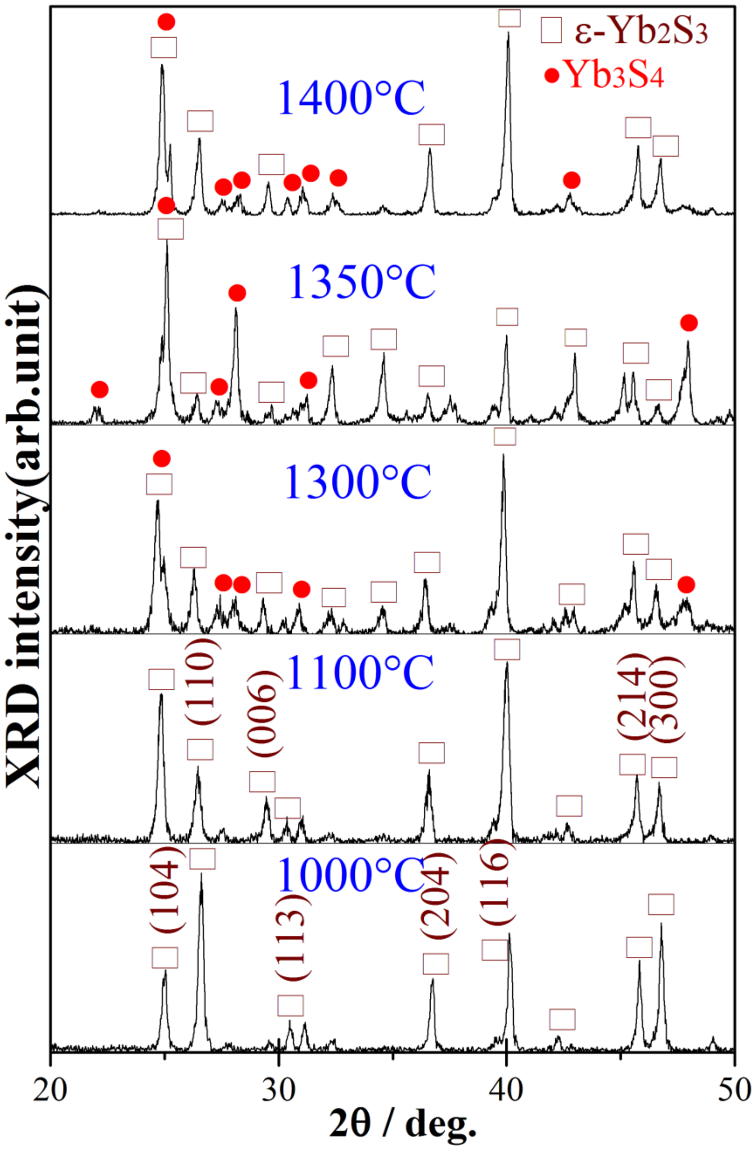

Fig. 2.14 XRD patterns of heat-treatment products by SPS

Base on the above-mentioned annealing results, ytterbium monosulfide can be formed by annealing the sesquisulfide at high temperature. Ytterbium are easier to be reduced to the divalent state than the others lanthanide element due to their full 4f shell electronic structures.

2.5 Sintering and Heat capacity of Yb_3S_4 and YbS

Figure 2.15 showed XRD patterns of Yb_3S_4 and YbS compacts sintered from the annealed Yb_3S_4 and YbS powder at 1550 °C for 1 or 3 hr and 1600 °C for 0.33 hr, respectively. XRD results suggested that Yb_3S_4 was stable at about 1550 °C. Yb_3S_4 is difficult to transform and decompose to YbS during SPS sintering. YbS bulk was easy to be broken during sintering process due to its NaCl structure.

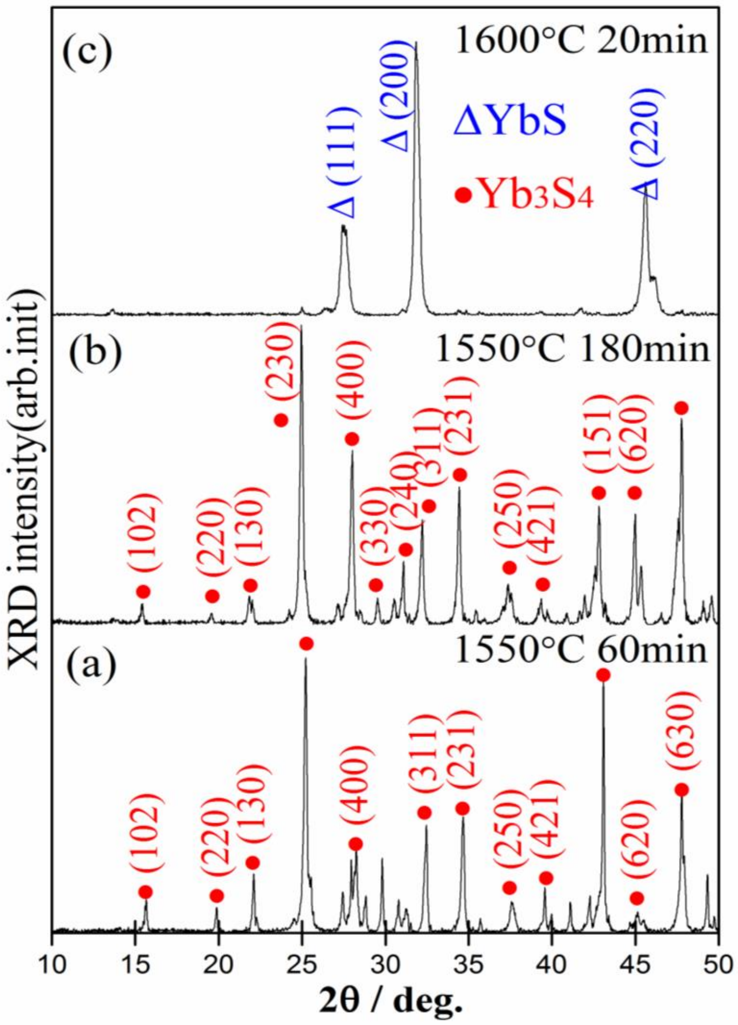

Fig. 2.15 XRD patterns of Yb_3S_4 and YbS compacts sintered from the annealed Yb_3S_4 and YbS powder

Figure 2.16 shows SEM micrographs analysis of sintered Yb_3S_4 and YbS compacts from the annealed Yb_3S_4 and YbS powder. In Fig. 2.17, there are local microcracks in synthetic Yb_3S_4, which is the reason for the sample broken. On the other hand, both Yb_3S_4 and YbS compacts have some poles, which may be caused by the high temperature sulfur loss.

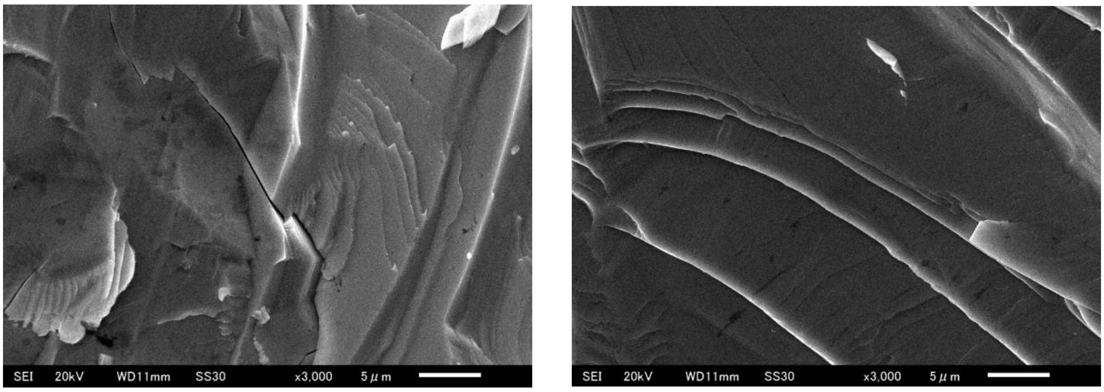

Fig. 2.16 SEM micrographs of Yb_3S_4 and YbS compacts sintered from the annealed Yb_3S_4 at 1500 °C for 5h and YbS powder at 1600 °C for 0.33 hr

Figure 2.17 shows the temperature dependence of specific heats for Yb_3S_4 and YbS compacts sintered from the annealed Yb_3S_4 at 1500 °C for 5h and YbS powder at 1600 °C for 0.33 hr. A broad peak appears at about 4 K for Yb_3S_4 with a peak value of 5.1 $J/K\cdot mol^{-1}$, which is smaller than that former research result of Yb_3S_4 (5.5 $J/K\cdot mol^{-1}$ at 4.3 K). Moreover, the peak value per Yb^{3+} is evaluated as 1.46 J/K Yb^{3+}, which included the contributions of the crystal field and phonon. This value seems to be smaller than that of calculated with the S=1/2 impurity Kondo model. And then, there is no peak for antiferromagnetic YbS.

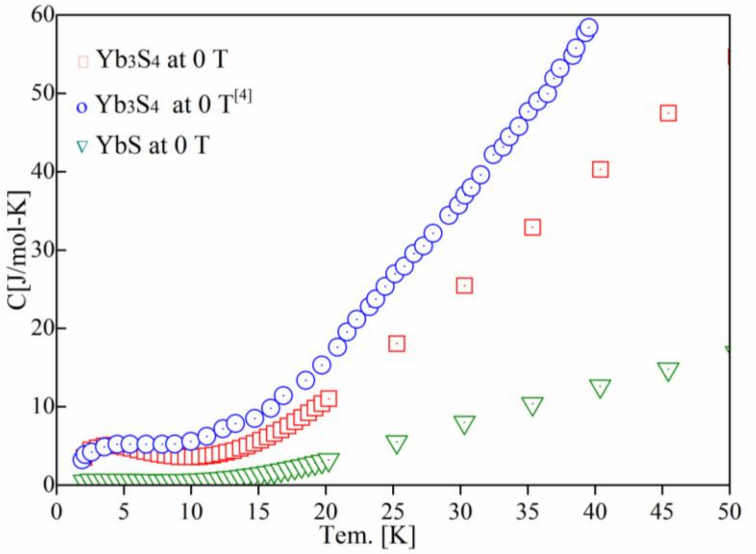

Fig. 2.17 heat capacity of Yb_3S_4 and YbS compacts sintered from the annealed Yb_3S_4 at 1500 °C for 5h and YbS powder at 1600 °C for 0.33 hr

2.6 Conclusions

In the synthesis of ytterbium sulfides, a new polymorphic form of Yb_2S_3 with an orthorhombic structure has been observed and obtained at 600 ~ 850 °C, single-phase ε-Yb_2S_3 was prepared above 1000 °C for 8 hr. In the annealing of synthetic ε-Yb_2S_3, Yb_3S_4 and YbS could be formed by decomposed Yb_2S_3 at high temperature. On the other hand, bigger specific surface area can reduce the sulfurization temperature and accelerate the sulfurization reaction. The impurity contents of oxygen and carbon in synthetic powders and the particle size of synthetic powders were dependent on the sulfurization conditions, especially the CS_2 gas flow rate.

Yb_2O_3 powders with different characters were employed to research the influence of particle size and specific surface area on the synthesis of Yb_2S_3. The main conclusions are as follows: (1) High sulfurization temperature (1000 °C) and small particle size are necessary for preparation of single hexagonal ε-Yb_2S_3. Larger specific surface area (50 m^2/g) of Yb_2O_3 is better for fabrication of orthorhombic η-Yb_2S_3 at low temperature of 600 °C for 8 hr. However, single Yb_2S_3 cannot be obtained if specific surface area of Yb_2O_3 is less than 2 m^2/g and particle size is larger than 5 μm. (2) Sulfurization time (0.5 hr) tends to decrease with increasing temperature (1050 °C). CS_2 gas flow rate does not only influence the sulfurization efficiency and products, but also control the impurity content. Particle sizes of synthetic orthorhombic η-Yb_2S_3 and hexagonal ε-Yb_2S_3 are dependent on sulfurization condition and impurity content. (3) Heavy Ln_2O_3 are comparatively difficult to be sulfurized than light Ln_2O_3. To modify characters of Ln_2O_3 is an effective step for preparation of Ln_2S_3.

Hexagonal ε-Yb_2S_3 was synthesized at above 1000°C by sulfurizing its oxide with CS_2 gas. The synthetic Yb_2S_3 is more stable in sulfur-rich atmosphere than argon gas or vacuum at about 1000°C. Yb_2S_3 phase transformed to Yb_3S_4 phase (1000 °C for 3 hr or 1200 °C for 1 hr) or YbS phase (1500 °C for 3 hr) during annealing. Yb_2S_3 had better phase stability below 1400 °C with spark plasma sintering. The phase stability of Yb_2S_3 probably depended on the sulfur vapor pressure. Yb_3S_4 and YbS were sintered by spark plasmas sintering at 1500 °C for 5 hr and 1600 °C for 0.33 hr, respectively. The heat capacity of synthetic Yb_3S_4 and YbS was measured at 2- 50 K and compared with previous reported.

Chapter 3 Preparation, sintering and large magnetocaloric effect of europium sulfides

3.1 Introduction

Europium is one of the unusual rare earth elements, because in solids it occurs in different valence states: it can be either divalent, trivalent or of mixed valency[94]. Bivalent europium (with 7 electrons in the 4f orbital) and trivalent europium (having 6 electrons in the 4f orbital) are the two main oxidation states of europium. The valence of europium is strongly dependent on temperature and valence change can cause phase transformation of Eu_3S_4-to-EuS.

There are three main europium sulfide species, i.e., EuS, Eu_3S_4, and EuS_2 [95]. Recently, there has been important attention in EuS nanoparticles as prospective optomagnetic and luminescent materials because the crystal size of these particles affects the optomagnetic and luminescent properties [96]. EuS has received considerable attention because of its unique photophysical and magnetooptical properties [97] and exhibits spin-filtering effects with potential application in spintronics [98]. EuS is an important starting material for the Eu-Cu-S system [99], the Eu-R-S system (R = La, Ce, Pr, Nd, and Gd) [100], and the Eu-Pb-S system [101, 102]. Partial Eu-substitution of the fluorescent sulfide material $BaAl_2S_4$ synthesized from the mixture of Al_2S_3, BaS, and EuS, is anticipated to be applicable for development of an inorganic electroluminescence (EL) display [97].

Single crystal EuS has a large magnetocaloric effect ($37\ J\cdot Kg^{-1}\cdot K^{-1}$) at 18.5 K near the liquid hydrogen temperature of 20 K [103]. For storage and transportation of hydrogen fuel, it is effective to liquefy hydrogen; therefore, a regenerating agent with a large magnetocaloric effect near the liquid hydrogen temperature is required [104].

Mixed valence Eu_3S_4 with the formula of $(Eu^{2+})(Eu^{3+})_2S_4$ is sensitive to temperature. Eu_3S_4 crystals can act as sites for nucleation to accelerate the formation of γ-La_2S_3 during the nucleation process, which is advantageous for the preparation and stabilization of γ-La_2S_3 at low-temperature[9]. $EuLn_2S_4$ (Ln = La-Gd) with Th_3P_4 structure is a rare p-type semiconductor with a relatively large Seebeck coefficient of $350\ \mu V\cdot K^{-1}$ at around 340 K[100].

Traditionally, EuS powders are generally prepared from the constituents [95] or by CS_2-gas [105] or H_2S-gas sulfurization [106] of Eu_2O_3. H_2S-gas sulfurization process of Eu_2O_3 conducted over several days and high sulfurization temperature (1523 K) is necessary for the minimum oxygen concentration in the synthetic EuS [106]. Compared with H_2S sulfurization, CS_2 gas is a more effective sulfurization agent, which have been proven during the preparation of binary rare-earth sesquisulfides from their oxides [6]. These sesquisulfides can be obtained at a lower temperature by CS_2-gas sulfurization than that of H_2S-gas sulfurization, as is evident from the change in the standard free energy of formation of sulfurization.

The most common method for the synthesis of EuS nanoparticle is thermal decomposition of dithiocarbamate complexes in coordinating solvents [107]. EuS nanocrystals with narrow size distribution are synthesized in high yields by the thermal decomposition of $Eu(oleate)_3$ in oleylamine using CS_2 as the sulfur source[108]. To overcome the problem of yield and purity for thermal decomposition method, Eu_2O_3 nanowires were employed to synthesize EuS via H_2S-gas sulfurization [109, 110]. However, there is no report about CS_2-gas sulfurization of nanoscale Eu_2O_3 with different shapes for the preparation of EuS.

In the Chapter 2, the formation of sesquisulfide was found to be dependent on the particle size and specific surface area of Yb_2O_3 used as the starting material[111]. In general, the sulfurization of Yb_2O_3 results in the formation of hexagonal Yb_2S_3 through Yb_2O_2S. When Yb_2O_3 with a particle size below 1 μm and a specific surface area of 50 m^2/g was employed, a new polymorphic Yb_2S_3 phase with an orthorhombic structure was obtained at 873 K [111]. Europium is similar with ytterbium on the stable divalenve and half-filled 4f electric structure, so it is meaningful to study the influences of particle size and SSA of Eu_2O_3 on sulfurization process.

In this chapter, the formation of europium sulfides, especially Eu_3S_4 and EuS, is investigated via CS_2-gas sulfurization of three kinds of nanoscale Eu_2O_3 powders with different characteristics. The dependence of the sulfurization products on the conditions and the initially synthesized powder is systematically evaluated. Morphology and SSA of synthetics were characterized by high resolution scanning electron microscopy (SEM) and the Multi-point Brunauer, Emmett and Teller (BET) method. Sulfurization reaction processes were analyzed with thermodynamic calculation.

We also examine the optimal heat-treatment conditions for synthetic EuS based on X-ray diffraction analysis by subjecting the obtained europium sulfides to heat treatment in different atmospheres. Polycrystalline materials that can be manufactured into plate, sphere or both are necessary for practical use of magnetic materials in magnetic refrigerator. Moreover, MCE of polycrystalline EuS is required to have similar value to that of a single crystal. Magnetocaloric effect of EuS sintered at 1000 °C and 1600 °C from two kinds of Eu_2O_3 was investigated.

3.2 Experimental procedure

Herein, Eu_2O_3 powders (SSA of 9.33 m^2/g, purity of 99.99% mass fraction, average particle size ~100 nm, Shin-Etsu Chemical Co., Ltd., remarked as Eu_2O_3-A; SSA of 8.47 m^2/g, purity of 99.9% mass fraction, mean particle size ~130 nm, Anan Kasei Co., Ltd. remarked as Eu_2O_3-B; particle distribution of nanowire Eu_2O_3 ~ 2.5 μm*50 nm, remarked as Eu_2O_3-C) were examined as listed in Table 3.1. The CS_2 gas sulfurization process was described in our previous report [111]. The sulfurization condition is from 300 °C to 1050 °C for 0.5-8 hr with gas flowing rate (denoted as GFR) of 50-100 mL/min.

X-ray diffraction (XRD, Model Rint-Ultima+, Rigaku Corp., Tokyo, Japan) with monochromatic Cu-Kα radiation at 40 kV and 20 mA was used to identify the synthesized products. The lattice parameters of the products were also calculated from the data acquired with a scan step of 1.0×10^{-3} degree for 2 s. The reaction degree was estimated from the relative intensities of the diffraction lines of each synthesized product. The oxygen and carbon content of the synthesized products were determined by oxygen analyzer (Model TC-436, Leco Corp., St. Joseph, MI) and carbon analyzer (Model CS-444LS, Leco Corp., St. Joseph, MI), respectively. The actual stoichiometry of the obtained products was estimated by oxidizing them to stoichiometric Eu_2O_3 at 1000 °C. The sulfur content was calculated from the weight of Eu_2O_3 and the mass change caused by the complete oxidation of the sulfide to the oxide.

The morphology of synthesized powders was characterized by SEM (JSM-5310LV, JEOL Ltd., Tokyo, Japan). The SSA of the synthetic products was measured by using a surface area and pore size analyzer (Autosorb-1, Quantachrome Instruments, Florida, USA) with N_2 adsorption. The isothermal magnetization curves for sintered EuS compact were measured at 10 -30 K with a Quantum Design SQUID magnetometer to check the magnetocaloric effect of polycrystalline EuS.

Heat treatment of the synthesized Eu_3S_4 powders was performed under different conditions as follows: 1) Eu_3S_4 powder was held at 673–1073 K for 1 hr under Ar/CS_2 or Ar gas. 2) Eu_3S_4 powder was placed on a BN boat (inner diameter: 15 mm) and held at 773–1773 K for 1 hr under vacuum at less than 1.4×10^{-3} Pa.

Table 3.1 Information of Eu_2O_3 powders with different characteristic

Raw material	SSA(m^2/g)	Grain size	Purity (%)	Producer
Eu_2O_3-A	9.33	~100 nm	99.99	Shin-Etsu Chemical Co., Ltd.,
Eu_2O_3-B	8.47	~130 nm	99.9	Anan Kasei Co., Ltd.
Eu_2O_3-C	9.99	~ 2.5 μm*50 nm	–	Preparation in our lab

3.3 Influence of Eu_2O_3 character and sulfurization conditions on the preparation of EuS

3.3.1 Preparation of Eu_3S_4 and EuS by CS_2-gas sulfurization of Eu_2O_3

Figure 3.1 shows TEM images of the Eu_2O_3 powder employed in this study. Eu_2O_3-A nanospheres have a uniform size of ~100 nm and SSA is 9.33 m^2/g (Fig. 3.1a). Compared with Eu_2O_3-A, homogeneous oval Eu_2O_3-B has bigger particle size (~ 130 nm) (Fig. 3.1b) and smaller SSA (8.47 m^2/g). Because these Eu_2O_3-A and Eu_2O_3-B powders consist of fine particles and possess large SSA, chemical reactivity of this Eu_2O_3 powder is expected to be extremely high. Eu_2O_3-C powders are prepared from $Eu(NO_3)\cdot 6H_2O$ and $(NH_4)_2CO_3$ by the coprecipitation method. The precipitate was calcined at 800 °C for 1 hr. The particle size of Eu_2O_3-C with needle-like shape is ~ 2.5 µm*50 nm (top right of Fig. 3.1c). The Eu_2O_3-C plate is easier to break due to the existence of some stoma (center of Fig. 3.1c).

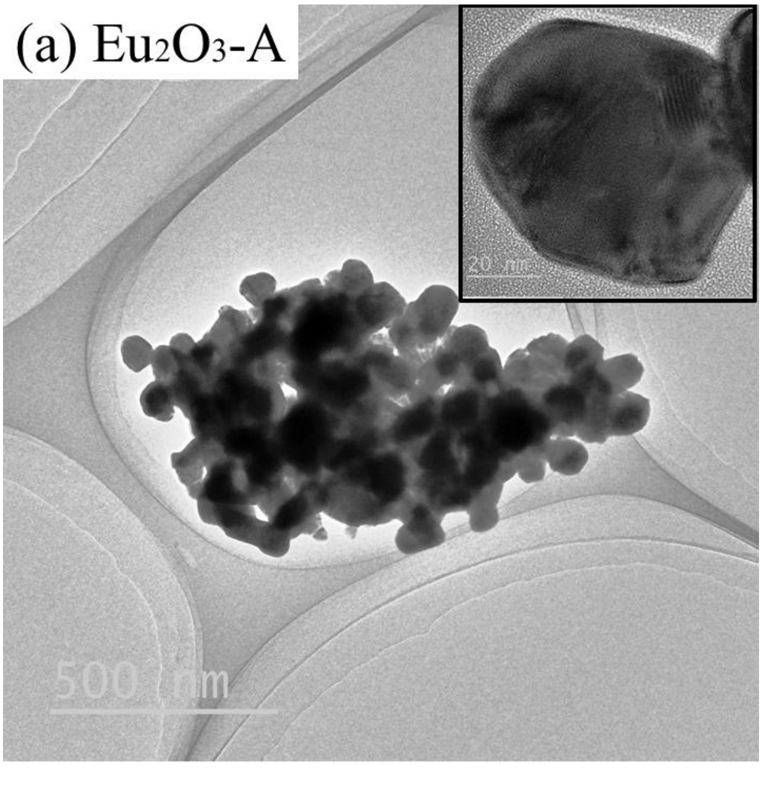

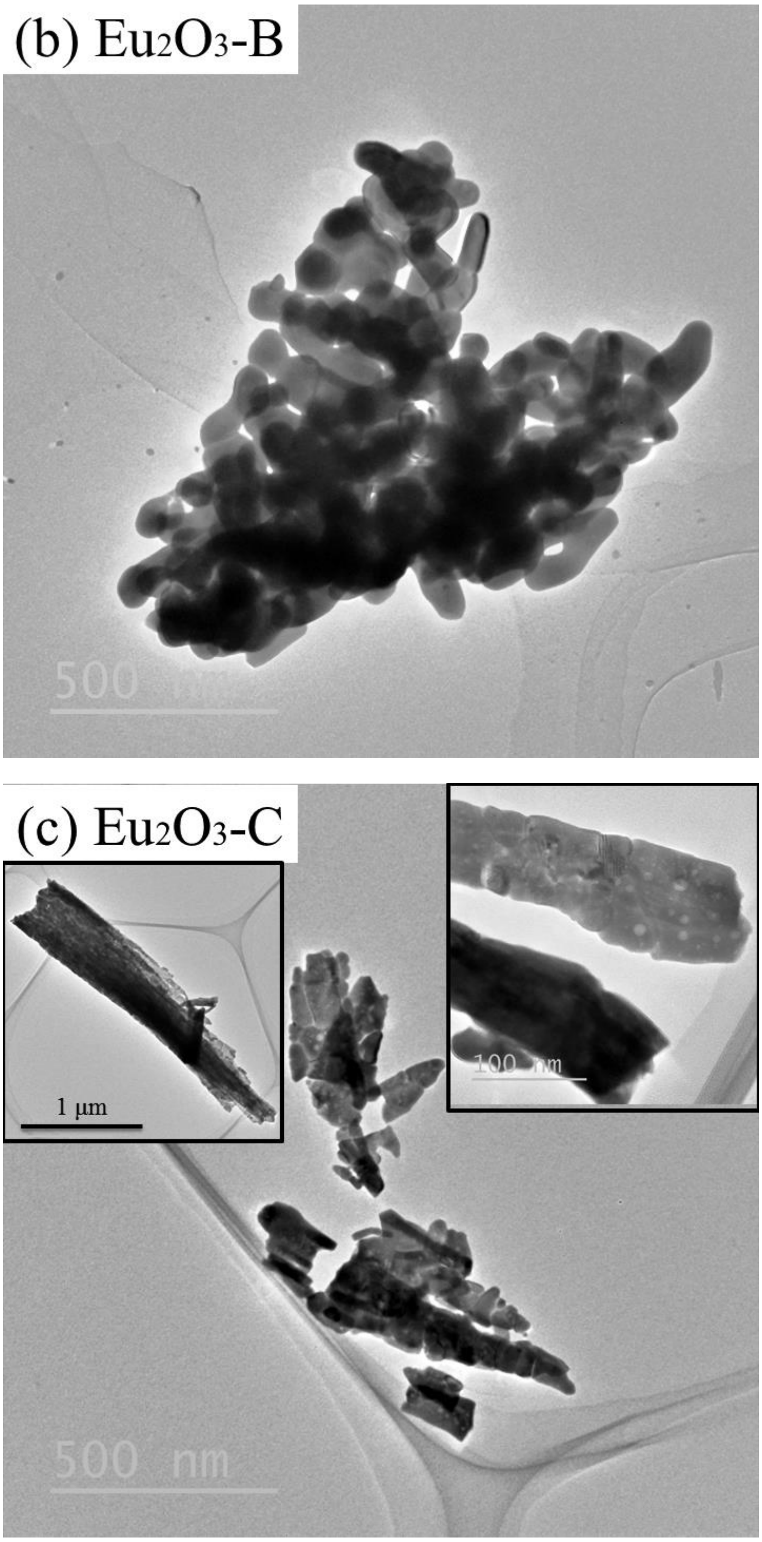

Figure 3.1 TEM images of the Eu_2O_3 powder

Figure 3.2 shows representative XRD patterns of synthetics with sulfurization at 500 ~1050 °C for 0.5 ~ 8 hr and GFR of 1.67 mL/s. In Fig. 3.2a, single phase Eu_3S_4 formed by the sulfurization of Eu_2O_3-A at 500°C for 8 hr. Single Eu_3S_4 can be gained from Eu_2O_3-A only at 500 °C for longer than 0.5 hr. The intensities of EuS characteristic peaks strengthened while those of Eu_3S_4 weakened following with sulfurization temperature increasing from 600 °C to 800 °C. Single phase EuS can be obtained at 800 °C for 3 hr or above 900 °C for 0.5 hr.

For the sulfurization of Eu_2O_3-B, it is impossible to prepared single phase Eu_3S_4 at 500 °C for 0.5 - 8 hr. Different with the sulfurization of Eu_2O_3-A, weak characteristic peaks of residual Eu_2O_3 always existed. The transformation of Eu_3S_4-to-EuS started from 600 °C, which is similar with that of Eu_2O_3-A. However, the transformation process cannot complete due to the residual Eu_2O_2S. Single phase EuS cannot be sulfurized at 800 °C even for 8 hr with different CS_2-gas flow rate (0.83 mL/s - 1.67 mL/s). EuS can be prepared at 900 °C for 2 hr or above 1000 °C for 0.5 hr.

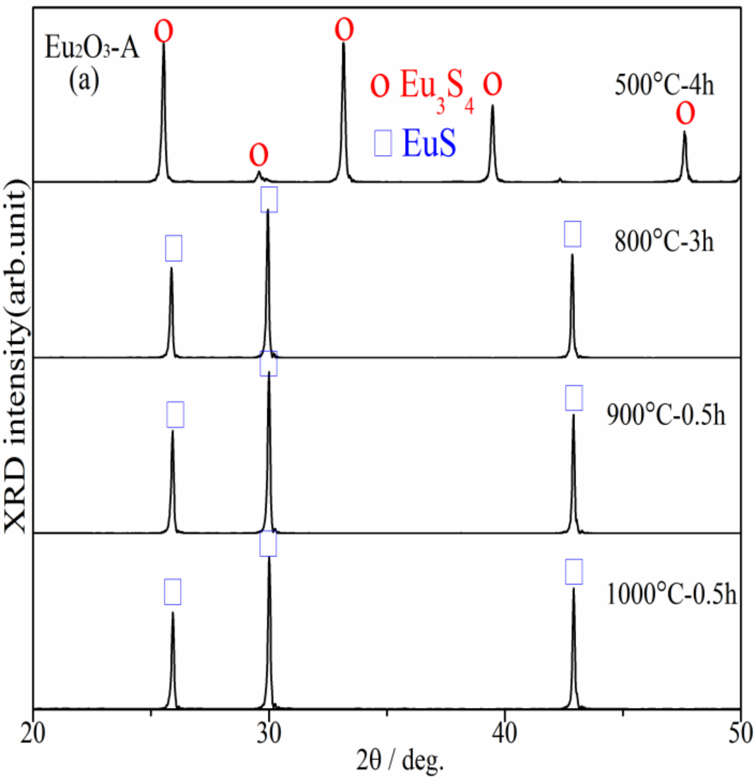

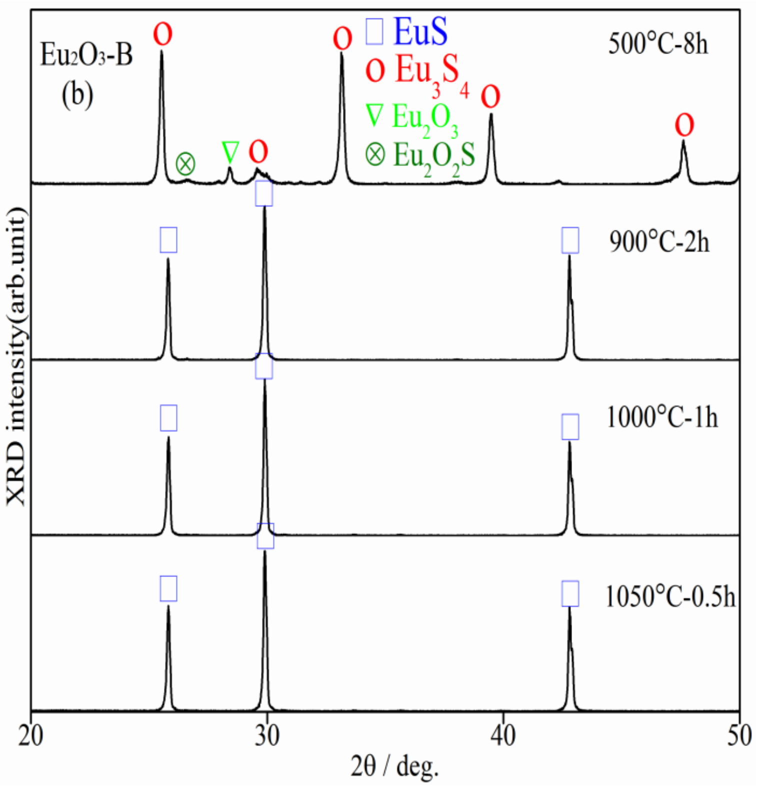

Figure 3.2 XRD patterns of synthetics with sulfurization at 500 ~1050 °C for 0.5 ~ 8 hr and GFR of 1.67 mL/s

Figure 3.3 shows typical XRD patterns of the products prepared by CS_2 sulfurization of Eu_2O_3-A powder at 673-1073 K for 0.5-8 hr. The sulfurization reaction started at 673 K and diffraction peaks of Eu_3S_4 and EuS_2 were detected (Fig. 2a). Eu_3S_4, as a single product, was obtained via sulfurization at 773 K for 4 hr (Fig. 2b, JCPDS standard card PDF 01-074-7272). Ananth et al. [95] attempted to synthesize Eu_3S_4 from a 3:4 mixture of Eu and S powder using a direct reaction method in a sealed tube. That reaction yielded an unknown product at 773 K [95]. In the present study, all the peaks were identified. When the sulfurization temperature was increased to 873 K, weak diffraction peaks of EuS and Eu_2O_2S were observed, but the main phase was Eu_3S_4 (Fig. 2c). Single-phase EuS was obtained via sulfurization at temperatures above 1073 K for 8 hr (Fig. 2d, JCPDS standard card PDF03-065-5080). Reduction of europium to the divalent state would increase the number of 4f electrons to seven, which is a half-filled level and thus a stable state.

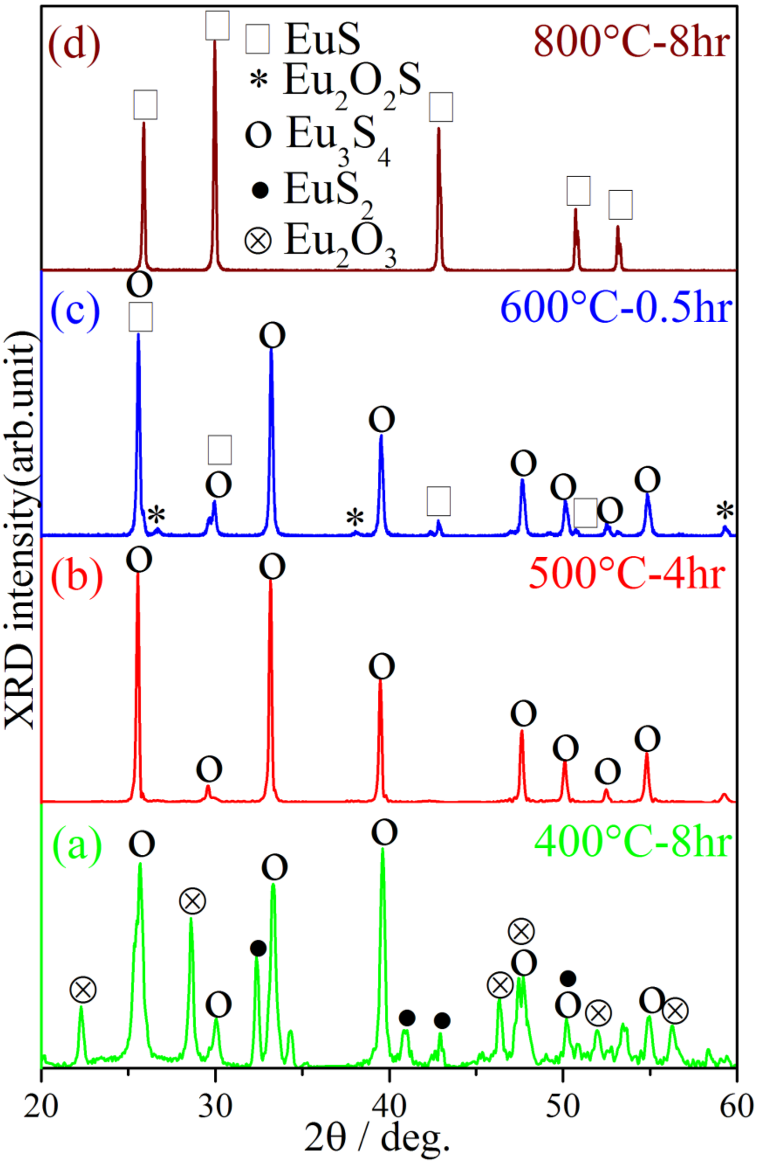

Figure 3.3 XRD patterns of the products prepared by CS_2 sulfurization of Eu_2O_3-A powder at 673-1073 K for 0.5-8 hr.

Figure 3.4 shows the dependence of the lattice parameters of Eu_3S_4 (on the break) and EuS (below the break) on the sulfurization conditions. It is reported that the lattice parameters of cubic Eu_3S_4 and EuS are 8.534 Å (PDF card 01-074-7272) and 5.97 Å [109], respectively. In the sulfurization temperature range where Eu_3S_4 was detected, as shown in Figure 3.4, the lattice constant of Eu_3S_4 tended to decrease as the sulfurization temperature and time decreased. In the low sulfurization temperature range where Eu_3S_4 presented, the lattice constant of EuS did not depend on the sulfurization time and remained constant at 5.97 Å. In the high sulfurization temperature range, the lattice constant of EuS gradually decreased as the sulfurization temperature increased in the case of a short sulfurization time. In the high sulfurization temperature range where single-phase EuS was obtained, the lattice constant was smaller in the case of a long sulfurization time than in the case of a short sulfurization time.

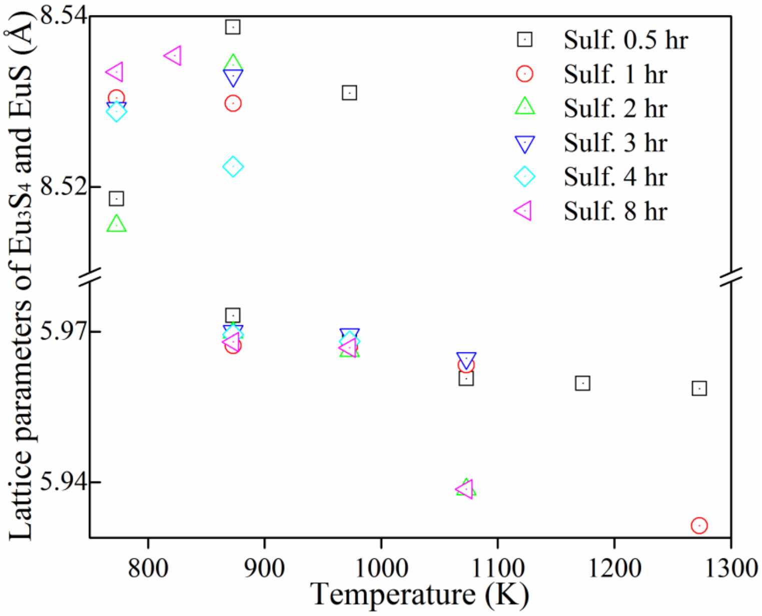

Figure 3.4 Lattice parameters of Eu_3S_4 and EuS

Table 3.2 shows chemical composition of synthetic EuS from sulfurization of Eu_2O_3. For a low sulfurization temperature, impurity oxygen remained in the Eu_3S_4 powder. The content of impurity oxygen declined from 0.89% in the Eu_3S_4 powder (sulfurized at 500 °C for 8 hr) to 0.11% in the EuS powder (sulfurized at 1000 °C for 8 hr). On the other hand, the amount of impurity carbon increased from 0.05% (sulfurized at 800 °C for 8 hr) to 0.26% (sulfurized at 1000 °C for 8 hr) in the EuS powder due to the decomposition of CS_2 gas. Based on the mole ratio of Eu to S in the EuS powder, S deficiency was observed for the short sulfurization time of 0.5 hr at 900 °C. For longer sulfurization time of 8 hr and higher sulfurization temperature, S was enriched, i.e., Eu was deficient. It is deduced that EuS possesses a solid solution range and the Eu deficiency was more clearly observed.

Table 3.2 Chemical composition of synthetics by sulfurized Eu_2O_3-A

Product	Temp.	Time	Mass(O)	Mass (C)	Mass(Eu)	Mass (S)	Mole Eu/S
Eu_3S_4	500 °C	8 hr	0.89%	0.12%	77.9%	21.0%	0.7825
EuS	800 °C	3 hr	--	--	81.18%	17.09%	0.9980

EuS	800 °C	8 hr	0.52%	0.05%	82.5%	17.7%	1.0171
EuS	900 °C	0.5 hr	--	--	82.02%	17.27%	0.9982
EuS	1000 °C	0.5 hr	--	--	82.25%	17.32%	0.9983
EuS	1000 °C	8 hr	0.11%	0.26%	82.4%	18%	1.0356

3.3.2 Influence of sulfurization conditions on the formation of EuS

The temperature dependences of diffraction intensity of EuS (200), Eu_2O_2S (100), Eu_3S_4 (211), EuS_2 (220) and Eu_2O_3 (222) formed via CS_2 sulfurization of Eu_2O_3-A at 500 °C - 1050 °C for 0.5, 1, and 8 hr with gas flow rate of 1.67 mL/s are shown in Fig. 3.5a. At a sulfurization temperature of 400 °C, EuS_2 was formed as an intermediate product. Shafer [106] reported that EuS_2 was not formed during H_2S-gas sulfurization of Eu_2O_3. The maximum diffraction intensity of EuS_2 was detected at 400 °C and disappeared at 500 °C. Diffraction intensity of Eu_3S_4 increased gradually from 400 °C to 500 °C and decreased from 600 °C and finally disappeared at 800 °C. Single phase Eu_3S_4 was obtained at 500 - 550 °C, which is lower than the temperature at which this single phase was obtained during H_2S sulfurization, i.e., above 650 °C [106]. Hexagonal Eu_2O_2S appeared at 600 - 800 °C for short reaction time of 0.5 hr or 1 hr. For longer sulfurization time of 8 hr, Eu_2O_2S disappeared at 600 °C. Intensity of diffraction peak of Eu_3S_4 lessened while that of EuS enlarged at 600 - 800 °C. Single EuS phase was finally formed at 800 °C for 8 hr.

With an increase in the sulfurization temperature, Eu_2O_2S was detected with low intensity in the temperature range of phase transformation from Eu_3S_4 to EuS, where Eu_3S_4 and EuS coexistent. The temperature range of this phase transformation became narrow as the sulfurization time increased. For a longer sulfurization time of 8 hr, low intensity Eu_2O_2S peaks were observed at only 600 °C.

Figure 3.5b shows temperature dependences of diffraction intensity of EuS (200), Eu_2O_2S (100), Eu_3S_4 (211), EuS_2 (220) and Eu_2O_3 (222) formed via the sulfurization of Eu_2O_3-B at 500 °C - 1050 °C for 0.5 hr and 8 hr with GFR of 1.67 mL/s. Different with the sulfurization of Eu_2O_3-A, peaks of Eu_2O_3-B did not fade until to 700 °C for 0.5 hr and 600 °C for 8 hr, respectively. Eu_3S_4 appeared at 500 - 700 °C for short sulfurization of 0.5 hr. However, the decomposition of Eu_3S_4 finished at 600 °C for 8 hr. Single phase EuS can be synthesized by the sulfurization of Eu_2O_3-B at 1000 -

1050 °C for 0.5 hr or 900 °C for 8 hr.

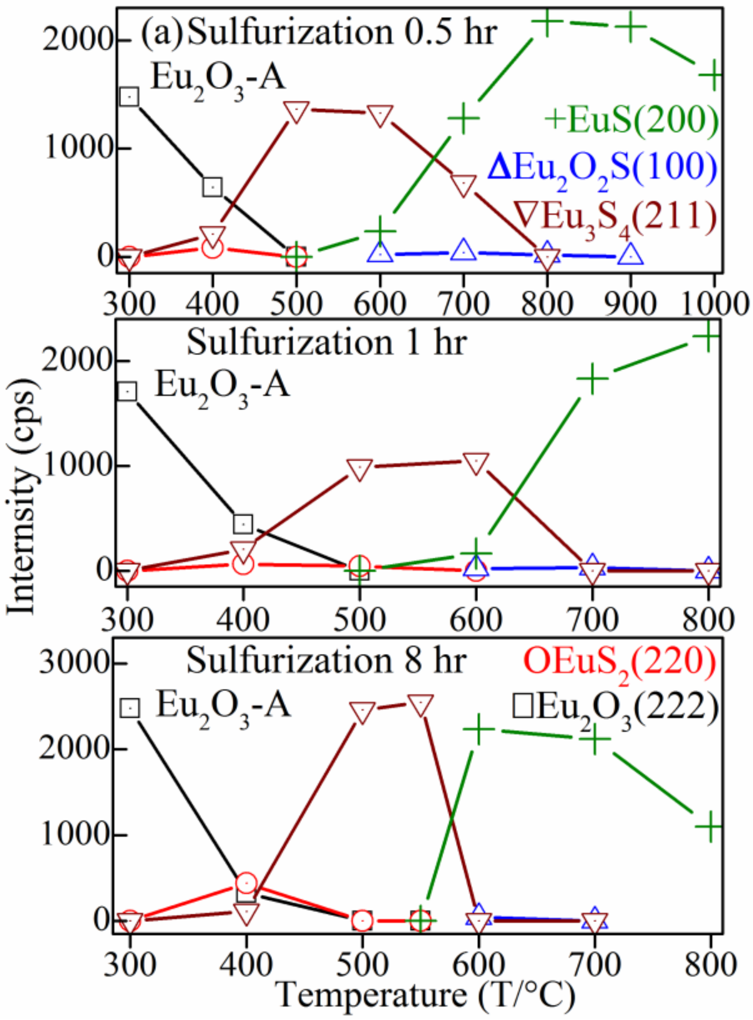

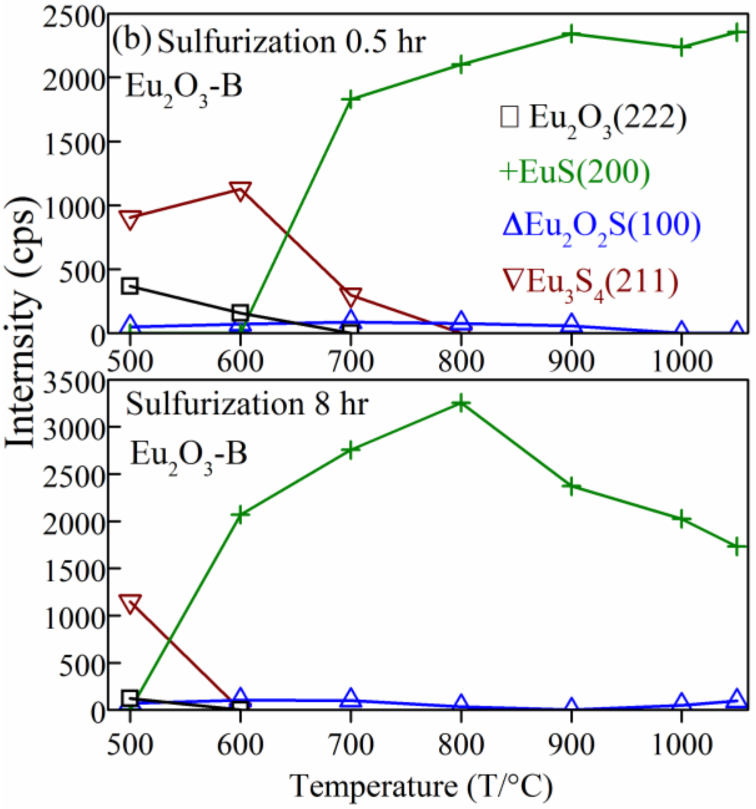

Figure 3.5 Temperature dependences of diffraction intensity of EuS (200), Eu_2O_2S (100), Eu_3S_4 (211), EuS_2 (220) and Eu_2O_3 (222) formed via CS_2 sulfurization of Eu_2O_3-A at 500 °C - 1050 °C for 0.5, 1, and 8 hr with gas flow rate of 1.67 mL/s

3.3.3 Morphology and specific surface area of EuS particles

Figure 3.6 shows typical SEM micrographs of synthetics formed by the sulfurization of Eu_2O_3-A powders. The shape of Eu_3S_4 produced at 500 °C for 0.5 hr with GFR of 1.67 mL/s (Fig. 3.6a) is similar with that of Eu_2O_3-A (Fig. 3.1a). Following sulfurization temperature increased to 800 °C, Eu_3S_4 phase transformed to EuS phase (Fig. 3.6b). The transformation of Eu_3S_4-to-EuS was accelerated by increase of impurity content, just like the effecting of carbon on the sintered La_2S_3 powders [112]. The important point to note is the shape of single EuS is similar with that of Eu_2O_3-A.

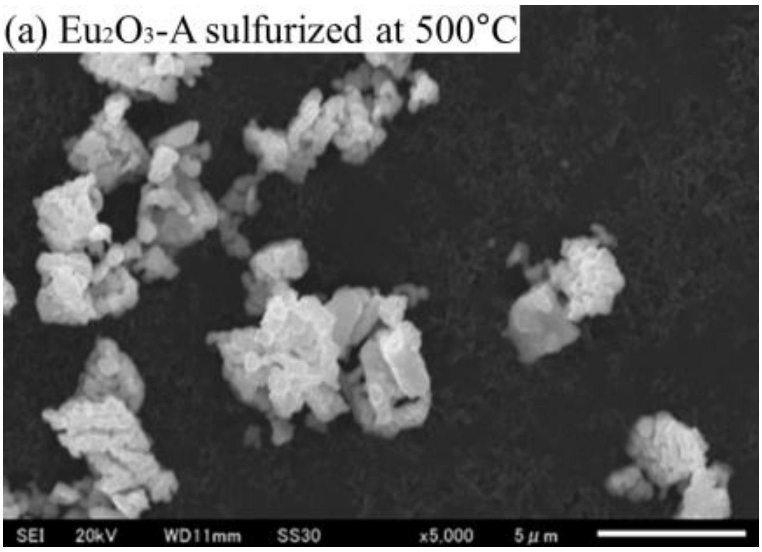
(a) Eu_2O_3-A sulfurized at 500°C

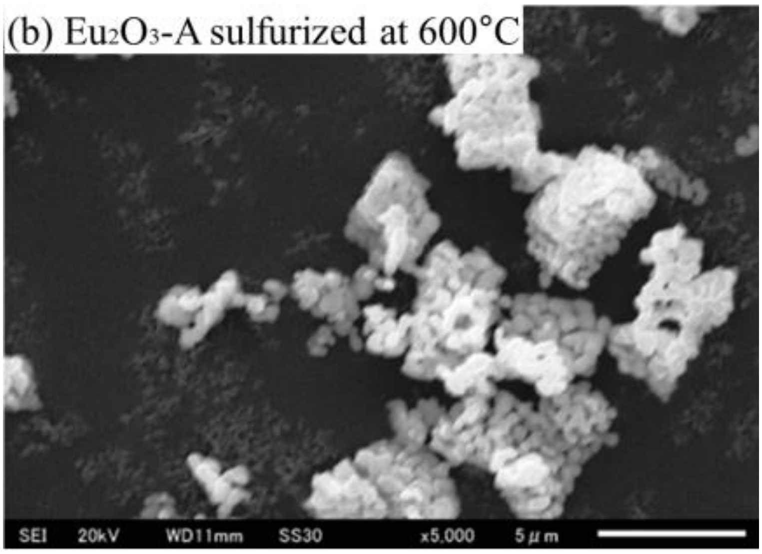
(b) Eu_2O_3-A sulfurized at 600°C

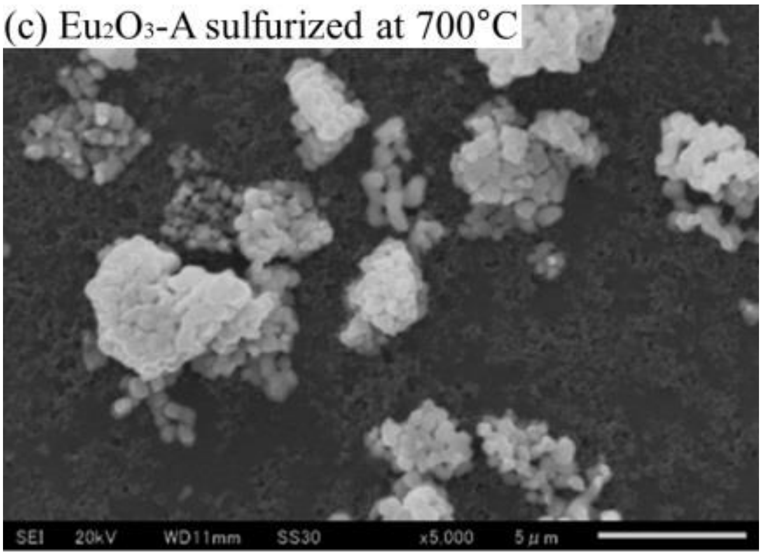
(c) Eu_2O_3-A sulfurized at 700°C

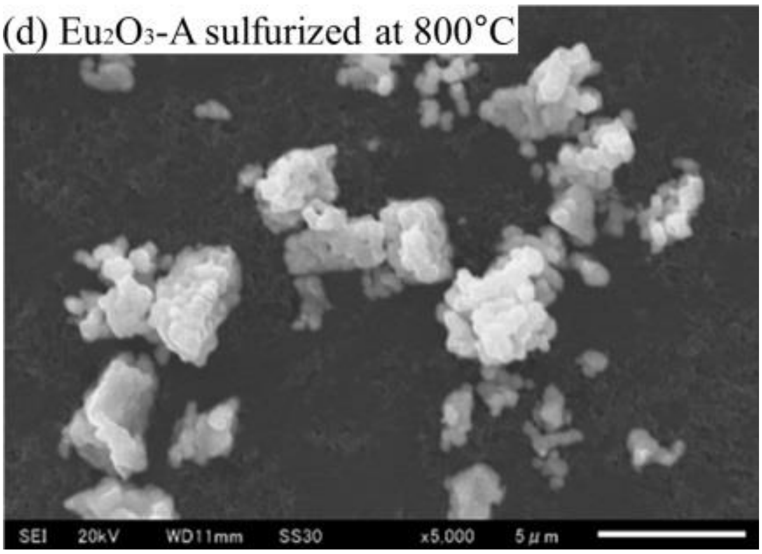

Figure 3.6 SEM micrographs of Eu_3S_4 and EuS formed by the sulfurization of Eu_2O_3-A

Figure 3.7 shows SEM micrographs of the sulfurization products formed by sulfurization at 600-800 °C for 3 hr. Single phase EuS was obtained at 800 °C for the same sulfurization time. Similar to Eu_3S_4, agglomeration of primary EuS particles generated secondary particles. As shown in the SEM images, the average size of the primary particles tended to become larger as the sulfurization temperature increased.

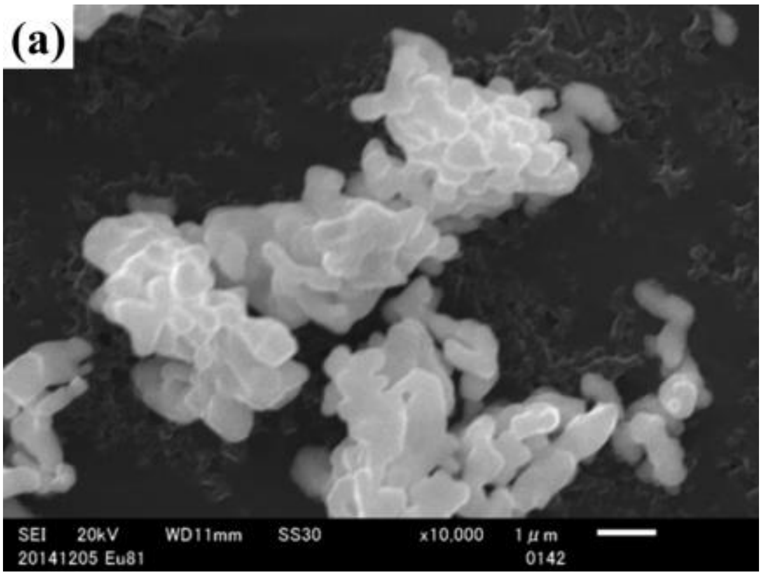

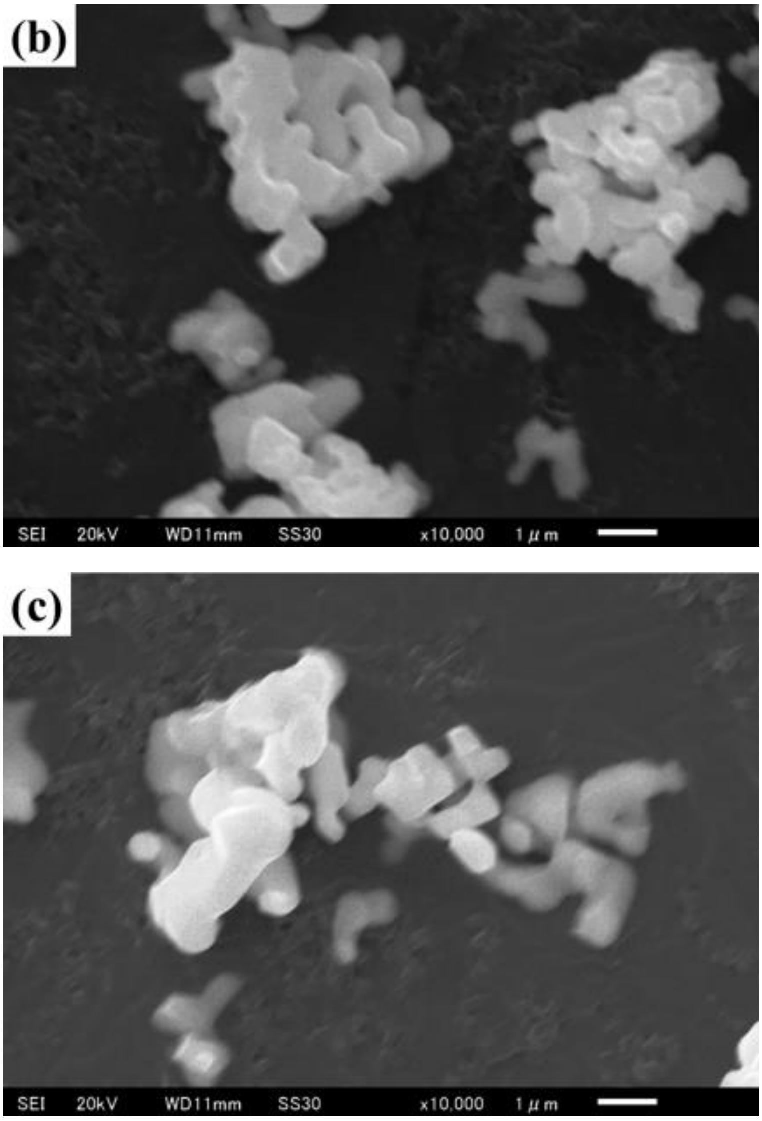

Figure 3.7 SEM micrographs of the sulfurization products formed by sulfurization at 600-800 °C for 3 hr

Figure 3.8 shows SEM micrographs of EuS formed by the sulfurization of Eu_2O_3-B at 900 - 1050 °C for 0.5-2 hr with GFR of 1.67 mL/s. Fig. 3.8a shows the partial agglutination of single EuS phase. In Fig. 3.8b, the sulfurization product has larger particle size than that of EuS in Fig. 3.8a, inferring that EuS particle grows as the temperature increases to 1050 °C. Gas flow rate has little effect on the morphology of sulfurization products as shown in Fig. 3.8d - f. The differences of Eu_2O_3-A and Eu_2O_3-B are smaller as shown in Fig. 3.1, but the shapes of synthetic EuS are differences.

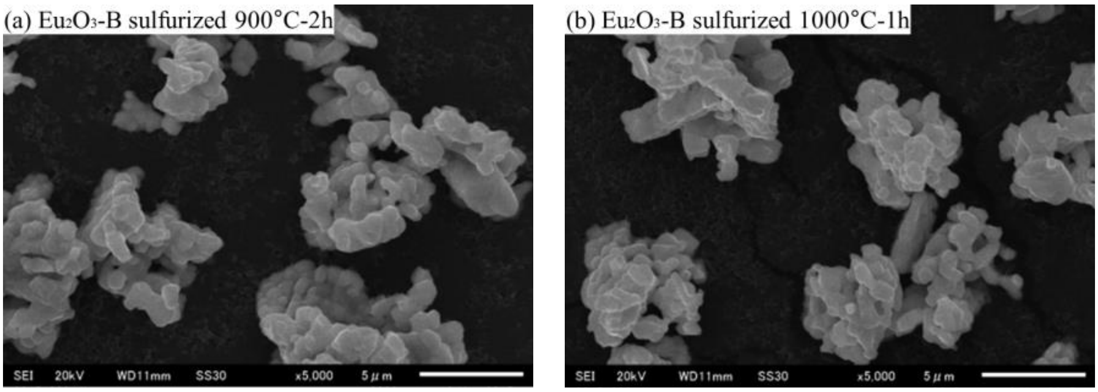
(a) Eu_2O_3-B sulfurized 900°C-2h

(b) Eu_2O_3-B sulfurized 1000°C-1h

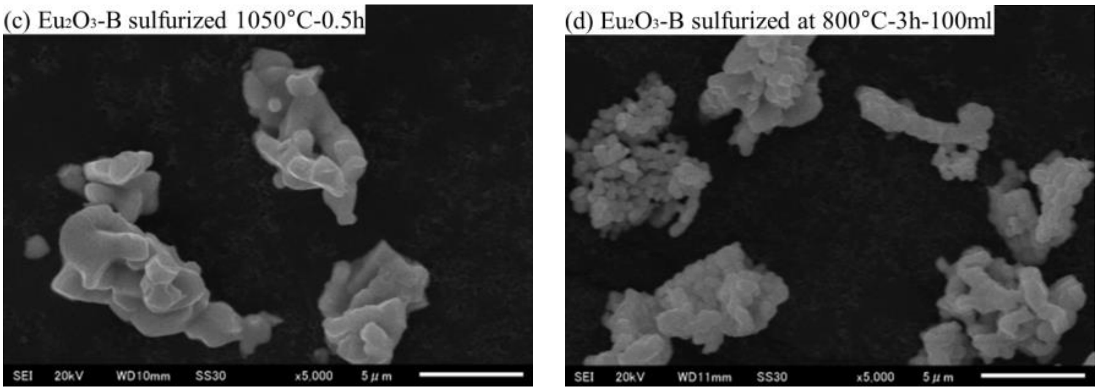
(c) Eu_2O_3-B sulfurized 1050°C-0.5h

(d) Eu_2O_3-B sulfurized at 800°C-3h-100ml

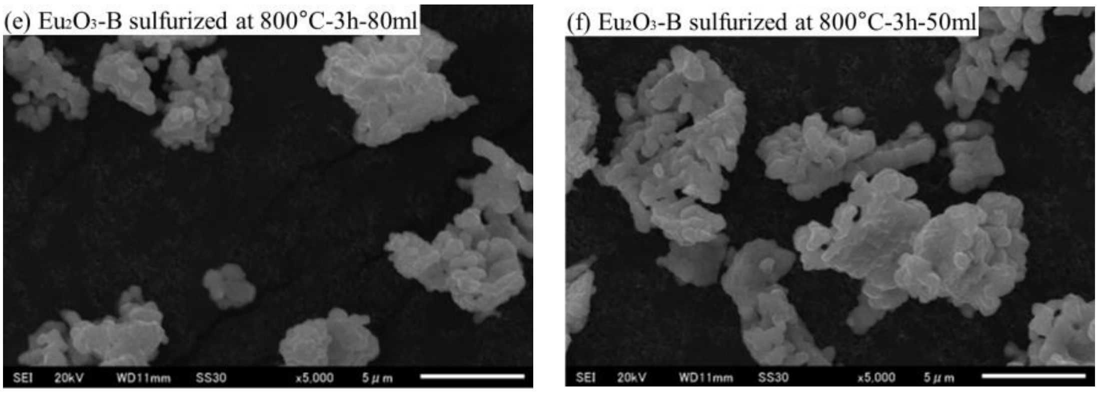
(e) Eu_2O_3-B sulfurized at 800°C-3h-80ml

(f) Eu_2O_3-B sulfurized at 800°C-3h-50ml

Figure 3.8 SEM micrographs of EuS formed by the sulfurization of Eu_2O_3-B at 900 - 1050 °C for 0.5-2 hr with GFR of 1.67 mL/s

Figure 3.9 shows SEM micrographs of EuS produced by the sulfurization of Eu_2O_3-C powders with GFR of 1.67 mL/s. In Fig. 3.9a and Fig. 3.9b, grain size and shape of EuS are different with that of primary Eu_2O_3-C particles (Fig. 3.1c), which is same with H_2S-gas sulfurization of Eu_2O_3 nanowires [109]. Both variation of the oxidation state of europium from trivalent to divalent and the anion exchange process for Eu_2O_3 to EuS need high sulfurization temperature, which destroys the morphology of the oxide nanowires resulting in highly sintered agglomerated materials [109]. Moreover, grain size of synthetic EuS became larger with the rising of temperature.

(a) Eu_2O_3-C sulfurized at 750°C

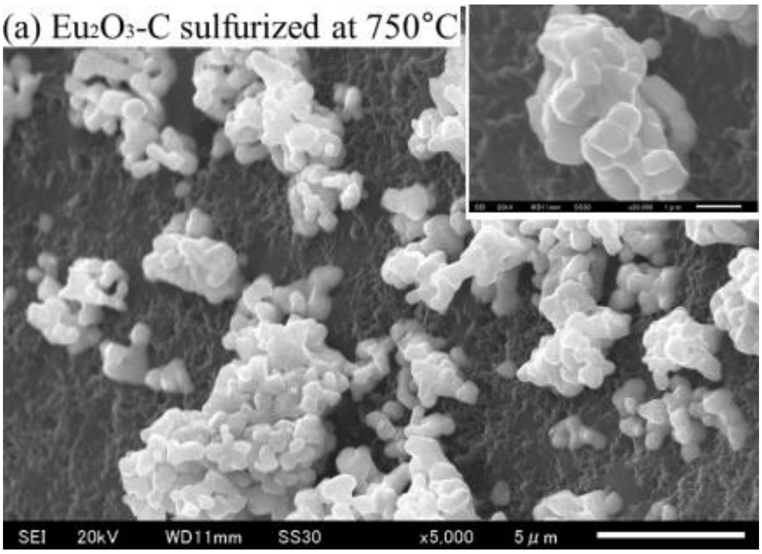

(b) Eu_2O_3-C sulfurized at 1050°C

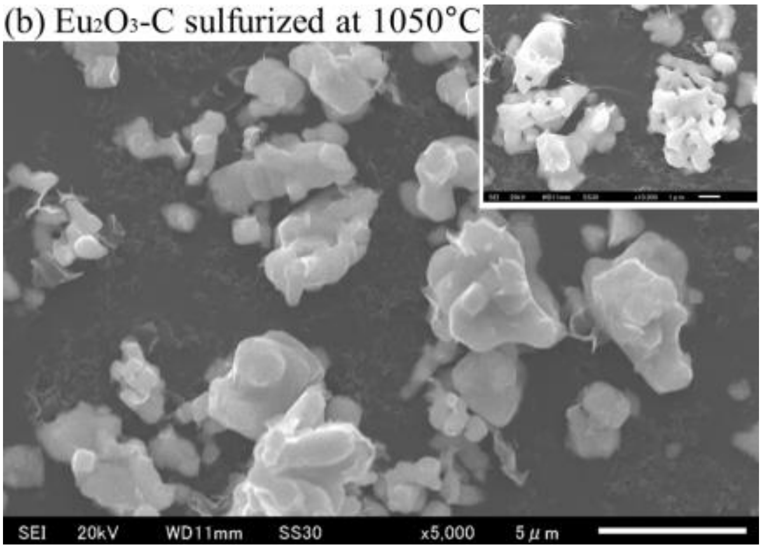

Figure 3.9 shows SEM micrographs of EuS produced by the sulfurization of Eu_2O_3-C powders with GFR of 1.67 mL/s

Figure 3.10 shows particle size distributions of Eu_2O_3, Eu_3S_4 sulfurized at 500 °C and EuS powders sulfurized at 800 °C, respectively. The average particle size of Eu_2O_3 is 4.15 μm. Compared with Eu_2O_3 powder, the distribution of synthetic Eu_3S_4 and EuS reflects a broad range of particle sizes with poor uniformity. The average particle size of synthetic Eu_3S_4 is 6.95 μm, which is smaller than that of EuS (11.37 μm). Both Eu_3S_4 and EuS have larger particles than that of Eu_2O_3.

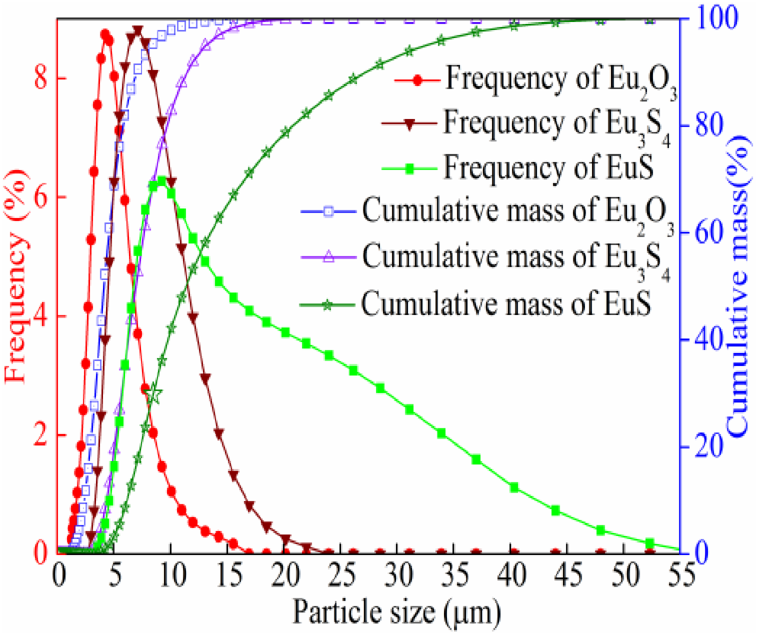

Figure 3.10 Particle size distributions of Eu_2O_3, Eu_3S_4, and EuS

The SSA of the sulfurization products obtained from Eu_2O_3-A at 400 - 800 °C for 1-3 hr are summarized in Fig. 3.11. The SSA of all sulfurization products was smaller than that of the parent Eu_2O_3-A (9.37 m^2/g), indicating that the SSA of the synthetics decreased and the particle size increased during the sulfurization process. It was confirmed that the SSA decreased as the sulfurization temperature and time increased. This is due to grain growth with increasing sulfurization temperature and time, which leads to the reduction of the SSA. When EuS was formed subsequently to the formation of single-phase Eu_3S_4 at 500 °C, the SSA declined to a lesser extent, and eventually the SSA increased slightly. The density of EuS (5.71 g/cm^3) is less than that of Eu_3S_4 (6.26 g/cm^3); thus, the decrease in the density caused a slight increase in the volume of the sample when the transformation described in Equation (1) occurred to form EuS. This also led to an increase of the SSA.

$$Eu_3S_4\ (s) \rightarrow 3\ EuS\ (s) + 1/2\ S_2\ (g) \qquad (1)$$

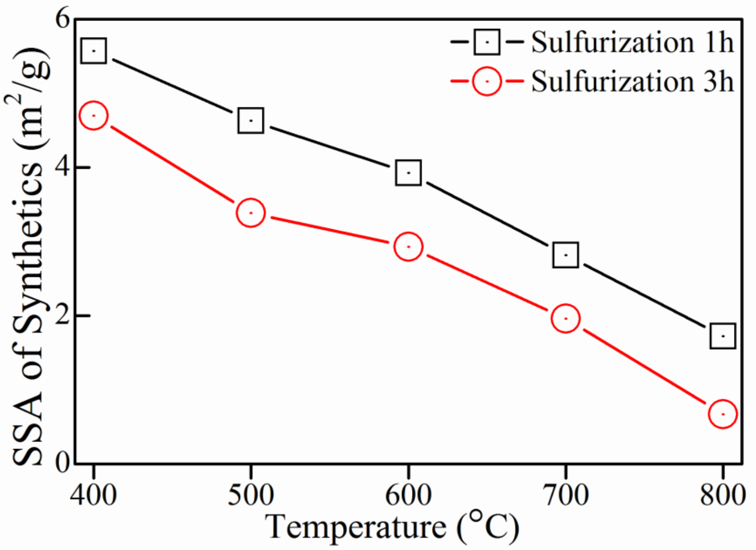

Figure 3.11 SSA of the sulfurization products obtained from Eu_2O_3-A at 400 - 800 °C for 1-3 hr

3.3.4 Thermodynamic analysis of sulfurization process

CS_2 sulfurization of Eu_2O_3 is a complex reaction process. The proposed reactions that occur during CS_2 sulfurization of Eu_2O_3, in addition to that in Equation (1), are described below. The sulfurization reaction of H_2S gas is also described below.

Eu_2O_3 (s) + $3CS_2$ (g) → $2/3Eu_3S_4$ (s) + 3COS (g) + $1/6S_2$ (g) [113] (2)

Eu_2O_3 (s) + CS_2 (g) → Eu_2O_2S (s) + COS (g) [114] (3)

Eu_2O_3 (s) + $3/2CS_2$ (g) → 2EuS (s) +$1/2S_2$ (g) + $3/2CO_2$ (g) (4)

Eu_2O_3 (s) +$3/2CS_2$ (g) → 1/2 EuS_2 (s) + $1/2Eu_3S_4$ (s) + $3/2CO_2$ (g) (5)

EuS_2 (s) → $1/3Eu_3S_4$ (s) + $1/3S_2$ (g) (6)

Eu_2O_3 (s) + EuS_2 (s) → $3/2Eu_2O_2S$ (s) + $1/4S_2$ (g) (7)

Eu_2O_3(s) + $3H_2S$ (g) → 2EuS (s) +$1/2S_2$ (g) + $3H_2O$ (g) (8)

Eu_2O_3 (s) + EuS (s) + $1/4S_2$ (g) → $3/2Eu_2O_2S$ (s) (9)

Eu_2O_3 (s) + $1/2Eu_3S_4$(s) → $3/2Eu_2O_2S$ (s) + 1/2EuS (s) (10)

The temperature dependences of the standard free-energy changes (ΔG^o) for most of these reactions were calculated from the thermodynamic data [113-115] as shown in Fig. 3.12. The sulfurization reaction is considered to proceed mainly due to Equations (2), (3), and (4). Comparison of Equation (2) with Equation (3) shows that the negative value of ΔG^o is larger in Equation (2) than that of Equation (3) at low temperatures and smaller at high temperatures. Therefore, Eu_3S_4 and Eu_2O_2S are predicted to be formed at low and high temperatures, respectively.

Since ΔG° in Equation (4) exhibits positive and negative values at low and high temperatures, respectively, EuS is predicted to be formed only at high temperatures. Shafer et al. [106] reported that when the sulfurization of Eu_2O_3 powder was performed using H_2S gas until equilibrium was reached, Eu_2O_2S was formed at 400 - 550 °C, Eu_2O_2S and Eu_3S_4 were formed at 575 -650 °C, Eu_3S_4 containing a small amount of EuS was formed at 700 °C, and single-phase EuS was obtained at 950 °C or higher. Therefore, this reaction mechanism can be generally predicted from Fig. 3.12.

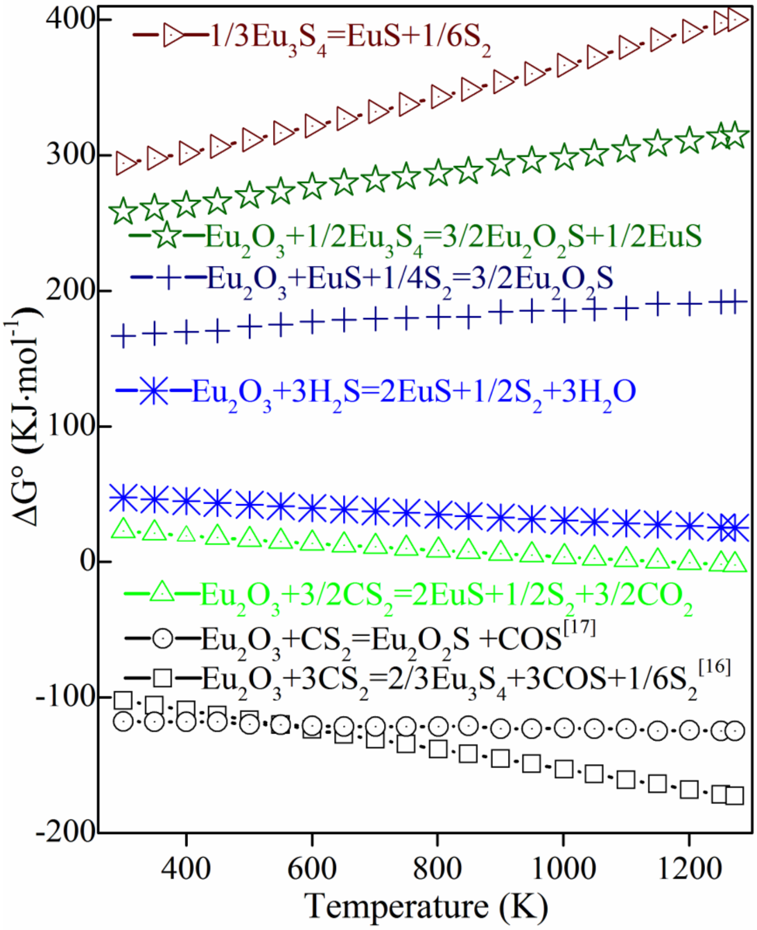

Figure 3.12 Temperature dependence of standard free-energy change for the reactions

In the present research, when Eu_3S_4 was first formed from Eu_2O_3, EuS_2 was formed instead of Eu_2O_2S, and a small amount of Eu_2O_2S was formed in the temperature range where Eu_3S_4 and EuS coexisted. Although the particle size of Eu_2O_3 used by Shafer et al. [106] is unknown, the particle size of Eu_2O_3 is smaller. Therefore, the excellent reactivity of Eu_2O_3, the formation of EuS_2 instead of Eu_2O_2S, and the formation of Eu_2O_2S, in which trivalent Eu (as a component of Eu_3S_4) utilized the oxygen in Eu_3S_4, can be explained. When Equation (4) is compared with Equation (8), it can be understood that the reactivity of CS_2 gas is superior to that of H_2S gas. The reaction mechanism that is operative in the present study is thought to differ from that performed by Shafer et al. because of the excellent reactivity of CS_2 gas and Eu_2O_3 utilized in the present study.

Figure 3.13 summarizes the relationship between the sulfurization conditions and the products from the sulfurization of Eu_2O_3-A. No reaction was observed at 300 °C. A mixture of Eu_2O_3, EuS_2, and Eu_3S_4 was synthesized at 400 °C with a treatment time of less than 3 hr. When the sulfurization time increased from 3 to 8 hr, EuS_2 and Eu_3S_4 became the prominent phases. For sulfurization at 500 °C, single-phase $Eu_3S_4$was formed regardless of the sulfurization time. At 600 °C, EuS was also formed in addition to Eu_3S_4, and a small amount of Eu_2O_2S was also detected. Subsequently, single-phase EuS was obtained by sulfurization at 800 °C for 3 hr, and at 900 °C for 0.5 hr; i.e., the sulfurization time decreased as the sulfurization temperature increased. The results show that the reaction sequence with increasing temperature was as follows: Eu_2O_3 → EuS_2 (400 °C) → Eu_3S_4 (400 - 500 °C) → EuS (Eu_2O_2S above 600 °C). Europium was reduced from the trivalent state to the divalent state with increasing sulfurization temperature.

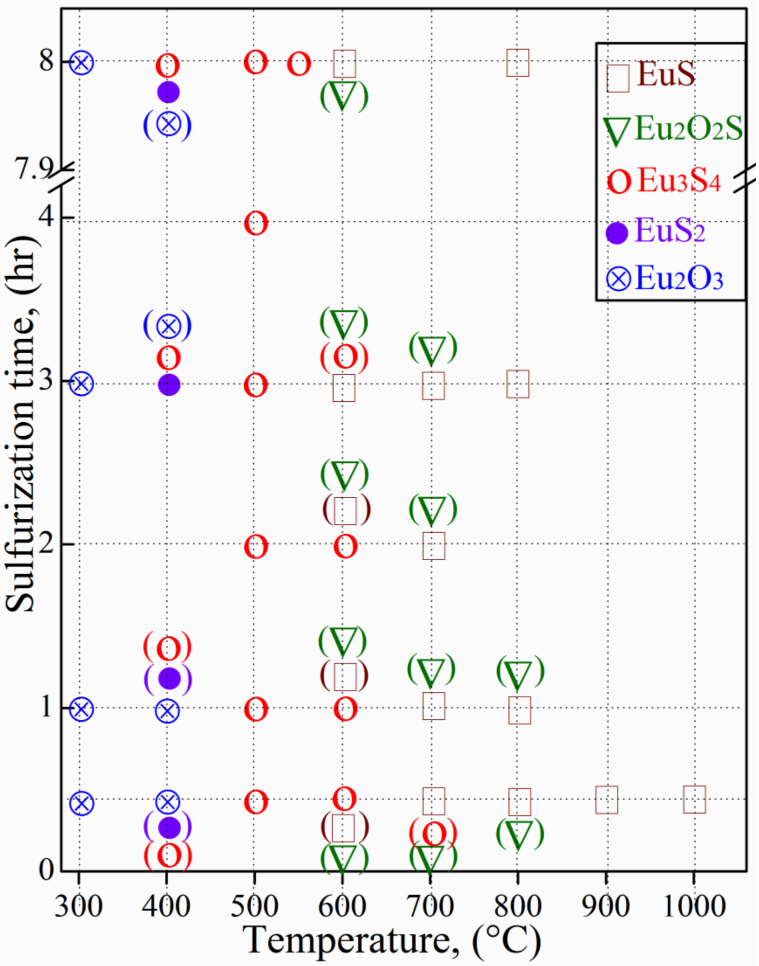

Figure 3.13 Relationship of sulfurization products with sulfurization conditions for Eu_2O_3-A

3.4 Heat treatment of synthesized Eu_3S_4

In Chapter 2.3, the phase transformation from orthorhombic Yb_2S_3 to hexagonal Yb_2S_3 reportedly occurred when heat treatment was performed at 1000 °C for 3 hr in an Ar/CS_2 atmosphere, but this phase transformation did not occur under the same conditions in an Ar atmosphere [116]. Moreover, hexagonal Yb_2S_3 was transformed to Yb_3S_4 with treatment at 1000 - 1050 °C for 12 hr under Ar atmosphere. To confirm the stability of Eu_3S_4 under different atmospheres, synthesized Eu_3S_4 was heat treated for 1 hr under Ar/CS_2 or Ar atmosphere. The XRD patterns of the heat-treated products derived from Eu_3S_4 are shown in Figure 3.14. Eu_3S_4 sulfurized at 500 °C for 8 hr was employed as the starting material for heat treatment.

XRD patterns of the heat-treated products derived from Eu_3S_4 are shown in Figure 3.14. The synthesized Eu_3S_4 powders underwent phase transition at 600 °C under Ar/CS_2 atmosphere. Transformation of Eu_3S_4 to EuS was completed at 700 °C.

However, weak characteristic peaks of Eu_2O_2S remained after heat treatment at 800 °C under Ar atmosphere. The striking differences between these two atmospheres are the reducibility and sulfur vapor pressure. The difference between Ar/CS_2 or Ar atmosphere is that the reductive gas CS_2 can avoid the formation of Eu_2O_2S compared with Ar atmosphere. The generated EuS is very easy to be oxidation under Ar atmosphere. On the other hand, the sulfur vapor pressure under Ar/CS_2 atmosphere is higher than that of Ar atmosphere. Theoretically, the decomposition of Eu_3S_4 is inhibited so the reaction rate may be slow under Ar/CS_2 atmosphere.

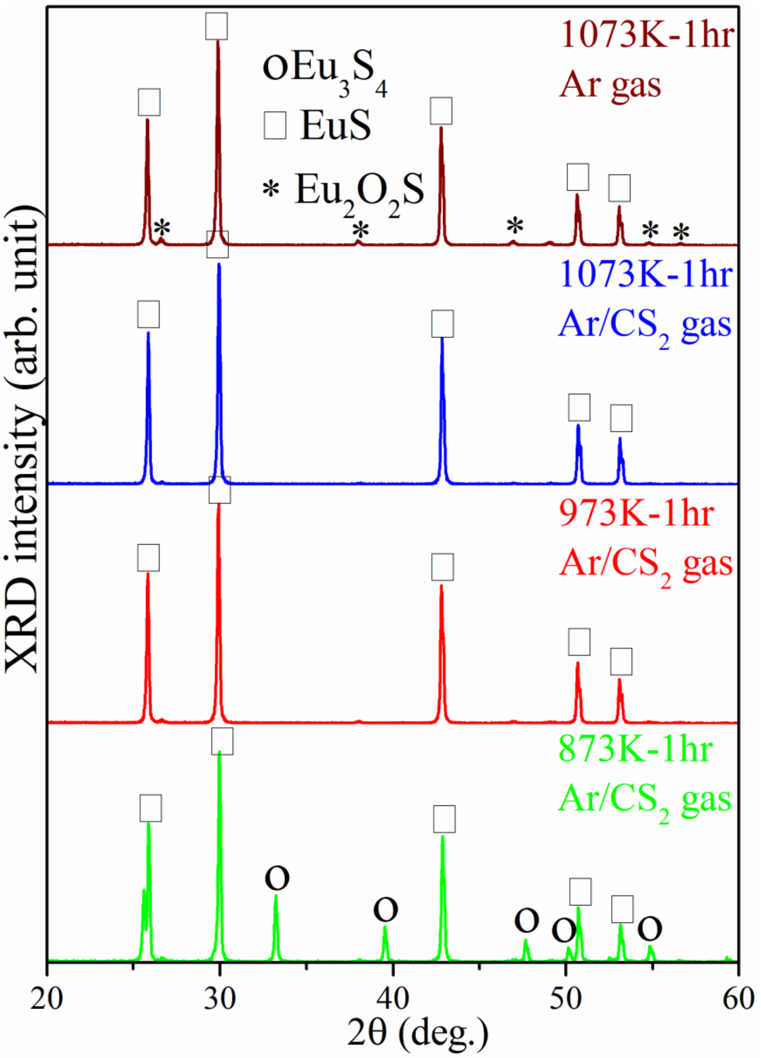

Figure 3.14 XRD patterns of synthetics from Eu_3S_4 under Ar or Ar/CS_2 atmosphere

To clearly illustrate the influence of sulfur vapor pressure, representative XRD patterns of the reaction products from Eu_3S_4 treated under vacuum are shown in Fig. 3.15. During the annealing process, Eu_3S_4 was stable at 500 °C and the vapor pressure of sulfur increased due to the decomposition of Eu_3S_4. Diffraction peaks of EuS were observed with treatment at 550 °C for 1 hr, and single-phase EuS was formed by annealing at 600 °C. Furthermore, when EuS was annealed at the higher temperature of 1500 °C, no decomposition occurred due to the high melting point of EuS. The phase transformation of Eu_3S_4-to-EuS is similar with that of Yb_3S_4-to-YbS at 1500 -1550 °C under vacuum. The crystal structures of Eu_3S_4 and EuS are Th_3P_4-type (space group I-43d) and NaCl-type crystal structure (space group Fm3m), respectively. Moreover, Eu_3S_4 included bivalent and trivalent Eu ion, but EuS usually contained bivalent Eu ion. Bivalent Eu ion is more stable than trivalent Eu at high temperature, so Eu_3S_4 transformed to EuS at high temperature.

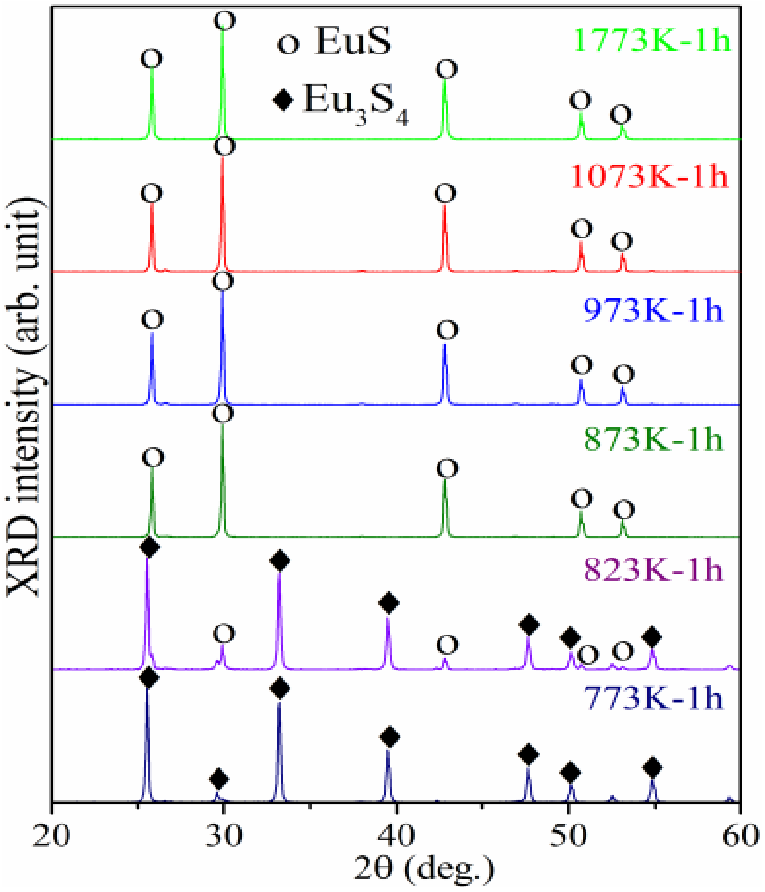

Figure 3.15 XRD patterns of synthetics from Eu_3S_4 under vacuum

Figure 3.16 shows lattice parameters of EuS/Eu_3S_4 from Eu_3S_4 treated at 400-1050 °C for 1 hr under Ar or Ar/CS_2 atmospheres. Compared with initial Eu_3S_4, lattice parameter of Eu_3S_4 is about 8.53 Å and has no obvious change after treated at 400 °C or 600 °C under Ar atmosphere. Lattice parameter of EuS is almost same with that of sulfurized EuS (5.97 Å). It suggested that both methods, CS_2 sulfurization and heat treatment, can be employed to fabricate high pure EuS.

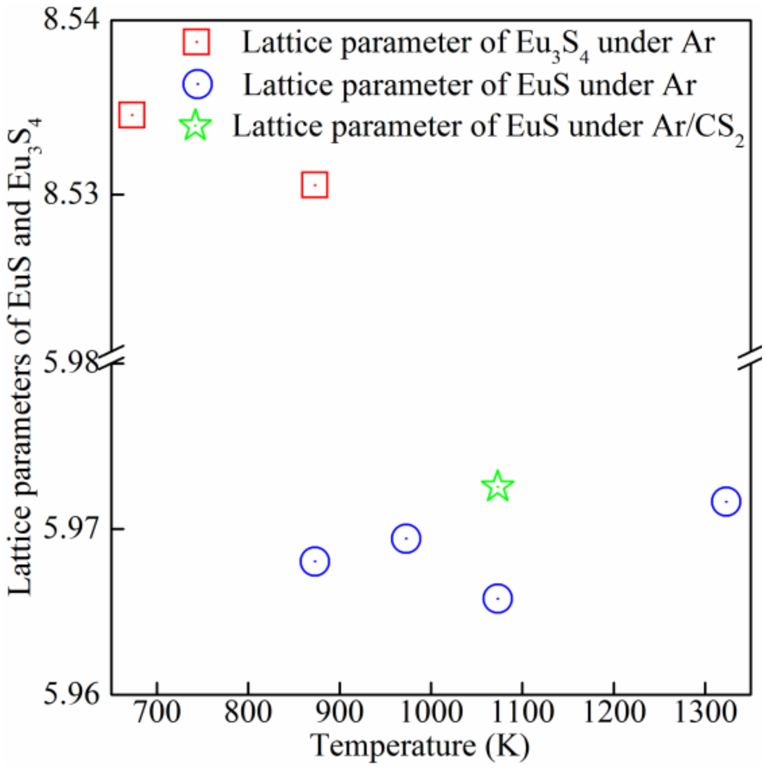

Figure 3.16 Lattice parameters of EuS/Eu$_3$S$_4$ from treated Eu$_3$S$_4$

Figure 3.17 shows SEM micrographs of the products derived from heat-treatment of synthesized Eu$_3$S$_4$ under Ar/CS$_2$ atmosphere. The particle size is similar to that obtained via direct CS$_2$ sulfurization of Eu$_2$O$_3$ at 600 - 800 °C as shown Fig. 3.7. In the case of Eu$_3$S$_4$ as well as Eu$_2$O$_3$, fine primary particles agglomerated to form secondary particles, and the average size of the secondary particles tended to increase as the heat treatment temperature increased. The average size of the primary particles was constant up to the heat treatment temperature of 800 °C, regardless of the types of products.

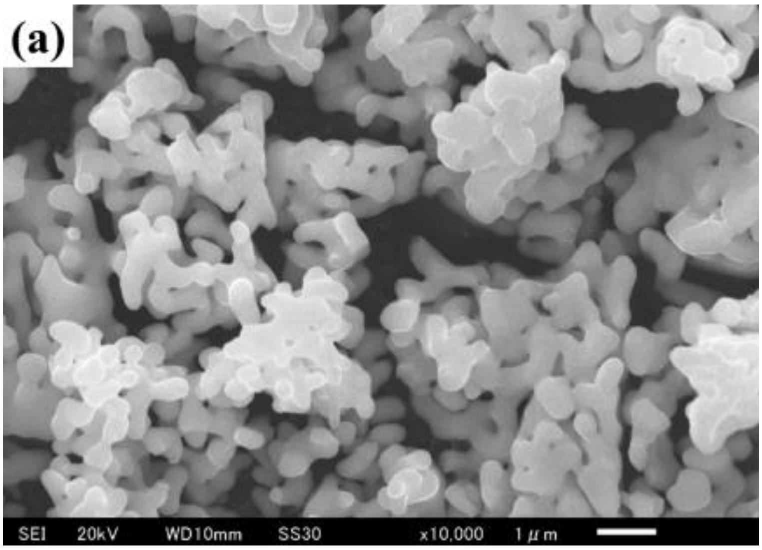
(a)
SEI 20kV WD10mm SS30 x10,000 1 μm

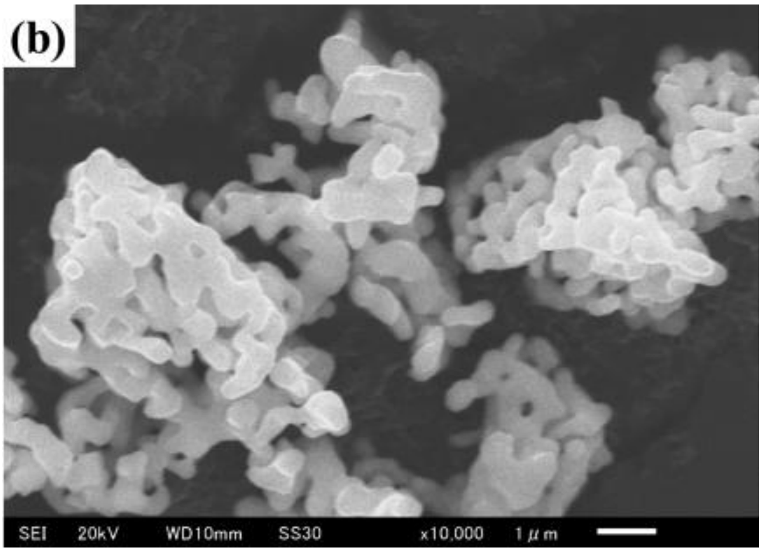
(b)
SEI 20kV WD10mm SS30 x10,000 1 μm

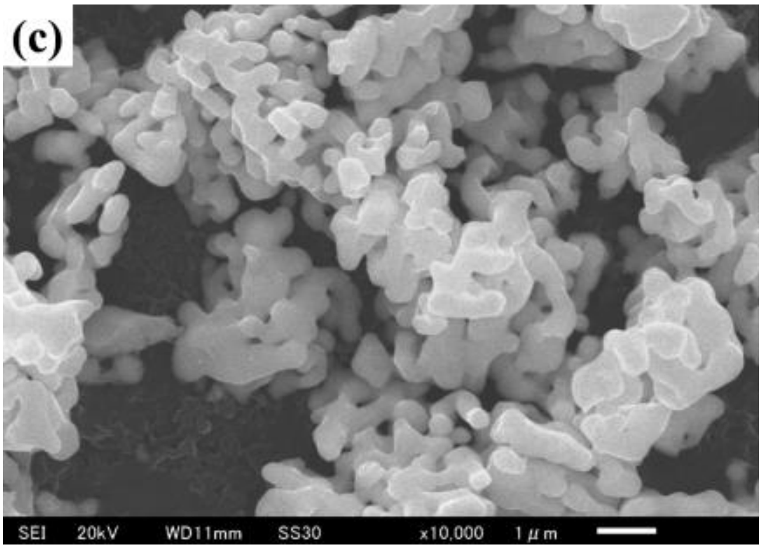
(c)
SEI 20kV WD11mm SS30 x10,000 1 μm

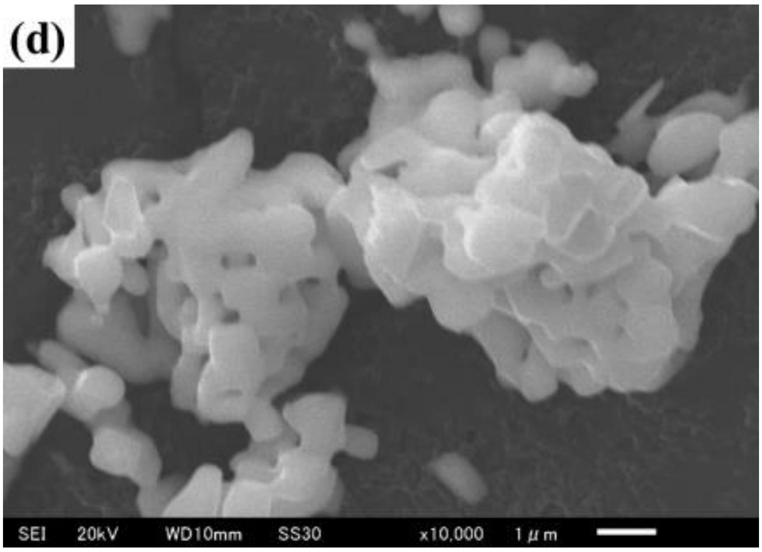

Figure 3.17 SEM micrographs of the products derived from heat-treatment of synthesized Eu_3S_4 under Ar/CS_2 atmosphere

Table 3.3 shows chemical compositions of synthetics by treated Eu_3S_4 powders at 500 - 800 °C for 1 hr under Ar/CS_2 or Ar gas. There is a phase transformation of synthetic Eu_3S_4 powders with Th_3P_4 structure to EuS powders with NaCl structure. The impurity content lessened during this phase transformation following with temperature increase. Moreover, impurity content of EuS treated under Ar/CS_2 gas is lower than that of EuS treated under Ar gas. This result suggested that impurity oxygen can be removed by heat treatment under Ar/CS_2 atmosphere. The phase transformation from Eu_3S_4 to EuS differs from the phase transformation of light rare-earth sesquisulfides R_2S_3 (R = La, Ce, Sm, Nd, and Gd), in which the composition does not change.

Table 3.3 Chemical compositions of synthetics by heat-treated Eu_3S_4 at 500 - 800 °C

Synthetics	Heat-treatment			Composition (mass %)		
	K	hr	Gas	Eu	S	Impurity
Eu_3S_4	773	1	Ar/CS_2	78.44	15.49	6.06
Eu_3S_4/ EuS	873	1	Ar/CS_2	79.08	16.65	4.27
EuS	973	1	Ar/CS_2	82.45	17.36	0.19
EuS	1073	1	Ar/CS_2	82.54	17.37	0.09
EuS	1073	1	Ar	82.02	17.27	0.71

The results of heat-treatment study revealed that enrichment of sulfur was effective for the sulfurization of impurity phase Eu_2O_2S. The decomposition reaction of Eu_3S_4 was confirmed to proceed easily under reduced pressure.

3.5 Sintering and large magnetocaloric effect of synthesized EuS

3.5.1 Sintering of synthetic EuS powder

Representative XRD patterns of synthetics from sulfurized EuS powders at 1000°C ~ 1400°C for 3 hr are shown in Figure 3.18. Single phase EuS compacts can be obtained for all the sintering temperature ranges. There is no characteristic peak of Eu_2O_2S.

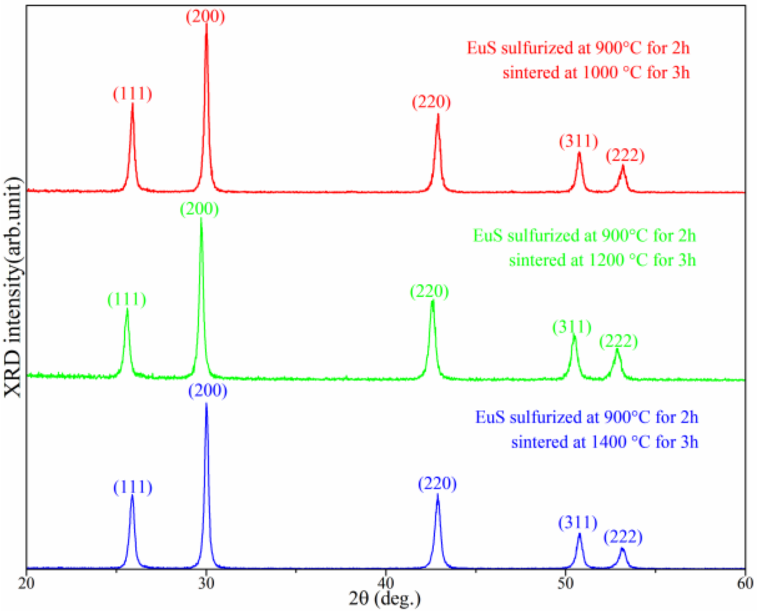

Fig. 3.18 XRD patterns of sintered EuS compacts at 1000 -1400 °C for 3 hr

Figure 3.19 showed SEM image of the sintered EuS for the cross section of fracture surface at 1000 -1400 °C for 3 hr. The EuS powders were from the sulfurization of Eu_2O_3-B by CS_2 gas. The sintered EuS is entirely homogeneous and there is no obviously preferred orientation. In addition, the particle size of the EuS grain becomes larger as sintering temperature increases. On the other hand, the brittle fracture is within the grain boundary and the existence of cleavage plane can explain the crack of sintered EuS.

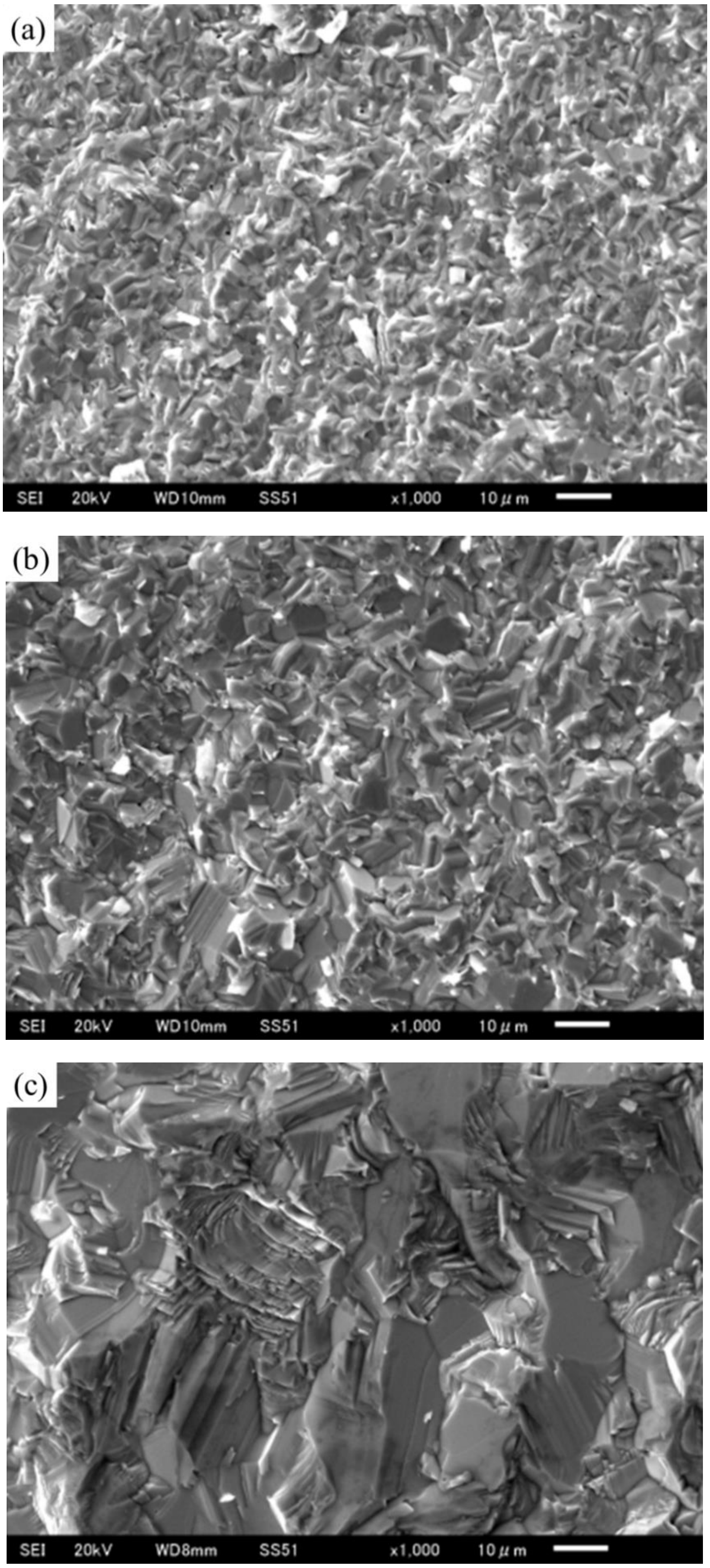

Fig. 3.19 SEM micrograph of EuS sintered at 1000°C (a), 1200 °C (b), and 1400 °C (c) for 3 hr

3.5.2 Magnetization of polycrystalline EuS compacts

Figure 3.20 showed Magnetization M(T) and inverse susceptibility of polycrystalline EuS compact as functions of temperature in a field of 100 Oe. The magnetization of polycrystalline EuS is smaller than that of single crystal EuS, about The PM to FM transition for polycrystalline EuS occurred at around the defined Curie temperature T_c = 16.8 K. the M(T) behavior conform the Curie-Weiss rule with the values of PM Curie temperature θ_P=16.95. This Curie temperature is similar with that of single crystal EuS. However, the field cooling (FC) and zero-field-cooling (ZFC) curves have some difference over the measure temperature range. This result indicates that there are some thermomagnetic irreversibility and magnetic anisotropy for polycrystalline EuS compact.

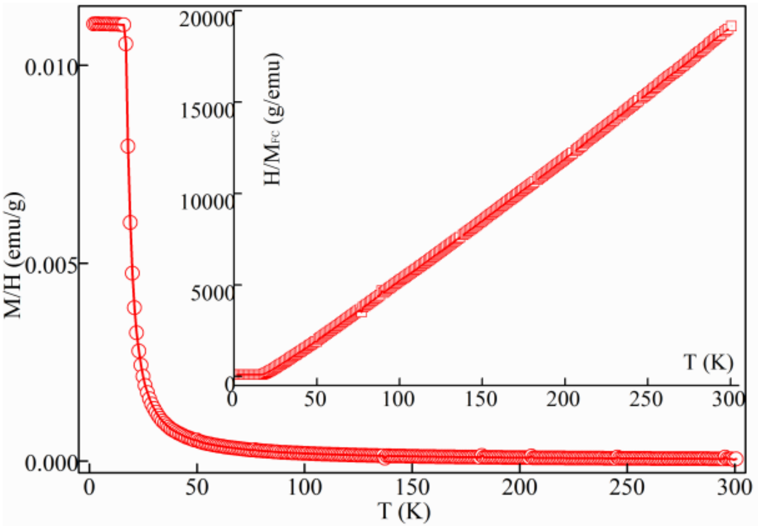

Figure 3.20 Temperature dependences of FC magnetization of polycrystalline EuS

In order to investigate the influence of applied magnetic field on the magnetocaloric property of polycrystalline EuS, the isothermal magnetization curves as a function of magnetic field were measured in applied fields of up to 5 T at around the magnetic transition temperature (16.5 K). Figure 3.21 shows the field dependence of magnetization for sintered EuS at the temperature range of 10 - 30 K. EuS bulks were sintered by spark plasmas sintering under vacuum of 7 $*10^{-3}$ Pa at 1000 °C for 3 hr from EuS powders, which were prepared by sulfurization of Eu_2O_3-B powders at 900 °C for 2 hr. The density of sintered EuS compact is 4.9 g/cm^3 and the grain size of sintered EuS bulk is about 5 μm. XRD pattern suggested sintered EuS bulk was single phase without characteristic peak of Eu_2O_2S. From Fig. 3.21, the M-H characteristics were differences in different temperature ranges. The sintered EuS showed a paramagnetic-to-ferromagnetic transition at below 1 T and then tends to saturate with the rising of magnetic field. A similar behavior has been observed in single crystal EuS applied along the [100] and [110] direction [103].

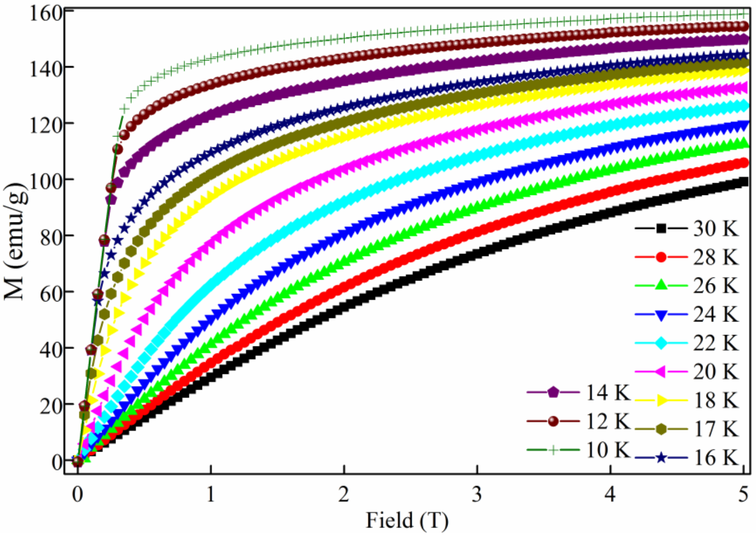

Fig. 3.21 Magnetization of polycrystalline EuS as a function of field

The relationship between magnetization M(H, T)/ M(H, B) for polycrystalline EuS and temperature or magnetic field are shown in Fig. 3.22. EuS compact was sintered by spark plasmas sintering under vacuum of 7 $*10^{-3}$ Pa at 1600 °C from EuS powders, which were prepared by sulfurization of Eu_2O_3-A powders. As seen in Figure 3.21a, M(H, T) showed the ferromagnetic behavior and had different values for a certain field at low temperatures, which is different with that of single crystal EuS with almost the same value for a given and temperature. The magnetization reached the saturation before 1 T at low temperature. This trend became weak following the rising of temperature and the magnetization increases nearly linearly with an increase in magnetic field and this slope reduced with the rising of temperature from 34 K to 50 K. Magnetization lessened with the increase of temperature for a certain field. A slight nonlinearity in the M - H curves is noticed at low temperatures for fields much higher than 4T, which may be ascribed to the existence of impurity of residual carbon or oxygen atom caused by the sulfurization process.

Figure 3.21b showed the temperature dependence of the magnetization of polycrystalline EuS at various magnetic fields. For polycrystalline EuS, a clear jump for magnetization was observed at T_C for the magnetic fields less than 0.6 T. EuS exhibits smooth temperature variation of the magnetization particularly at high fields.

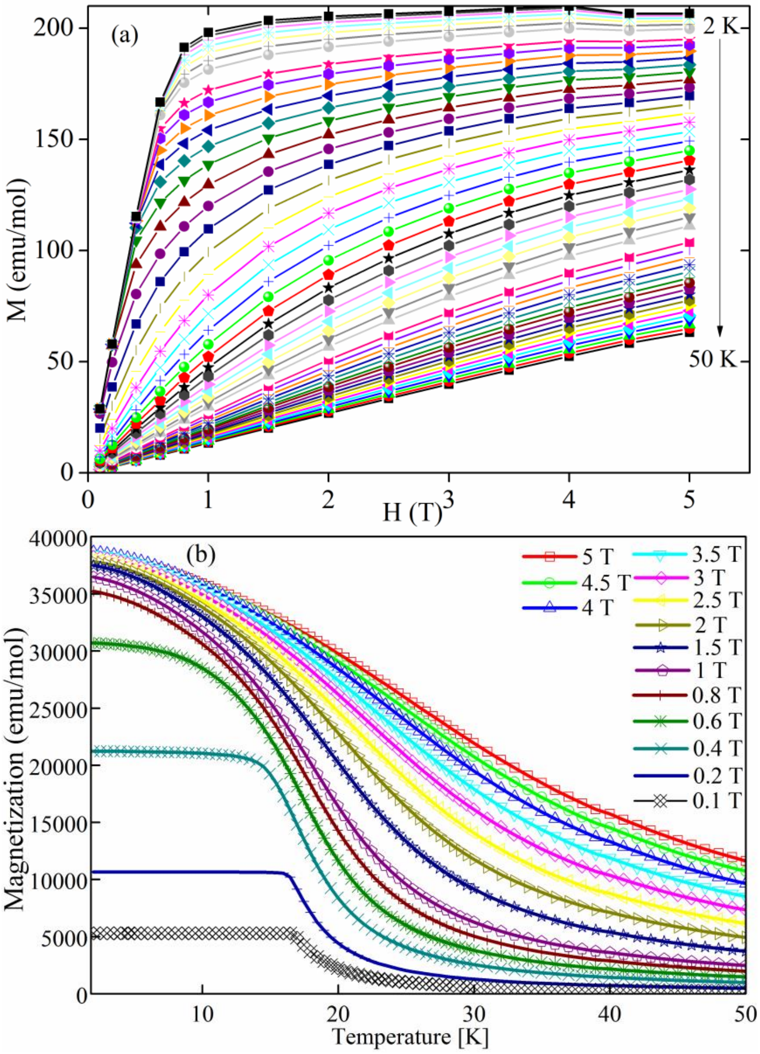

Figure 3.21 Magnetization of polycrystalline EuS as a function of field (a) and temperature (b)

The Arrott plots of polycrystalline EuS compound (from Eu_2O_3-B) sintered at 1000 °C for 3 hr are shown in Fig. 3.22. The negative slope of the Arrott plot confirmed the occurrence of a second order PM-to-FM phase transition. The isothermal magnetic entropy changes have been calculated from the isothermal magnetization data by employing Maxwell's relationship $\Delta S(T, H)= \int_0^H (\frac{\partial M}{\partial T})_H \, dH$. The entropy changes ΔS for different magnetic field changes as a function of temperature are given in Fig. 3.23. The ΔS of polycrystalline show peaks around T_c and the maximum values of ΔS are obtained to be 16.76 J/Kg/K and 28.4 J/Kg/K for the field changes of 2 T and 5 T, respectively. Though these values are slight smaller than those of single crystal EuS under the same magnetic field change, the preparation process is simple and the raw material Eu_2O_3 powders are cheaper and easier to storage. Moreover, the entropy changes ΔS were connected with grain size of sintered EuS [117], grain size and ΔS will be optimize in further study.

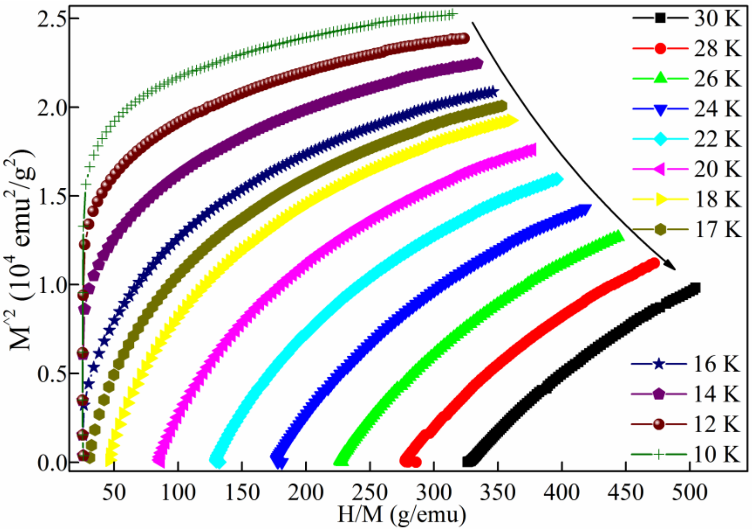

Fig. 3.22 The Arrott plots of polycrystalline EuS sintered at 1000 °C for 3hr from Eu_2O_3-B

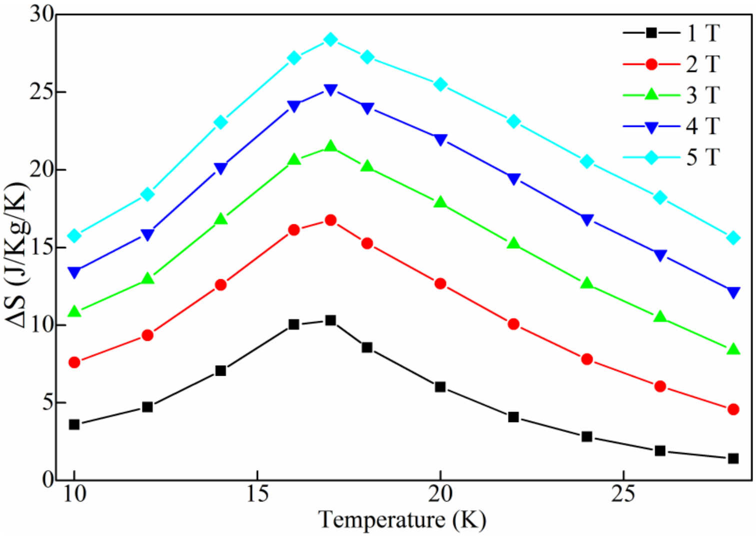

Fig. 3.23 Magnetic entropy change of polycrystalline EuS from Eu_2O_3-B

Figure 3.24 shows Arrott plots of polycrystalline EuS (from Eu_2O_3-A) in which the appearance of the inflection point confirms the occurrence of a magnetic transition from the paramagnetic to ferromagnetic ordering at above T_c. The negative slop of the Arrott plots (M^2 versus H/M) suggests that it is a second order phase transformation.

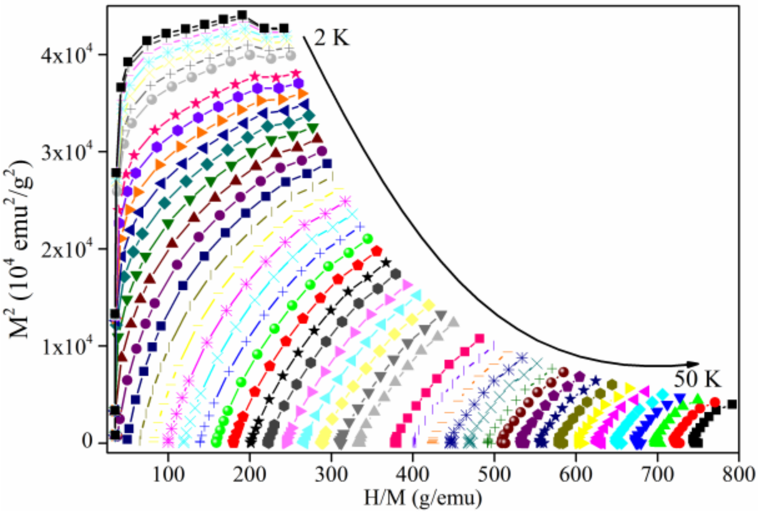

Figure 3.24 The Arrott plots (M^2 versus H/M) of polycrystalline EuS from Eu_2O_3-A

The change in magnetic entropy of polycrystalline EuS (from Eu_2O_3-A) is displayed in Figure 3.25 as a function of the temperature for different magnetic fields. The absolute value of ΔS first increased and began to decrease after reaching a maximum value. Moreover, the corresponding temperature for maximum ΔS increased slightly from 17.47 K for ΔH = 1T to 17.97 K for ΔH = 5T. A large MCE was observed at above Curie temperature. The peak values of ΔS under applied fields of 1, 2, and 5 T are 2.02, 3.57, and 6.32 J/mol/K, respectively. It need to emphasize that the observed ΔS value for polycrystalline EuS is similar with that of single crystal EuS prepared with the more complex process. Such a high magnitude of ΔS was rarely observed in polycrystalline rare-earth monosulfides or sesquisulfides.

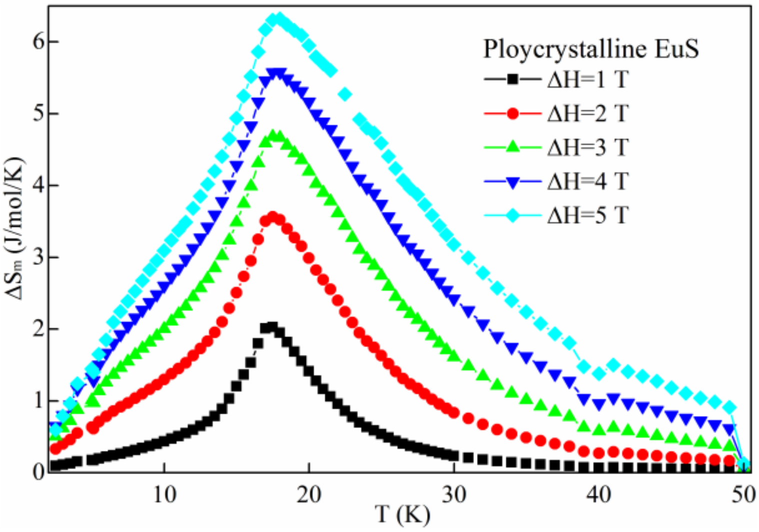

Figure 3.25 Magnetic entropy change of EuS as a function of temperature calculated from the magnetization data

3.5.3 Specific heat of polycrystalline EuS compacts

To calculate the adiabatic temperature change ΔT_{ad} and verify the accuracy of the magnetic entropy change estimated based on the Maxwell relation, the temperature dependence of specific heat C(T) of EuS (from Eu_2O_3-A) was also measured in magnetic fields of zero and 5 T as illustrated in Fig. 3.26. The C(T) curve shows a large peak at around 16.4 K under the zero field. Following the increase of magnetic field, the peak becomes weak and disappeared. The specific heat peak is almost completely smoothed out at 5 T.

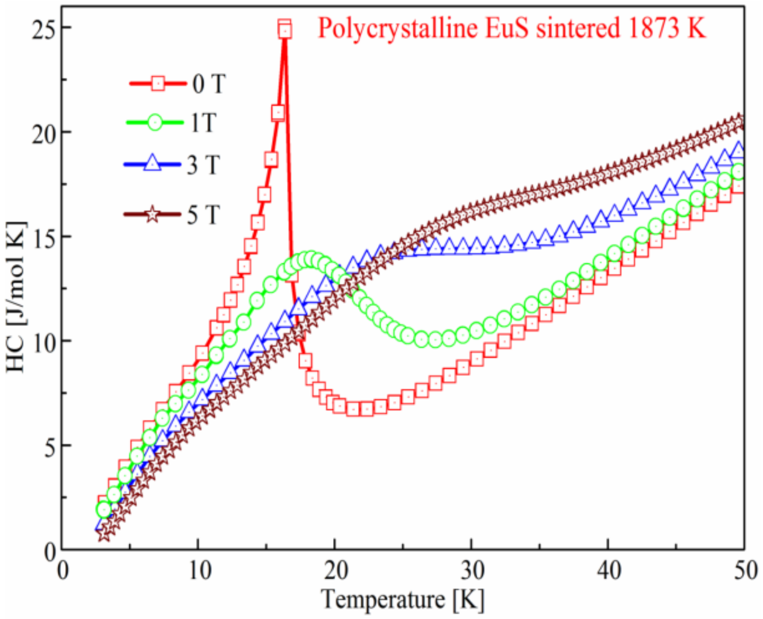

Figure 3.26 Specific heat of EuS measured at different magnetic field

Figure 3.27a showed the calculated results of entropy based on the specific heat data (Figure 3.26). The entropy for polycrystalline EuS has a convex at the about Curie temperature under zero magnetic field. Entropy change of EuS can be calculated by using $\Delta S_m = \Delta S = S(H, T) - S(0, T)$, where, $S(H, T) = \int_0^T [C(H,T)/T]dT$ as shown in Fig. 3.27b. It can be observed from this figure that the calculated results from calorimetric method are slightly smaller than these from the magnetization results and the Maxwell relation.

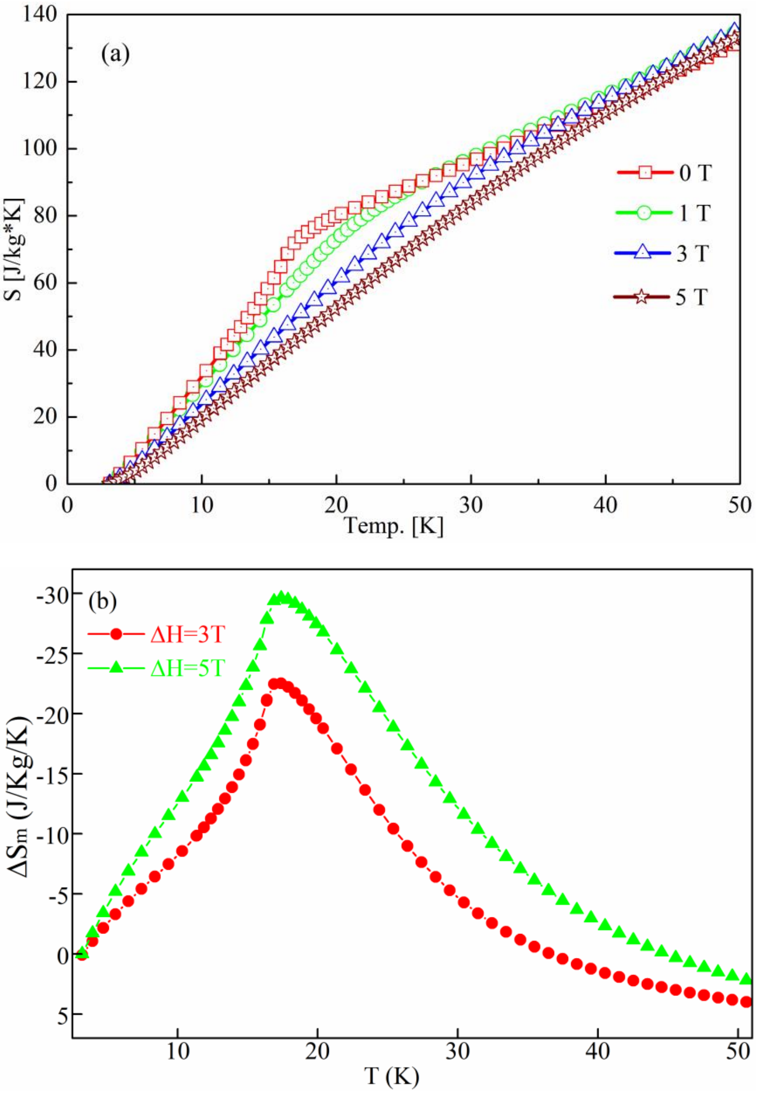

Figure 3.27 Calculated entropy value and change of polycrystalline EuS

To get more believable entropy data and reduce the calculated error, the entropy for polycrystalline EuS (from Eu_2O_3-A) was calculated from the combination of the calorimetric and magnetic data as shown in Figure 3.28. The entropy data from C(T) data under the field of 5T was chosen as the basis (marked as S(5T)). The revised entropy of polycrystalline EuS under zero magnetic field (marked as S(0T)) is computed from the direct plus for S(5T) and ΔS(5T) from the magnetic data. The revised entropy under the field of 1T and 3T can be obtained from the plus of S(0T) with corresponding entropy change from the magnetic data. The revised entropy by matching the specific heat and the magnetization data had a high degree of reliability.

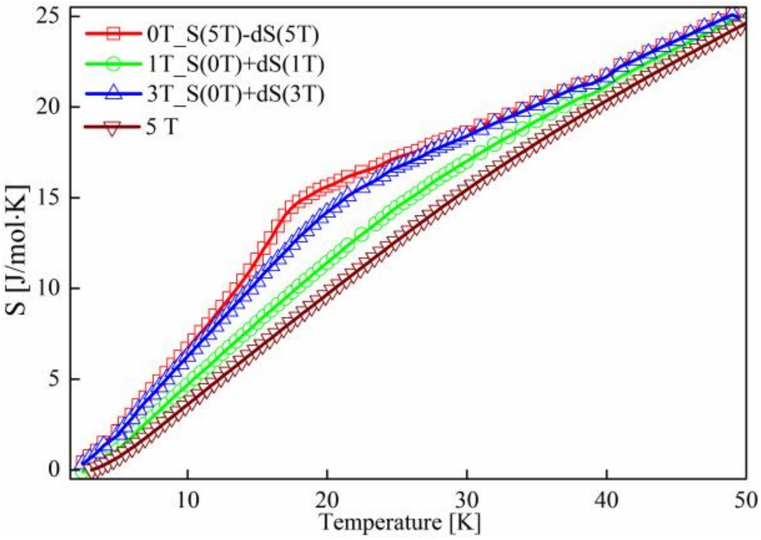

Figure 3.28 the revised entropy for polycrystalline EuS from specific heat and magnetization data

The relative cooling power (RCP) is an important parameter for a magnetic refrigerant material, which is usually defined as RCP $=\left|\Delta S_{max}*\delta T_{FWHM}\right|$, where ΔS_{max} is the maximum of ΔS from Fig. 3.25 and δT_{FWHM} is the full width at half corresponding maximum of ΔS. The ΔS_{max} and RCP were calculated with the above equation as shown in Fig. 3.29. Both ΔS_{max} and RCP have the very large values and increase monotonically with increasing ΔH, indicating that polycrystalline EuS has the outstanding magnetic refrigeration property. The RCP values were 69.26 and 125.39 J/mol for ΔH = 3 T and 5 T, respectively. The RCP for polycrystalline EuS is slightly smaller than that of single crystal (143.94 J/mol) ΔH = 5 T.

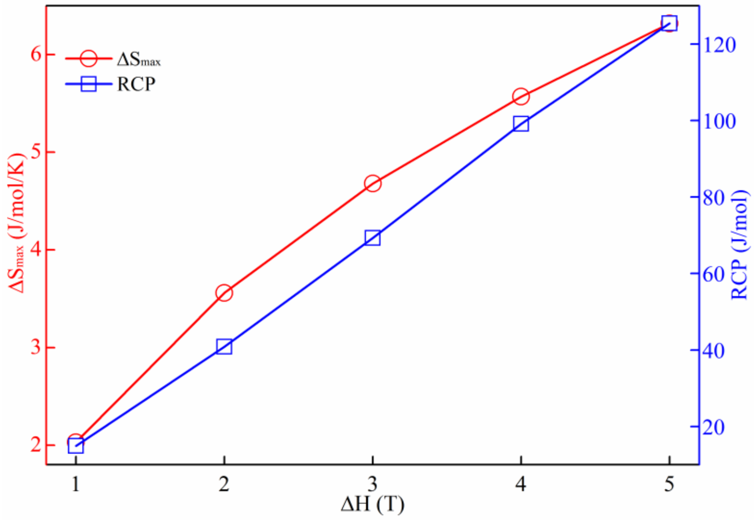

Fig. 3.29 Magnetic field dependences of the maximum magnetic entropy change and the relative cooling power of polycrystalline EuS

3.5.4 Comparison specific heat of polycrystalline and singe crystal EuS

To clearly realize the differences of the magnetocaloric properties between polycrystalline and single crystal EuS, heat capacities for both kinds of EuS under different magnetic fields were compared as shown in Fig. 3.30. The heat capacities values are almost same at lower than 20 K under zero magnetic fields. The heat capacity for paramagnetic polycrystalline EuS phase is slightly smaller than that of single crystal EuS.

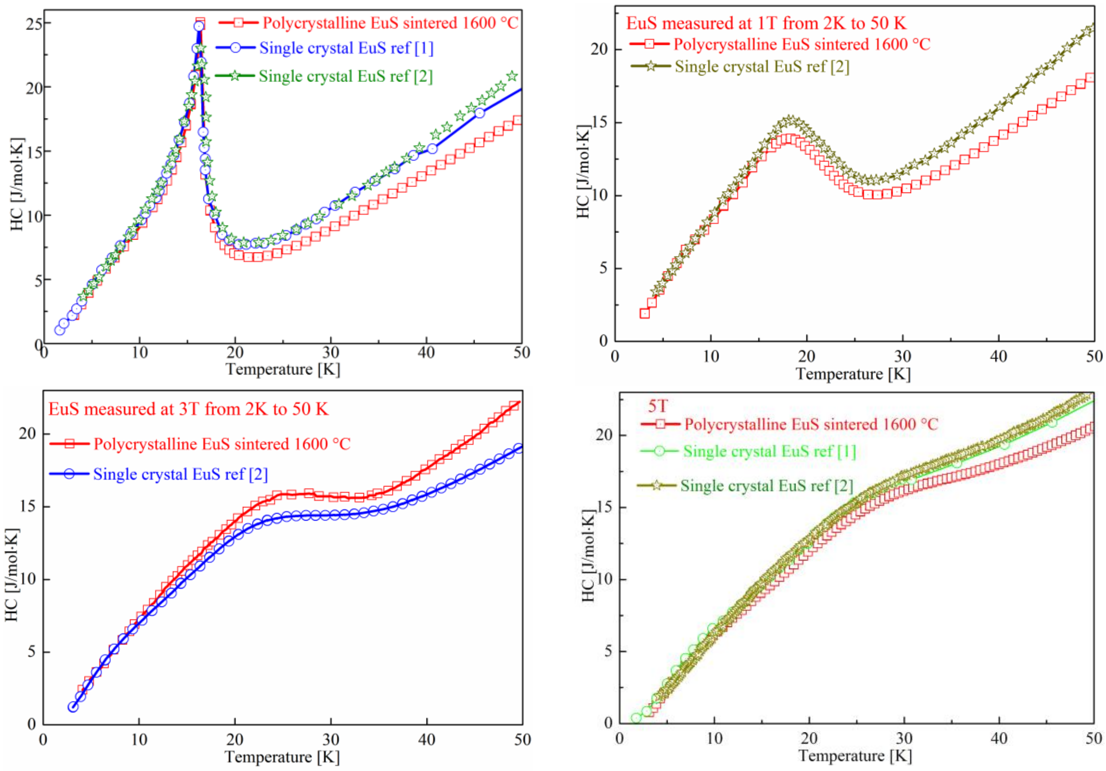

Fig. 3.30 Comparison of heat capacity for polycrystalline and single crystal EuS under zero field (a); 1T (b); 3 T (c); and 5 T (d);

3.6 Conclusions

Influences of particle size and specific surface area of Eu_2O_3 powders on the synthesis of EuS were investigated. High sulfurization temperature (750 or 800 °C) and small grain size are necessary for preparation of EuS. Larger specific surface area of Eu_2O_3 is better for fabrication of Eu_3S_4 at low temperature of 500 °C for longer than 0.5 hr. The shape of synthetic EuS is dependent with that of smaller spherical Eu_2O_3 but the morphology of the Eu_2O_3 nanowires was destroyed at high sulfurization temperature. The specific surface area of the sulfurization product lessened as the sulfurization temperature increased, accompanying with phase transformation of

Eu_3S_4-to-EuS. According to thermodynamic analysis, CS_2-gas sulfurization is more effective than that of H_2S-gas sulfurization due to the formation of unstable EuS_2 phase.

In the evaluation of the effect of heat treatment on the phase transformation from Eu_3S_4 to EuS at a fixed heat treatment time of 1 hr, it was found that heat treatment at 973 K under CS_2/Ar atmosphere and at 873 K under vacuum yielded single-phase EuS. Heat treatment of Eu_3S_4 powder generated a small amount of Eu_2O_2S owing to the impurity oxygen in Eu_3S_4 powder. When heat treatment was performed at high temperatures in the CS_2/Ar atmosphere, the formation of Eu_2O_2S could be inhibited.

Modifying the characters of Eu_2O_3 is an effective step for the preparation of EuS. Large maximum magnetic entropy change of sintered EuS indicated its excellent refrigeration performance and thus it is possible to be employed as magnetic refrigerant material for liquefaction of hydrogen.

A sintered compact of the ferromagnetic semiconductor EuS that had relative density larger than 95% was synthesized. MCE is studied in the vicinity of its ordering temperature and shown to be close to that of single crystal. S - T diagram of sintered EuS was obtained. These results indicate that sintered EuS has excellent ability as a magnetic refrigerant for hydrogen liquefaction.

Chapter 4 Synthesis and sintering of samarium rich SmS_x and its electrical property

4.1 Introduction

Rare earth sulfides were studied as high temperature thermoelectric materials, for their high thermoelectric performances, high melting point, and self-doping ability [80, 118, 119]. Samarium monosulfide SmS at 17.6 wt% sulfur is a semiconductor material with *n*-type conductivity, crystal lattice of the NaCl type, and a high melting temperature (~2300°C)[120]. Characteristic features of the SmS energy-band structure include the presence of 4*f* levels of samarium located at Ef = 0.23 eV below the conduction-band bottom and acting as donors[120]. This energy-band structure not only decided the pressure induced discontinuous semiconductor-metal transition due to 4f-5d electron delocalization, but also caused the temperature induced thermal electromotive force and phase transformation by a conduction-electron concentration gradient[72].

Similar with preparation of other binary[121, 122] and ternary sesquisulfide, polycrystalline SmS powders were also prepared by the reaction of H_2S with samarium bis(trimethylsilyl)amide in tetrahydrofuran (THF) at 10^{-2} torr [123], however, volatile and toxic H_2S is difficult to handle. Traditionally, single crystal SmS with respective compositions was synthesized from metal samarium and sulfur powder by heating, annealing, cold forming, and atmospheric pressure sintering in a sealed silica ampoule tube. However, this method takes long period and composition control of SmS is estimated to be difficult owing to the large difference of vapor pressure between samarium and sulfur.

Most methods employed metallic Sm powders as Sm source for the fabrication of SmS. Compared with metal Sm powder; samarium hydride (SmH_3) powders were used to replace Sm powders because SmH_3 powders are easier to storage and cheaper than Sm powders. Moreover, the advantage of SmH_3 is the generation of H_2 which can avoid or resist the oxidation of SmS at a certain degree.

Polycrystalline SmS has a thermoelectric figure of merit ZT ~0.9 with the optimal composition $SmS_{0.96}$[124]. If we assume the Carnot efficiency to be 50%, thermoelectric materials with ZT=0.89 enable thermoelectric generation with a maximum theoretical generating efficiency of 10%. According to the phase diagram of samarium and sulfur [125], solid solution range of single SmS phase is obtained just in the narrow composition part. The thermoelectric properties of SmS depend on the actual composition.

In this study, non-stoichiometric SmS_x ($0.55 \le x \le 1.2$) with different target composition was prepared from the direct reaction between of samarium sesquisulfide (Sm_2S_3) and SmH_3 to reaffirm the composition dependency of thermoelectric properties. Furthermore, to avoid contamination from the encapsulated ampoule, a BN crucible was employed as the reaction container under vacuum because of high activity of samarium after the release of hydrogen. The reaction temperature is at 1273K which is slightly lower than conventional research. Further, the synthetic powder was sintered with a pulsed electric current sintering device. Electric transport properties of synthetic SmS_x ($0.55 \le x \le 1.07$) were investigated in detail.

4.2 Experimental procedure

4.2.1 Synthesis of SmS_x powders

Both Sm_2S_3 and SmH_3 powders from Kojundo Chemical Laboratory Co., LTD were employed. Compared with synthetic Sm_2S_3 by CS_2-gas sulfurization of commercial or synthesized Sm_2O_3 by co-precipitation, commercial Sm_2S_3 with large vapor pressure sulfur was employed, which has little impurity carbon. SmH_3 and Sm_2S_3 were weighed in molar ratio of M (M= 0.5 for $SmS_{1.2}$, 0.8 for $SmS_{1.07}$, 1 for $SmS_{1.0}$, 1.11 for $SmS_{0.96}$, 1.5 for $SmS_{0.86}$, 1.8 for $SmS_{0.79}$, 2 for $SmS_{0.75}$, 2.5 for $SmS_{0.67}$, 3 for $SmS_{0.60}$, and 3.5 for $SmS_{0.55}$). These powders were mixed under vacuum glove box to prevent the oxidation. The mixtures were put on BN crucibles and heated at 1273 K for 3 hr under a vacuum of $< 1.2 * 10^{-3}$ Pa. Honeycomb Ti foils was placed on the top and one side of BN boat to avoid oxidation. Then the product was milled using a ball mill under vacuum.

The synthetic powders mixed with 10% Si (internal standard substance, purity Company,) were analyzed with X-ray diffraction (XRD, Model Rint-Ultima+, Rigaku Corp., Tokyo, Japan) with monochromatic Cu Kα radiation at 40 kV and 20 mA to check phase compositions. Cell parameters of synthetic powders were measured at the scan step of 1.0×10^{-3} degree for 2s.

4.2.2 Sintering of SmS_x compacts

The synthetic SmS_x powders (1.2 gram) were mounted in a graphite die of 10.5 mm diameter and consolidated by a pulse electric current sintering (SPS-511S, Sumitomo Coal Mining Co.). The chamber of apparatus was pumped down to 7.0 * 10^{-3} Pa. The sintering was performed at 1373K-1673K for 1 hr under the applied pressure of 50 MPa. Microstructures of SmS_x compacts were examined with a scanning electron microscopy (SEM, JSM-5310LV, JEOL Ltd. Tokyo, Japan) to reveal the microstructure and compactness. The chemical compositions of the synthetic SmS_x were determined by ICP emission spectrometry method (Thermo Fisher SCIENTIFIC iCAP6300DUO) for Sm content and infrared absorption technique (LECO CS844) for sulfur content.

4.2.3 Electrical properties of SmS_x compacts

The thermoelectric transport properties such as Seebeck coefficient and electrical resistivity of the sintered compacts were simultaneously measured under a He atmosphere in the temperature range of 300 - 623 K with a temperature differential method and a four-probe method, respectively (ZEM-2). The typical bars used for these measurements had dimensions of 3mm*3mm*5 mm. The power factor was calculated from the earlier of the electrical resistivity and Seebeck coefficient. And based on the former research result of thermal conductivity of SmS, the ZT values were calculated and compared with former results prepared by different method.

4.3 Experimental results

4.3.1 Synthesis of SmS_x powders

Figure 4.1 shows XRD patterns of synthetics from the mixture of Sm_2S_3 and SmH_3 reacted at 1000°C for 3h. There are two main reactions to produce Sm_3S_4 and SmS. When the ratio of Sm_2S_3 to SmH_3 is 0.5 or 0.8, there are not enough Sm atoms to reduce Sm^{3+} of Sm_2S_3 to Sm^{2+} of SmS. So mix-valence compound Sm_3S_4 phase (PFD card: 01-071-0433) is the main product. The prerequisite to fabricate pure SmS (PFD card: 03-065-5955) is the ratio of Sm_2S_3 and SmH_3 above 1. Following with the increase of SmH_3 content, the surplus Sm atoms have self-doped in SmS crystal. Moreover, some Sm atoms replace S atoms in the SmS crystal[72]. In addition, the characteristic peak of rich samarium metal was not identified even the content of metal samarium in the target above 60%. However, the peak position of synthetic SmS_x is smaller than that of reported semiconductor SmS (30°) or metallic SmS (31°) [126]

and has a trend to low angle following the increase of Sm content. The peaks shift to small angle behavior suggested the large and increase of lattice parameter of SmS following the rising of the ratio of Sm_2S_3 and SmH_3.

The behavior of the lattice parameter of SmS_x with samarium content was shown in Fig. 4.2. When the ratio of starting material is less than 1, reaction product is the mixture of Sm_3S_4 (theory lattice parameter of 8.556 Å) and semiconductor SmS (theory lattice parameter of 5.97 Å). The variation of lattice parameter of synthetic is connected with the difference of the diameter of Sm^{2+} (ionic radii of 1.14 Å) and Sm^{3+} (ionic radii of 0.96 Å). Lattice parameters of synthetic SmS showed a wavy variation following the increase of Sm content. The lattice parameter of SmS is also dependent on the temperature[127], which can influence the value fluctuation of Sm atoms between bivalent and trivalent. When Sm content increased to 53.8%, the solved Sm atom in the SmS crystal expanded lattice parameter to 5.99 Å, which has the same effect and value with the temperature dependence[127]. This value is larger than theory lattice parameter of semiconductor SmS. When Sm atoms were melting in the lattice of generated SmS, Sm atoms may substitute in the position of S atoms[128]. After the substitution, atomic radius of Sm atom is much larger than that of S atom. On the other hand, mutual repulsion between Sm atoms and adjacent Sm atoms becomes large. Both cases may cause lattice expansion.

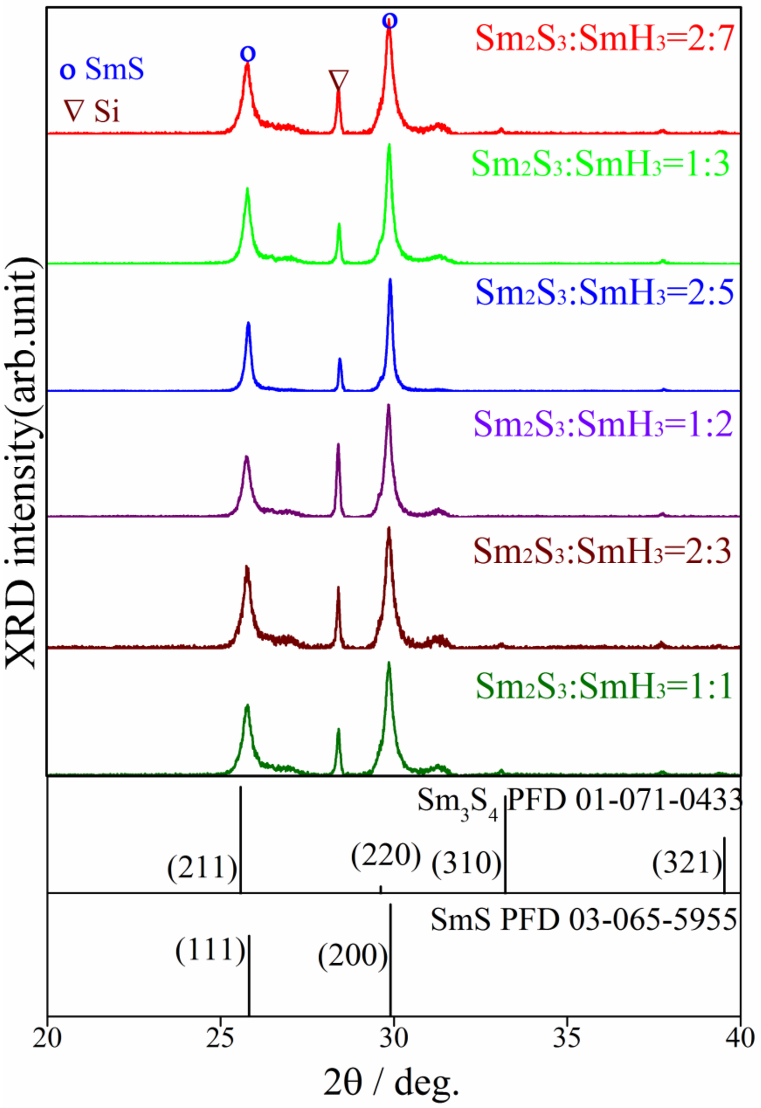

Fig. 4.1 XRD of synthetic SmS by annealing at 1273 K for 3 hr

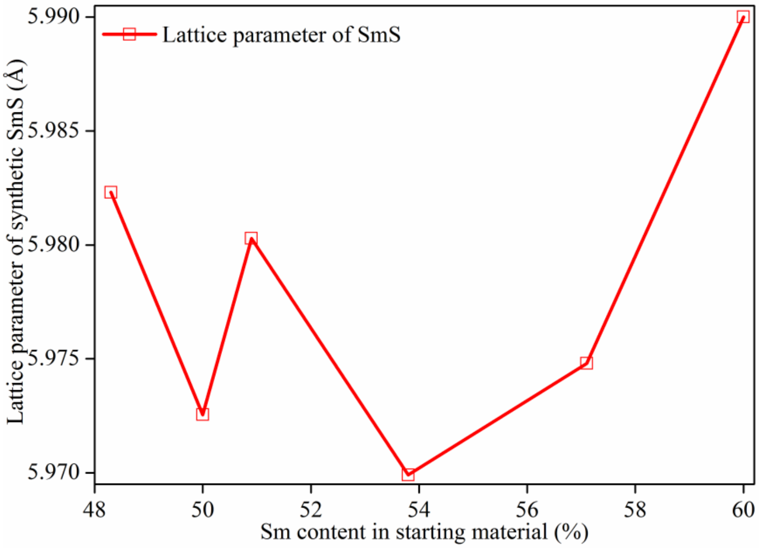

Fig. 4.2 Lattice parameters of synthetic SmS_x

Table 4.1 lists the nominal and actual compositions of synthetic SmS_x. As can be seen from the Table 4.1, when the ratio of starting material is 1, the XRD result of synthesized $SmS_{1.0}$ is single SmS phase, but it presents some trace amounts of sulfur enrichment in the actual composition. The actual synthetic SmS still cannot form Sm enrichment as the ratio of raw materials increased from 1.11 to 1.8. On the other hand, there exists samarium loss during the reaction process. This caused actual composition of SmS_x became irregular when the ratio of Sm_2S_3 and SmH_3 is above 2. However, this does not affect the preparation of high samarium enrichment SmS_x and investigation electrical transport properties of SmS_x. When the ratio of starting material is 2, the actual content of Sm in the synthetic SmS reached 53.9% (another form: $Sm_{1.16}S$). This actual composition has higher Sm content than that reported normal composition for $Sm_{1.07}S$ [128], which composition is based on the calculation that one sulfur atom was replaced by Sm atom in the SmS unit cell. This result suggested that when the ratio of raw materials is more than 2, more than one sulfur atom is possibly substituted to Sm sites in the unit cell of SmS.

Table 4.1 Nominal and actual compositions of synthetic SmS_x

Nominal composition of SmS				Actual composition of SmS		
M	at%Sm	at%S	SmS_x	at%Sm	at%S	SmS_x
1 : 1	50	50	1	49.8	50.2	1.01
1 : 1.11	50.9	49.1	0.96	49.9	50.1	1.00
1:1.5	53.8	46.2	0.86	50.1	49.9	1.00
1:1.8	55.9	44.1	0.79	50.1	49.9	1.00
1:2.0	57.1	42.9	0.75	53.9	46.1	0.86
1:3.0	62.5	37.5	0.60	52.3	47.7	0.91
1 : 3.5	64.7	35.3	0.55	52.1	47.9	0.92

Figure 4.3 shows typical SEM micrographs of synthetic SmS_x powders at 1273 K for 3 hr. The synthetic SmS_x powder has large particle and reunited together because solid phase sintering happens. The added Sm content has no influence on the particle size of synthetic SmS_x.

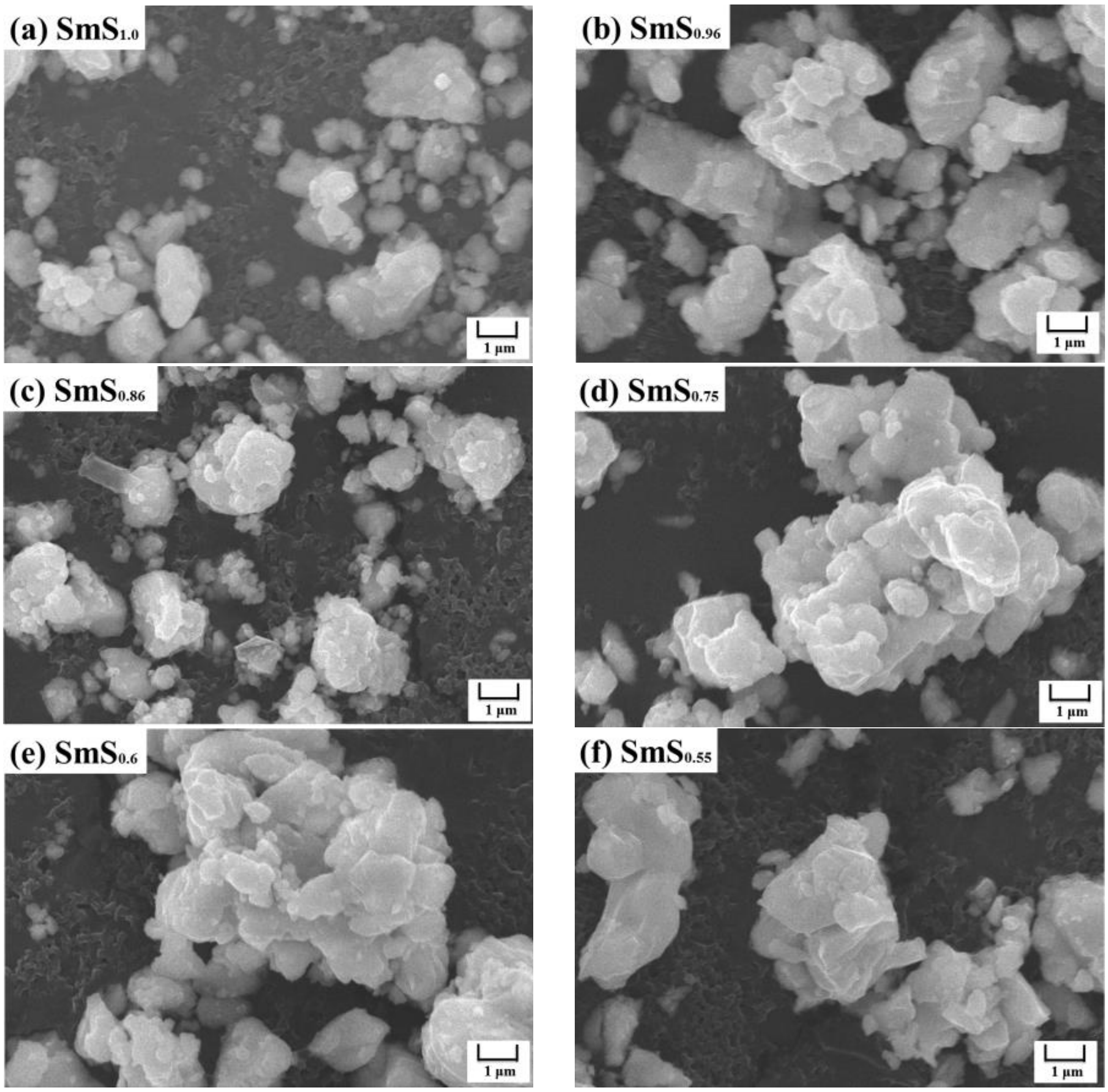

Fig. 4.3 SEM micrographs of synthetic SmS_x powder

Reaction process of the formation of SmS_x was analyzed by the thermodynamic data as shown in Fig. 4.4. There is no thermodynamic data for SmH_3, so the standard free energy change for the thermal decomposition reaction of SmH_3 in equation (1) cannot be calculated. However, thermodynamic data of LaH_2, CeH_2 and PrH_2 show the decomposition reaction of the Gibbs free energy change from positive to negative following with increasing temperature and atomic number. According to the variation of vacuum degree during the experiment, the decomposition of SmH_3 began at about 773K and completed at 1073K. The obtained Sm with higher activity can react with Sm_2S_3 to fabricate SmS as shown in the equation (3).

In this study, maintaining a high vacuum was very important throughout the process of the reaction. The oxidation reaction of metal samarium proceeded to be easier in the way of equation (4). The standard free energy change is negative, so this reaction is easy to advance the right in any of the temperature. Also, the reaction between the product of Sm_2O_3 in equation (4) Sm_2O_3 and starting material of Sm_2S_3 is believed to generate Sm_2O_2S as shown in the equation (5). The weak peak of Sm_2O_2S was easier to be occurred when the vacuum is not well. According to the standard free energy of the formation of Sm_2O_2S, equation (5) proceeded to be easy. If metal Sm was employed as Sm source for the preparation of SmS, Sm_2O_3 layer on the surface of metal Sm easily led to trace Sm_2O_2S in the final product [129]. However, the hydrogen gas from the decomposition of SmH_3 not only can avoid the oxidation of metal samarium and the formation of Sm_2O_2S, but also can reduce trivalent Sm.

$$SmH_3(s) \rightarrow Sm(s)+3/2H_2(s) \qquad (1)$$

$$Sm(s) \rightarrow Sm(l) \qquad (2)$$

$$Sm_2S_3(s)+Sm(l) \rightarrow 3SmS(s) \qquad (3)$$

$$2Sm(l)+3/2O_2(g) \rightarrow Sm_2O_3(s) \qquad (4)$$

$$1/2Sm_2S_3(s)+Sm_2O_3(s) \rightarrow 3/2Sm_2O_2S(s) \qquad (5)$$

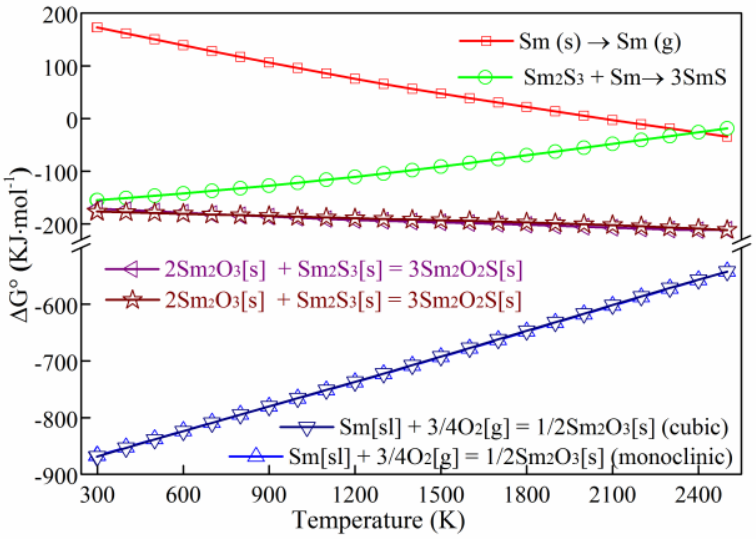

Fig. 4.4 Gibbs free energy analysis of reaction process

4.3.2 Sintering of SmS_x compacts

Figure 4.5 showed XRD results of the sintered SmS_x compacts from the annealed powder at 1373 K for 1 hr by SPS. Linear shrinkage curve of SmS_x compact suggested shrinkage of SmS_x started from 973 K and finished at about 1373 K. It is reasonable for the melting point of 2353 K. So, SmS_x was obtained only at 1373 K. Moreover, there is non-sintered at 1273K. A crack was observed in the sintered body with increasing the sintering temperature to 1473K and sintered SmS_x samples are easy to be cracked for high sintering temperature (above 1473 K). Compared with the results in Fig. 4.2, the lattice constant of SmS_x has no change before and after sintering. Finally, target composition of samarium rich samples $SmS_{1.0}$, $SmS_{0.857}$, and $SmS_{0.667}$ were conducted to evaluate the cross-sectional structure observation and thermoelectric properties.

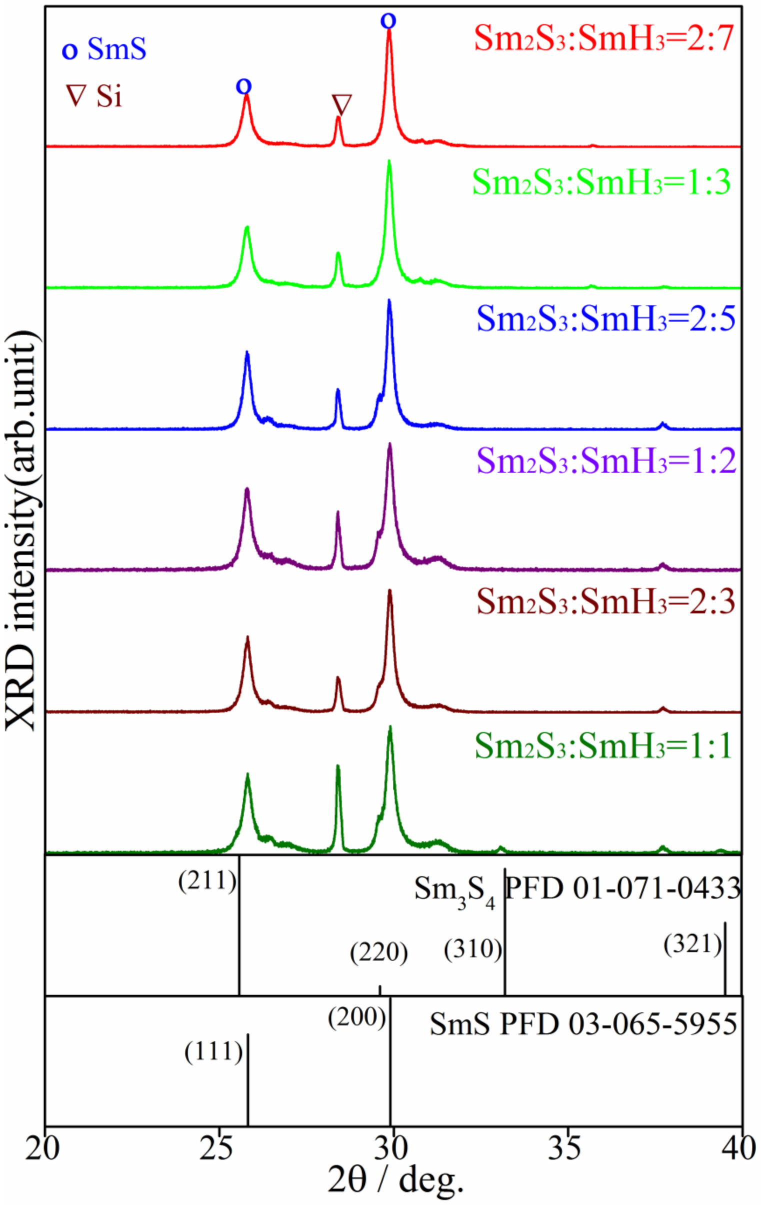

Fig. 4.5 XRD of SmS_x sintered at 1373 K for 1 hr

Figure 4.6 showed SEM image of the sintered SmS_x for the cross section of fracture surface. The sintered SmS_x is entirely homogeneous and there is no obviously preferred orientation. In addition, the particle size of the SmS_x grain becomes larger as samarium content increases. On the other hand, the brittle fracture is within the grain boundary and the existence of cleavage plane can explain the crack of sintered SmS_x.

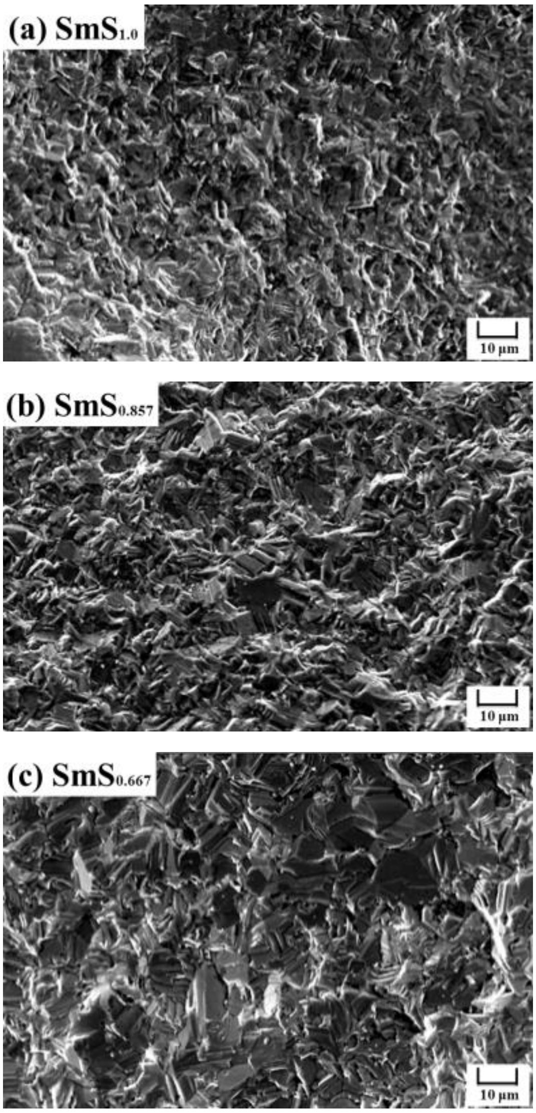

Fig. 4.6 SEM micrograph of SmS_x compacts on the fracture surface

4.3.3 Electrical transport properties of SmS_x compacts

Figure 4.7 shows electrical resistivity ρ as a function of temperature for selected SmS_x compacts. The ρ value of SmS_x ($0.86 \leq x \leq 1.07$) decreases as temperature increase, indicating it is semiconductor. The ρ value of SmS_x ($0.86 \leq x \leq 1.07$) show similar temperature dependence and the values are close to each other, indicating that electrical resistivity of SmS_x does not have larger variation before Sm content reach the saturation in the solid solution. The electrical resistivities were dramatically reduced as the Sm content increasing to 57.2 %, but slightly increased as reaction ratio increased to 3.5. In addition, electrical resistivity of SmS_x ($0.55 \le x \le 0.75$) first increased and then decreased. This should be attributed to the surplus of Sm. The residual Sm randomly distributed in the SmS matrix, which lead a markedly reduced electrical resistivity and the metallic behavior from 300 K to 450 K.

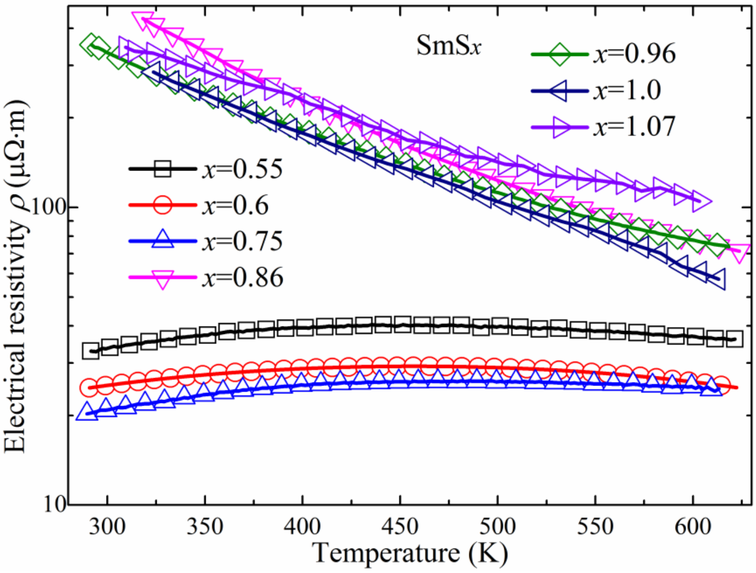

Fig. 4.7 Electrical conductivity σ for selected SmS_x compacts

Temperature dependent Seebeck coefficients of SmS_x ($0.55 \le x \le 1.07$) compounds are plotted in Fig. 8. The Seebeck coefficient of SmS_x ($0.55 \le x \le 1.07$) is negative indicating that it is n-type semiconductor, which increased as the temperature rises. The magnitude of the absolute Seebeck coefficients values is distributed between 170 and 280 $\mu V \cdot K^{-1}$ and increases as samarium-rich content added in the target composition. The Seebeck coefficient of SmS_x ($0.67 \le x \le 1.07$) decreased with increasing temperature while Seebeck coefficient of SmS_x ($0.55 \le x \le 0.75$) showed weak temperature dependence. Seebeck coefficient first increased as Sm ratio increasing, saturate at $SmS_{0.67}$, then decreased as Sm ratio increasing (except the abnormal $SmS_{0.75}$). The abnormal behavior of $SmS_{0.75}$ should be attributed the actual composition deviate the nominal value too much, as also indicated by electrical resistivity.

Compared with chemical composition analysis of synthesized SmS_x as listed in Table 1, the actual chemical composition for the synthesized SmS_x ($0.86 \le x \le 1.07$) was near stoichiometric and Seebeck coefficients of SmS_x ($0.86 \le x \le 1.07$) present totally the increasing trend with the rising of temperature. The surplus Sm atoms which randomly distributed in the SmS_x ($0.55 \leq x \leq 0.75$) matrix occurred valence transitions and generated electrons. Due to the existences of these generated electrons, the variation of Seebeck coefficient show zigzag curves in Fig. 4.8.

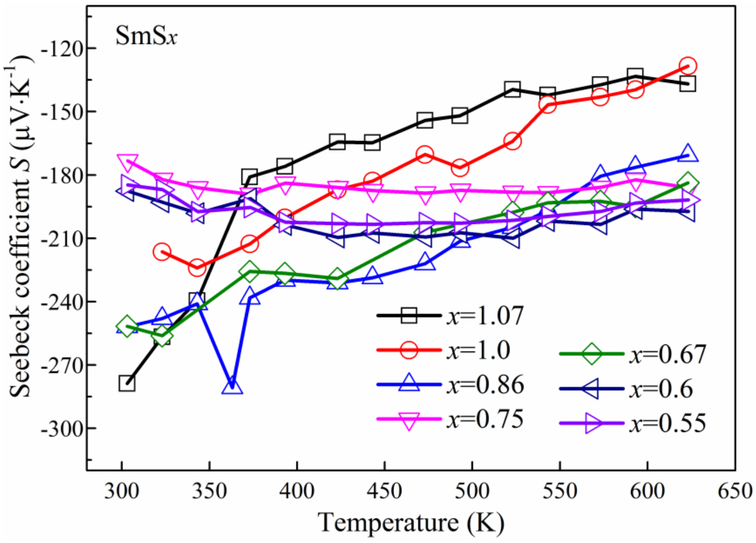

Fig. 4.8 Temperature dependent seebeck coefficients of selected SmS_x compounds

Figure 9 shows power factor of synthetic SmS_x ($0.55 \leq x \leq 1.07$). In the whole, power factor of synthetic SmS_x increased with the Sm content. The abnormal behavior of $SmS_{0.96}$ should be attributed the actual composition fluctuate. Power factor of synthetic $SmS_{0.55}$, $SmS_{0.6}$ and $SmS_{0.67}$ were significantly increased, however, there is no obvious trend that can be observed as Sm content increasing to 64.7 %, suggesting power factor is sensitive to Sm ratio when reaction ratio is above 2. The optimized power factor was found to be 1500 $\mu W \cdot K^{-2} \cdot m^{-1}$ for $SmS_{0.60}$ and $SmS_{0.75}$ between 323 ~ 623 K. This value is comparable to that of reported power factor of composition of $SmS_{0.965}$ (1400 $\mu W \cdot K^{-2} \cdot m^{-1}$ at 1000 K).

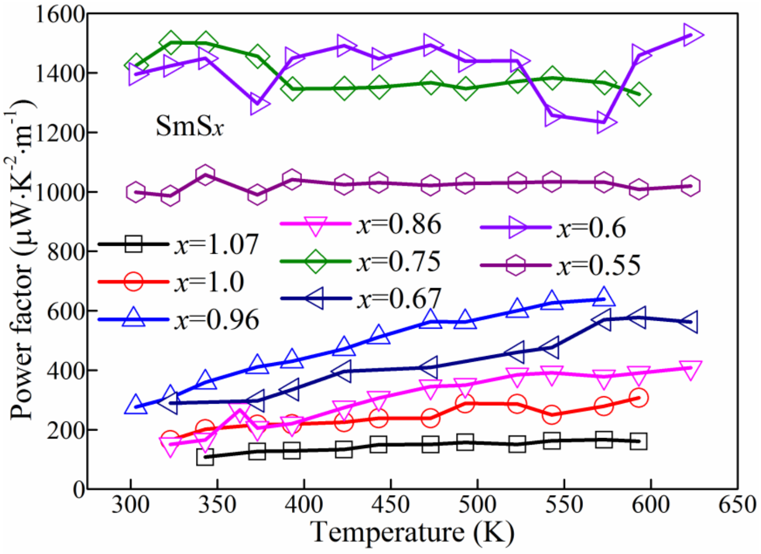

Fig. 4.9 Power factor of SmS_x ($0.55 \leq x \leq 1.07$) compacts

4.4 Conclusions

The stoichiometry Sm_3S_4 has been generated when the content of samarium in starting material was less than 50 %. Semiconductor SmS is generated after annealing and sintering. Since the shrinkage was completed around 1400 K according to the shrinkage curve, sintering of SmS was carried out at 1373 K to obtain an uncrack sintered compact. The Seebeck coefficient of SmS_x ($0.67 \leq x \leq 1.07$) lessens with the rises of temperature and Sm content. The electrical resistivity of $SmS_{0.75}$ had a clearly reduction following the increase of SmH_3 content. Power factor of the obtained samples was about the same level as those in the previous reports at 323 ~ 623 K.

Chapter 5 Conclusions

Yb_2O_3 powders with different characters were employed to research the influence of particle size and specific surface area on the synthesis of Yb_2S_3. The main conclusions are as follows: (1) High sulfurization temperature (1000 °C) and small particle size are necessary for preparation of single hexagonal ε-Yb_2S_3. Larger specific surface area (50 m^2/g) of Yb_2O_3 is better for fabrication of orthorhombic η-Yb_2S_3 at low temperature of 600 °C for 8 hr. However, single Yb_2S_3 cannot be obtained if specific surface area of Yb_2O_3 is less than 2 m^2/g and particle size is larger than 5 μm. (2) Sulfurization time (0.5 hr) tends to decrease with increasing temperature (1050 °C). CS_2 gas flow rate does not only influence the sulfurization efficiency and products, but also control the impurity content. Particle sizes of synthetic orthorhombic η-Yb_2S_3 and hexagonal ε-Yb_2S_3 are dependent on sulfurization condition and impurity content. (3) Heavy Ln_2O_3 are comparatively difficult to be sulfurized than light Ln_2O_3. To modify characters of Ln_2O_3 is an effective step for preparation of Ln_2S_3.

Hexagonal ε-Yb_2S_3 was synthesized at above 1000°C by sulfurizing its oxide with CS_2 gas. The synthetic Yb_2S_3 is more stable in sulfur-rich atmosphere than argon gas or vacuum at about 1000°C. Yb_2S_3 phase transformed to Yb_3S_4 phase (1000 °C for 3 hr or 1200 °C for 1 hr) or YbS phase (1500 °C for 3 hr) during annealing. Yb_2S_3 had better phase stability below 1400 °C with spark plasma sintering. The phase stability of Yb_2S_3 probably depended on the sulfur vapor pressure.

Single-phase Eu_3S_4 could be obtained via sulfurization of Eu_2O_3 using CS_2 gas at 773 K, independent of the sulfurization time. Single-phase EuS was also obtained for sulfurization temperature of 1073 K or higher, independent of the sulfurization time. Single-phase EuS could be obtained at sulfurization temperatures of 973 or 1073 K when the corresponding sulfurization times were 8 and 3 hr, respectively. Although the specific surface area of the product decreased as the sulfurization temperature increased, the decrease in the specific surface area was minimal, accompanied by cubic expansion, when the phase transformation from Eu_3S_4 to EuS occurred. In the evaluation of the effect of heat treatment on the phase transformation from Eu_3S_4 to EuS at a fixed heat treatment time of 1 hr, it was found that heat treatment at 973 K or higher in a CS_2/Ar atmosphere, at 1073 K or higher in an Ar atmosphere, and at 873 K or higher in a vacuum atmosphere, yielded single-phase EuS. Heat treatment of Eu_3S_4 powder generated a small amount of Eu_2O_2S because of impurity oxygen in the Eu_3S_4 powder and oxygen in the vacuum atmosphere. When heat treatment was performed at high temperatures in the CS_2/Ar atmosphere, the formation of Eu_2O_2S could be inhibited.

The stoichiometry Sm_3S_4 has been generated when the content of samarium in starting material was less than 50%. Semiconductor SmS is generated after annealing and sintering. Since the shrinkage was completed around 1400K according to the shrinkage curve, sintering of SmS was carried out at 1373K to obtain an uncrack sintered compact. The Seebeck coefficient of SmS_x ($0.67<x<1.07$) lessens with the rises of temperature and Sm content. The electrical resistivity of $SmS_{0.75}$ had a clearly reduction following the increase of SmH_3 content. Power factor the obtained samples was about the same level as those in the previous reports at 323 ~ 623K.

References

[1] S. Cotton, Lanthanide and actinide chemistry, John Wiley & Sons, 2013.

[2] P. Dorenbos, Energy of the first $4f^7 \rightarrow 4f^6 5d$ transition of Eu^{2+} in inorganic compounds, J. Lumin., 104 (2003) 239-260.

[3] P. Dorenbos, f→d transition energies of divalent lanthanides in inorganic compounds, J. Phys.: Condens. Matter., 15 (2003) 575-594.

[4] J. Flahaut, Sulfides, selenides and tellurides, Handbook on the Physics and Chemistry of Rare Earths, 4 (1979) 1-88.

[5] S. Roméro, A. Mosset, J.C. Trombe, P. Macaudière, Low-temperature process of the cubic lanthanide sesquisulfides: remarkable stabilization of the γ-Ce_2S_3 phase, J. Mater. Chem., 7 (1997) 1541-1547.

[6] M. Ohta, H. Yuan, S. Hirai, Y. Uemura, K. Shimakage, Preparation of R_2S_3 (R: La, Pr, Nd, Sm) powders by sulfurization of oxide powders using CS_2 gas, J. Alloys Compd., 374 (2004) 112-115.

[7] S.H. Han, K.A. Gschneidner, B.J. Beaudry, Preparation of the metastable high pressure γ-R_2S_3 phase (R:Er, Tm, Yb and Lu) by mechanical milling, J. Alloys Compd., 181 (1992) 463-468.

[8] S.H. Han, K.A. Gschneidner, B.J. Beaudry, Preparation of a metastable high temperature phase (γ-Dy_2S_3) and a metastable high pressure phase (γ-Y_2S_3) by mechanical alloying and mechanical milling, Scripta Metallurgica et Materiala., 25 (1991) 295-298.

[9] X. Luo, M. Zhang, L. Ma, Y. Peng, Preparation and stabilization of γ-La_2S_3 at low temperature, J. Rare Earths, 29 (2011) 313-316.

[10] J. KoŃCzyk, P. Demchenko, O. Bodak, G. Demchenko, B. Marciniak, W. Prochwicz, L. Muratova, Crystal structure of δ-Tm_2S_3, Chem. Met. Alloys., 1 (2008) 38-42.

[11] A.R. Landa-Canovas, U. Amador, L.C. Otero-Díaz, Crystal structure and microstructure of δ-Er_2S_3, J. Alloys Compd., 323 (2001) 91-96.

[12] N.R. Akhmedova, O.M. Aliev, I.B. Bakhtiyarly, Interaction in the Yb_2S_3-In_2S_3 system, Russ. J. Inorg. Chem., 51 (2006) 478-483.

[13] G.M. Kuz'micheva, I.A. Matveenko, Crystal Chemistry of Rare-Earth Chalcogenides, Russ. J. Coord. Chem. , 27 (2001) 73-84.

[14] E. Bucher, K. Andres, F.J. Di Salvo, J.P. Maita, A.C. Gossard, A.S. Cooper, G.W. Hull Jr, Magnetic and some thermal properties of chalcogenides of Pr and Tm and a few other rare earths, Phys. Rev. B, 11 (1975) 500.

[15] S. Hirai, E. Sumita, K. Shimakage, Y. Uemura, T. Nishimura, M. Mitomo, Synthesis and sintering of cerium (II) monosulfide, J. Am. Ceram. Soc., 87 (2004) 23-28.

[16] M. Guittard, J. Flahaut, Synthesis of lanthanide and actinide compounds, Springer, 1991, Vol:2, pp. 321-352.

[17] G.V. Samsonov, Crystal-chemical properties of sulfides of the rare-earth metals

and actinides, Sov. Powder Metall. Metal Ceram., 1 (1962) 237-243.

[18] J. Lock, The Magnetic Susceptibilities of Lanthanum, Cerium, Praseodymium, Neodymium and Samarium, from 1.5 K to 300 K, Proc. Phys. Soc. London, Sect. B, 70 (1957) 566.

[19] S. Hirai, K. Shimakage, Y. Saitou, T. Nishimura, Y. Uemura, M. Mitomo, L. Brewer, Synthesis and sintering of cerium (III) sulfide powders, J. Am. Ceram. Soc., 81 (1998) 145-151.

[20] K.A. Gschneidner, Preparation and processing of rare earth chalcogenides, J. Mater. Eng. Perform., 7 (1998) 656-660.

[21] H. Yuan, T. Kuzuya, M. Ohta, S. Hirai, Low-temperature formation of cubic Th_3P_4-type gadolinium and holmium sesquisulfide, J. MMIJ, 126 (2010) 450-455.

[22] M. Ohta, S. Hirai, T. Kuzuya, Preparation and Thermoelectric Properties of $LaGd_{1+x}S_3$ and $SmGd_{1+x}S_3$, J. Electron. Mater., 40 (2011) 537-542.

[23] Y. Haibin, M. Ohta, S. Hirai, T. Nishimura, K. Shimakage, Preparation of terbium sesquisulfide and holmium sesquisulfide by sulfurization of their oxide powders using CS_2 gas, J. Rare Earths, 22 (2004) 759-762.

[24] M. Ohta, S. Hirai, H. Kato, V.V. Sokolov, V.V. Bakovets, Thermal decomposition of NH_4SCN for preparation of Ln_2S_3 (Ln ¼ La and Gd) by Sulfurization, Mater. Trans., 50(2009) 1885-1889.

[25] R. Mauricot, J. Dexpert-Ghys, M. Evain, Photoluminescence of the undoped γ-Ln_2S_3 and doped γ-[Na]Ln_2S_3 rare earth sulfides (Ln= La, Ce), J. Lumin., 69 (1996) 41-48.

[26] V. Jarý, L. Havlák, J. Bárta, M. Buryi, E. Mihóková, M. Rejman, V. Laguta, M. Nikl, Optical, structural and paramagnetic properties of Eu-doped ternary sulfides $ALnS_2$ (A= Na, K, Rb; Ln= La, Gd, Lu, Y), Mater., 8 (2015) 6978-6998.

[27] T. Chopin, H. Guichon, O. Touret, Rare earth sesquisulfide compositions comprising alkali/alkaline earth metal values, US Patent 5,348,581, 1994.

[28] T. Chopin, D. Dupuis, Rare earth metal sulfide pigment compositions, US Patent 5,401,309, 1995.

[29] P. Macaudiere, J. Morros, J.-M. Tourre, A. Tressaud, Rare earth metal sulfide pigments comprising fluorine values, US Patent 5,501,733, 1996.

[30] P. Macaudiere, Very finely divided rare earth sulfide colorant compositions, US Patent 5,755,868, 1998.

[31] T Chopin, P. Macaudiere, Alkaline-earth metal-, copper- and optionally titanium-based silicates, blue or violet pigments based on these silicates, process for their preparation and their use, US Patent 5,888,291, 1999.

[32] E. Urones-Garrote, A. Gómez-Herrero, A.R. Landa-Cánovas, F. Fernández-Martınez, L.C. Otero-Dıaz, Synthesis and characterization of possible pigments in the Mg-Yb-S system, J. Alloys Compd., 374 (2004) 197-201.

[33] M.D. Hernandez-Alonso, A. Gomez-Herrero, A.R. Landa-Canovas, A. Duran, F. Fernández-Martínez, L.C. Otero-Díaz, New ecological pigments in the Ca-Yb-S system, J. Alloys Compd., 323 (2001) 297-302.

[34] G. Chen, Z. Zhu, H. Liu, Y. Wu, C. Zhu, Preparation of SiO_2 coated Ce_2S_3 red pigment with improved thermal stability, J. Rare Earths, 31 (2013) 891-896.

[35] H. Yuan, J. Zhang, R. Yu, Q. Su, Preparation of ternary rare earth sulfide $La_xCe_{2-x}S_3$ as red pigment, J. Rare Earths, 31 (2013) 327-330.

[36] J.M. Tomczak, L.V. Pourovskii, L. Vaugier, A. Georges, S. Biermann, Rare-earth vs. heavy metal pigments and their colors from first principles, Proc. Natl. Acad. Sci., 110 (2013) 904-907.

[37] E.D. Eastman, L. Brewer, L.A. Bromley, P.W. Gilles, N.I. Lofgren, Preparation and tests of refractory sulfide crucibles, J. Am. Chem. Soc., 34 (1951) 128-136.

[38] E.D. Eastman, L. Brewer, L.A. Bromley, P.W. Gilles, N.L. Lofgren, Preparation and Properties of Refractory Cerium Sulfides1a, J. Am. Chem. Soc., 72 (1950) 2248-2250.

[39] C. Wood, Materials for thermoelectric energy conversion, Rep. Prog. Phys., 51 (1988) 459.

[40] T. Takeshita, K.A. Gschneidner Jr, B.J. Beaudry, Preparation of γ-LaS_y ($1.33 < y < 1.50$) alloys by the pressure‐assisted reaction sintering method and their thermoelectric properties, J. Appl. Phys., 57 (1985) 4633-4637.

[41] G.G. Gadzhiev, S.M. Ismailov, M.M. Khamidov, K.K. Abdullaev, V.V. Sokolov, Thermophysical properties of sulfides of lanthanum, praseodymium, gadolinium, and dysprosium, High Temp., 38 (2000) 875-879.

[42] S.M. Taher, J.B. Gruber, Thermoelectric efficiency of rare earth sesquisulfides, Mater. Res. Bull., 16 (1981) 1407-1412.

[43] M. Ohta, S. Hirai, Thermoelectric Properties of $NdGd_{1+x}S_3$ Prepared by CS_2 Sulfurization, J. Electron. Mater., 38 (2009) 1287-1292.

[44] C.M. Varma, Mixed-valence compounds, Rev. Mod. Phys., 48 (1976) 219.

[45] J.M. Lawrence, P.S. Riseborough, R.D. Parks, Valence fluctuation phenomena, Rep. Prog. Phys., 44 (1981) 1.

[46] A. Jayaraman, V. Narayanamurti, E. Bucher, R.G. Maines, Continuous and discontinuous semiconductor-metal transition in samarium monochalcogenides under pressure, Phys. Rev. Lett., 25 (1970) 1430.

[47] E. Kaldis, P. Wachter, The semiconductor-metal transition of the samarium mono-chalcogenides, Solid State Commun., 11 (1972) 907-912.

[48] B. Batlogg, E. Kaldis, A. Schlegel, P. Wachter, Electronic structure of Sm monochalcogenides, Phys. Rev. B, 14 (1976) 5503.

[49] T. Ito, A. Chainani, H. Kumigashira, T. Takahashi, N.K. Sato, Electronic structure of black SmS. II. Angle-resolved photoemission spectroscopy, Phys. Rev. B, 65 (2002) 155202.

[50] A. Chainani, H. Kumigashira, T. Ito, T. Sato, T. Takahashi, T. Yokoya, T. Higuchi, T. Takeuchi, S. Shin, N.K. Sato, Electronic structure of black SmS. I. 4d-4f resonance and angle-integrated valence-band photoemission spectroscopy, Phys. Rev. B, Conden. Matter, 65 (2002) 155201-155201.

[51] P.A. Alekseev, R.V. Chernikov, A.V. Golubkov, K.V. Klementiev, A.P.

Menushenkov, K.S. Nemkovsky, XAFS spectroscopy of the mixed valent $Sm_{1-x}Y_xS$, Nucl. Instrum. Meth. Phys. Res. A, 543 (2005) 205-207.

[52] P.A. Alekseev, J.M. Mignot, E.V. Nefedova, K.S. Nemkovskii, V.N. Lazukov, I.P. Sadikov, A. Ochiai, Nature of the magnetic excitation spectrum in (Sm, Y) S: CEF effects or an exciton?, J. Exper. Theor. Phys. Lett., 79 (2004) 81-84.

[53] V.N. Belomestnykh, E.P. Tesleva, Acoustic, elastic, and anharmonic properties of $Sm_{1-x}R_xS$ solid solutions with trivalent impurities (R= Y, La, Tm), Russ. Phys. J., 55 (2012) 488-494.

[54] A.V. Golubkov, V.A. Didik, V.V. Kaminskii, E.A. Skoryatina, V.P. Usacheva, N.V. Sharenkova, Europium diffusion in SmS, Phys. Solid State, 47 (2005) 1233-1235.

[55] V.A. Didik, V.V. Kaminskiĭ, E.A. Skoryatina, V.P. Usacheva, N.V. Sharenkova, A.V. Golubkov, Nickel diffusion in samarium sulfide, Tech. Phys. Lett., 32 (2006) 555-557.

[56] S.S. Aplesnin, A.M. Khar’kov, Magnetic and dynamic properties of $Sm_xMn_{1-x}S$ solid solutions, Phys. Solid State, 55 (2013) 81-87.

[57] V.C. Srivastava, R. Stevenson, Effect of pressure on magnetic phase transitions of europium chalcogenides: EuO, EuS, and EuSe, Canadian J. Phys., 46 (1968) 2703-2713.

[58] K. Syassen, Ionic monochalcogenides under pressure, Phys. B+C, 139 (1986) 277-283.

[59] N. Benbattouche, G.A. Saunders, H. Bach, The pressure and temperature dependences of the elastic properties of EuS, J. Phys. Chem. Solids, 51 (1990) 181-188.

[60] P.K. Schwob, M. Tachiki, G.E. Everett, Determination of exchange integrals J_1 and J_2 and magnetic surface-anisotropy energy in EuS from standing-spin-wave resonance, Phys. Rev. B, 10 (1974) 165.

[61] R. Tsu, L. Esaki, Luminescence Spectra of Europium Chalcogenides: EuO, EuS, and EuSe, Phys. Rev. Lett., 24 (1970) 455.

[62] G. Güntherodt, Optical properties and electronic structure of europium chalcogenides, Phys. Conden. Matter., 18 (1974) 37-78.

[63] K. Tanaka, N. Tatehata, K. Fujita, K. Hirao, Preparation and Faraday effect of EuS microcrystal-embedded oxide thin films, J. Appl. Phys., 89 (2001) 2213-2219.

[64] Y. Hasegawa, M. Maeda, T. Nakanishi, Y. Doi, Y. Hinatsu, K. Fujita, K. Tanaka, H. Koizumi, K. Fushimi, Effective optical faraday rotations of semiconductor eus nanocrystals with paramagnetic transition-metal ions, J. Am. Chem. Soc., 135 (2013) 2659-2666.

[65] V.L. Moruzzi, D.T. Teaney, Specific heat of EuS, Solid State Commun., 1 (1963) 127-131.

[66] P. Schwob, O. Vogt, The shift of the ferromagnetic curie temperature in EuS by hydrostatic pressure, Phys. Lett. A, 24 (1967) 242-244.

[67] P. Brédy, P. Seyfert, Experimental results on magnetic and thermal properties of europium sulfide relevant to magnetic refrigeration, Cryogenics, 28 (1988) 605-606.

[68] G.V. Lashkarev, L.A. Ivanchenko, Y.B. Paderno, Optical investigation of ytterbium monochalcogenides, Phys. Status Solidi B, 49 (1972) 61-65.

[69] V. Narayanamurti, A. Jayaraman, E. Bucher, Optical absorption in ytterbium monochalcogenides under pressure, Phys. Rev. B, 9 (1974) 2521.

[70] K. Syassen, H. Winzen, H.G. Zimmer, H. Tups, J.M. Leger, Optical response of YbS and YbO at high pressures and the pressure-volume relation of YbS, Phys. Rev. B, 32 (1985) 8246.

[71] B. Batlogg, E. Kaldis, A. Schlegel, G. Von Schulthess, P. Wachter, Optical and electrical properties of the mixed valence compound Sm_3S_4, Solid State Commun., 19 (1976) 673-676.

[72] M.M. Kazanin, V.V. Kaminskii, S.M. Solov'ev, Anomalous thermal electromotive force in samarium monosulfide, Tech. Phys., 45 (2000) 659-661.

[73] P. Jood, M. Ohta, Hierarchical architecturing for layered thermoelectric sulfides and chalcogenides, Mater., 8 (2015) 1124-1149.

[74] N.A. Mancheri, World trade in rare earths, Chinese export restrictions, and implications, Res. Policy, 46 (2015) 262-271.

[75] D.S. Yadav, Electronic and mechanical properties of rare earth monochalcogenides, J. Alloys Compd., 537 (2012) 250-254.

[76] P. Maestro, D. Huguenin, Industrial applications of rare earths: which way for the end of the century, J. Alloys Compd., 225 (1995) 520-528.

[77] G. Chen, Z. Zhu, H. Liu, Y. Wu, C. Zhu, Preparation of SiO_2 coated Ce_2S_3 red pigment with improved thermal stability, J. RARE EARTH., 31 (2013) 891-896.

[78] P.N. Kumta, S.H. Risbud, Rare-earth chalcogenides—an emerging class of optical materials, J. Mater. Sci., 29 (1994) 1135-1158.

[79] Y. Miyazaki, H. Ogawa, T. Kajitani, Preparation and thermoelectric properties of misfit-layered sulfide $[Yb_{1.90}S_2]_{0.62}NbS_2$, Jpn. J. Appl. Phys., 43 (2004) L1202.

[80] H. Yuan, J. Zhang, R. Yu, Q. Su, Synthesis of rare earth sulfides and their UV-vis absorption spectra, J. RARE EARTH., 27 (2009) 308-311.

[81] M. Ohta, S. Hirai, Z. Ma, T. Nishimura, Y. Uemura, K. Shimakage, Phase transformation and microstructures of Ln_2S_3 (Ln= La, Sm) with different impurities content of oxygen and carbon, J. Alloys Compd., 408 (2006) 551-555.

[82] M. Ohta, Y. Haibin, S. Hirai, Y. Yajima, T. Nishimura, K. Shimakage, Thermoelectric properties of Th_3P_4-type rare-earth sulfides Ln_2S_3 (Ln= Gd, Tb) prepared by reaction of their oxides with CS_2 gas, J. Alloys Compd., 451 (2008) 627-631.

[83] M. Ohta, T. Kuzuya, H. Sasaki, T. Kawasaki, S. Hirai, Synthesis of multinary rare-earth sulfides $PrGdS_3$, $NdGdS_3$, and $SmEuGdS_4$, and investigation of their thermoelectric properties, J. Alloys Compd., 484 (2009) 268-272.

[84] M. Ohta, S. Hirai, T. Mori, Y. Yajima, T. Nishimura, K. Shimakage, Effect of non-stoichiometry on thermoelectric properties of Tb_2S_{3-x}, J. Alloys Compd., 418 (2006) 209-212.

[85] M. Ohta, S. Satoh, T. Kuzuya, S. Hirai, M. Kunii, A. Yamamoto, Thermoelectric

properties of $Ti_{1+x}S_2$ prepared by CS_2 sulfurization, Acta Mater., 60 (2012) 7232-7240.

[86] M. Silva, A review of developmental and reproductive toxicity of CS_2 and H_2S generated by the pesticide sodium tetrathiocarbonate, Birth Defects Res. B., 98 (2013) 119-138.

[87] G.M. Kuzmicheva, A.A. Eliseev, Study of Epsilon-Yb_2S_3 Crystalline-Structure, Russ. J. Inorg. Chem., 22 (1977) 897-900.

[88] I.A. Smirnov, Rare-earth semiconductors studies in the soviet union, J. Phys. Colloq., 41 (1980) 143-154.

[89] R. Chevalie, P. Laruelle, J. Flahaut, Crystal structure ytterbium sulfide Yb_3S_4, B. Soc. Fr. Mineral CR., 90 (1967) 564-574.

[90] C.O. Diaz, B.G. Hyde, On the non-stoichiometric ytterbium sulphide phase'Yb_3S_4', Acta Crystallogr., Sect. B: Struct. Sci, 39 (1983) 569-575.

[91] A. Tomas, M. Robert, M. Guittard, Structure du compose $Yb_{0.875}S$ structure of $Yb_{0.875}S$, Mater. Res. Bull., 23 (1988) 507-511.

[92] K.J. Range, H. Drexler, A. Gietl, U. Klement, K.G. Lange, Tm_2S_3-V, a corundum-type modification of thulium sesquisulfide, Acta Crystallogr. Sect. C-Cryst. Struct. Commun., 46 (1990) 487-488.

[93] S.J. Kim, J.W. Anderegg, H.F. Franzen, Structure of a new intermediate $Lu_{2+x}S_3$ phase, J. Less. Common. Met., 157 (1990) 133-138.

[94] C. Felser, Valence instabilities and inhomogeneous mixed valence in some ternary europium compounds, J. Alloys Compd., 262–263 (1997) 87-91.

[95] K.P. Ananth, P.J. Gielisse, T.J. Rockett, Synthesis and characterization of Europium sulfide, Mater. Res. Bull., 9 (1974) 1167-1171.

[96] S. Thongchant, Y. Hasegawa, Y. Wada, S. Yanagida, Liquid-phase synthesis of EuS nanocrystals and their physical properties, J. Phys. Chem. B, 107 (2003) 2193-2196.

[97] T. Nakanishi, M. Maeda, A. Kawashima, S. Kamiya, K. Fushimi, K. Fujita, K. Tanaka, Y. Hasegawa, Novel opto-magnetic silicate glass with semiconductor EuS nanocrystals, J. Alloys Compd., 562 (2013) 123-127.

[98] B.A. Orlowski, E. Guziewicz, B.J. Kowalski, T. Story, S. Mickevičius, A.Y. Sipatov, M. Chernyshova, I.N. Demchenko, N. Barrett, M. Taniguchi, A. Kimura, H. Sato, C.A. Sebenne, J.P. Lacharme, R. Medicherla, W. Drube, Photoemission study of EuS/PbS electronic structure, J. Alloys Compd., 362 (2004) 198-201.

[99] F. Furuuchi, M. Wakeshima, Y. Hinatsu, Magnetic properties and 151Eu Mössbauer effects of mixed valence europium copper sulfide, Eu_2CuS_3, J. Solid State Chem., 177 (2004) 3853-3858.

[100] Mineo Sato, J.S. Gin-ya Adachi, Electrical Properties of Th_3P_4-type Rare Earth Sulfides, $EuLn_2S_4$ (Ln=La-Gd), Chem. Inorg. Mater., 10 (1981) 1610-1616.

[101] S. Somarajan, M.A. Harrison, D.S. Koktysh, W. He, S.A. Hasan, J. H. Park, R.L. Stillwell, E.A. Payzant, J.H. Dickerson, Structural and magnetic analysis of nanocrystalline lead europium sulfide (Pb_xEu_yS), Mater. Chem. Phy., 134 (2012) 1-6.

[102] S. Somarajan, A.J. Krejci, W. He, D.S. Koktysh, J.H. Dickerson, Concentration

dependence of the exchange interaction in lead europium sulfide nanocrystals, Solid State Commun., 152 (2012) 161-164.

[103] D.X. Li, T. Yamamura, S. Nimori, Y. Homma, F. Honda, Y. Haga, D. Aoki, Large reversible magnetocaloric effect in ferromagnetic semiconductor EuS, Solid State Commun., 193 (2014) 6-10.

[104] Y. Zhang, X. Xu, Y. Yang, L. Hou, Z. Ren, X. Li, G. Wilde, Study of the magnetic phase transitions and magnetocaloric effect in Dy_2Cu_2In compound, J. Alloys Compd., 667 (2016) 130-133.

[105] N. Sato, G. Shinohara, A. Kirishima, O. Tochiyama, Sulfurization of rare-earth oxides with CS_2, J. Alloys Compd., 451 (2008) 669-672.

[106] M.W. Shafer, The formation of europium sulfide by the H_2S-Eu_2O_3 reaction at high temperatures, Mater. Res. Bull., 7 (1972) 603-611.

[107] T. Mirkovic, M.A. Hines, P.S. Nair, G.D. Scholes, Single-source precursor route for the synthesis of EuS nanocrystals, Chem. Mater., 17 (2005) 3451-3456.

[108] H. Lin, Q. Luo, W.Y. Tong, C. Jiang, R. Huang, H. Peng, L.C. Zhang, J. Travas-Sejdic, C.G. Duan, Facile preparation of rare-earth semiconductor nanocrystals and tuning of their dimensionalities, RSC Adv., 5 (2015) 86885-86890.

[109] W.L. Boncher, E.A. Görlich, K. Tomala, J.L. Bitter, S.L. Stoll, Valence and magnetic investigations of alkali metal-doped europium sulfide, Chem. Mater., 24 (2012) 4390-4396.

[110] W.L. Boncher, N. Rosa, S. Kar, S.L. Stoll, Europium chalcogenide nanowires by vapor phase conversions, Chem. Mater., 26, (2014) 3144-3150.

[111] L. Li, S. Hirai, H. Yuan, Influences of Yb_2O_3 characters and sulfurization conditions on preparation of Yb_2S_3, J. Alloys Compd., 618 (2015) 742-749.

[112] M. Ohta, S. Hirai, Z. Ma, T. Nishimura, Y. Uemura, K. Shimakage, Phase transformation and microstructures of Ln_2S_3 (Ln= La, Sm) with different impurities content of oxygen and carbon, J. Alloys Compd., 408 (2006) 551-555.

[113] A. Kirishima, Y. Amano, N. Sato, Behavior of fission products in sulfide reprocessing process, J. Nucl. Radiochem. Sci., 12 (2012) 1-4.

[114] A.K. Nobuaki Sato, Separation of lanthanides and actinides by sulfide method, Res. Proc., 57 (2010) 135-140.

[115] A.V. Harihara, H.A. Eick, Vaporization thermodynamics of europium (II) sulfide, High Temp. Sci., 3 (1971) 123-129.

[116] L. Li, S. Hirai, H. Yuan, E. Nakamura, Synthesis of ytterbium sulfides by the sulfurization and heat treatment, Key Eng. Mater., 655 (2015) 224-229.

[117] Z. Mohamed, E. Tka, J. Dhahri, E.K. Hlil, Giant magnetic entropy change in manganese perovskite $La_{0.67}Sr_{0.16}Ca_{0.17}MnO_3$ near room temperature, J. Alloys Compd., 615 (2014) 290-297.

[118] Yuan H.B, Zhang J.H., Yu R.J., Su Q., Preparation and thermoelectric properties of ternary rare earth sulfide γ-$Ce_{3-x}Eu_xS_4$, J. Rare Earths, 2008, 26 (6):817.

[119] Yuan H.B, Zhang J.H., Yu R.J., Su Q., Synthesis of rare earth sulfides and their UV-vis absorption spectra, J. Rare Earths, 2009, 27 (2):308.

[120] Kaminskiĭ V.V., Kazanin M.M., Solov’ev S.M., Sharenkova N.V., Volodin N.M., The effect of electromotive-force generation on electrical properties of thin samarium sulfide films, Semiconductors, 2006, 40(6):651.

[121] Luo X.X, Ma L.B., Xing M.M., Fu Y., Sun M., Tao P., Preparation of γ-Gd_2S_3 via thermolysis of $Gd[S_2CN(C_4H_8)]_3$·phen coordination, J. Rare Earths, 2012, 30(8):802.

[122] Li P.S., Li H.Y., Jie W.Q., Preparation of lanthanum sulfide nanoparticles by thermal decomposition of lanthanum complex, J. Rare Earths, 2011, 29(4):317.

[123] Andreev O.V., Bochkarev M.N., Nekrasova T.V., Protchenko A.V., Preparation of samarimm (ii) sulfide by the reaction of samarium (II) bis [bis (trimethylsilyl) amide] with hydrogen sulfide, Russ. Chem. Bull., 1995, 44 (2):233.

[124] Golubkov A.V., Kazanin M.M., Kaminskii V.V., Sokolov V.V., Solov'ev S.M., Trushnikova L.N., Thermoelectric properties of SmS_x (x= 0.8-1.5), Inorg. Mater., 2003, 39 (12):1251.

[125] Massalski T.B., Okamoto H., Subramanian P.R., Kacprzak L., Binary alloy phase diagrams. vol. 3, ASM International, 1990, (1990) 1485.

[126] Sharenkova N.V., Kaminskii V.V., Golubkov A.V., Vasil’ev L.N., Kamenskaya G.A., The structure of a metallic-phase film produced by mechanical polishing of polycrystalline SmS, Phys. Solid State, 2005, 47 (4):622.

[127] Kaminskii V.V., Sharenkova N.V., Vasil’ev L.N., Solov’ev S.M., Temperature dependence of the SmS lattice parameter, Phys. Solid State, 2005, 47 (2):225.

[128] Egorov V.M., Kaminskii V.V., Romanova M.V., Golubkov A.V., Thermal effects in $Sm_{1+x}S$ in the homogeneity range, Tech. Phys., 2012, 57(7):962.

[129] Kaminskii V.V., Golubkov A.V., Vasil’ev L.N., Defect samarium ions and electromotive-force generation in SmS, Phys. Solid State, 2002, 44 (8):1574.

List of Publications

Journal Paper:

(1) **Li Liang**, Hirai Shinji, Yuan Haibin,“Influences of Yb_2O_3 characters and sulfurization conditions on the preparation of Yb_2S_3”, Journal of Alloys and Compounds, Vol. 618, No. 5, pp. 742-749, 2015.

(2) **Liang Li**, Shinji Hirai, Haibin Yuan, Eiji Nakamura,“Synthesis of ytterbium sulfides by the sulfurization and heat treatment”, Key Engineering Materials, Vol. 655, pp. 224-229, 2015.

(3) **Li Liang**, Shinji Hirai, Eiji Nakamura, Haibin Yuan,“Influences of Eu_2O_3 characters and sulfurization conditions on the preparation of EuS and its large magnetocaloric effect”, Journal of Alloys and Compounds, Vol. 687, pp. 413-420, 2016..

(4) **Li Liang**, Shinji Hirai, Eiji Nakamura, Haibin Yuan, “Synthesis of europium sulfides by CS_2 sulfurization and heat treatment”, MRS Advances, DOI: http://dx.doi.org/10.1557/adv.2016.346.

(5) **Li Liang**, Shinji Hirai, Yohei Tasaki, “Synthesis and sintering of samarium rich SmS_x and its electrical property”, Journal of Rare Earths, (Accepted).

International Proceedings:

(1) **Liang Li**, Shinji Hirai, et. al, “Synthesis of valence-fluctuation rare-earth monosulfides and their specific heat characteristics at very low temperatures, 2015 MRS Fall meeting, 2015.12.3; (Poster),Boston, USA.

(2) **Liang Li**, Shinji Hirai, et. al, “Synthesis of high-purity EuS prepared by CS_2 sulfurization and heat treatments, 9th international conference on f-elements, 2015.9.7(Poster), Oxford, UK.

(3) **Liang Li**, Shinji Hirai, et. al, “Synthesis and phase transformation of europium sulfides prepared by CS_2 sulfurization”, 3rd International Doctoral Student Symposium on Material Science, 2015.2.26; (Oral), Sapporo, Hokkaido, Japan.

(4) **Liang Li**, Shinji Hirai, Haibin Yuan, “Synthesis of ytterbium sulfides by the sulfurization and heat treatment”, 5th International Congress Ceramics, 2014.8.20; (Oral) Beijing, China.

Proceedings of Local Presentation:

(1) **Liang Li**, Shinji Hirai, et. al, “Synthesis and sintering of polycrystalline EuS and its magnetocaloric effect at low temperature”, Muroran-IT Rare Earth Workshop2016, 2016.6.11,Rusutsu.

(2) **Liang Li**, Shinji Hirai, et. al, “Synthesis of europium sulfides by CS_2 gas sulfurization and their phase transformation”,資源·素材(春)2015.3.29,千葉.

(3) **李良**,葛谷俊博,平井伸治, “Yb_2O_3の CS_2ガス硫化と熱処理によるイッテルビウム硫化物の合成”,資源·素材 2014.9.15, 熊本.

(4) **李良**, 葛谷俊博，平井伸治, “Yb_2O_3の CS_2ガス硫化と熱処理による YbS の合成”,日本金属学会北海道支部,2014.7.28, 札幌.

(5) 朝倉貴一,Fan Haotian,**Liang Li**,平井伸治,中村英次,太田道広,葛谷俊博, “反応焼結法によるテトラヘドライト型 $Cu_{12}Sb_4S_{13}$焼結体の作製”, 資源·素材(春)2015. 3.29,千葉.

(6) 金澤昌俊,**李良**,葛谷俊博,関根ちひろ,平井伸治,“重希土類硫化物 Ln_2S_3 の圧力－温度相図”,第 1 回物構研サイエンスフェスタ,2013.3, つくば.

(7) 金澤昌俊,**李良**,葛谷俊博,関根ちひろ,平井伸治,“重希土類硫化物 Ln_2S_3 の高温高圧合成Ⅱ”,第 54 回高圧討論会,2013.11,新潟.

(8) 金澤昌俊,**李良**,葛谷俊博,関根ちひろ,平井伸治,“重希土類硫化物 Ln_2S_3 の高温高圧合成”,第 53 回高圧討論会,2012.11, 大阪.

(9) 松本宏一,村山大樹,裏雄太郎,宇治山崇,**李良**,平井伸治,中村英次,“希土類硫化物 EuS の磁気熱量効果”, 2015 年度秋季低温工学·超電導学会, 2015.12.2-4, 神戸.